UC Santa Barbara

UC Santa Barbara Electronic Theses and Dissertations

Title

Using Imaging Spectrometry and Thermal Imagery to Study Agriculture During Severe Drought in California’s Central Valley

Permalink

https://escholarship.org/uc/item/6n41v0mq

Author

Shivers, Sarah Wells

Publication Date

2019

Peer reviewed|Thesis/dissertation

eScholarship.org Powered by the California Digital Library
University of California

UNIVERSITY OF CALIFORNIA

Santa Barbara

Using Imaging Spectrometry and Thermal Imagery to Study Agriculture During Severe Drought in California's Central Valley

A dissertation submitted in partial satisfaction of the

requirements for the degree Doctor of Philosophy

in Geography

by

Sarah Wells Shivers

Committee in charge:

Professor Dar A. Roberts, Chair

Professor Joseph P. McFadden

Professor Christina (Naomi) Tague

March 2019

The dissertation of Sarah Wells Shivers is approved.

_____
Christina Tague

_____
Joseph P. McFadden

_____
Dar A. Roberts, Committee Chair

February 2019

Using Imaging Spectrometry and Thermal Imagery to Study Agriculture During Severe Drought in California's Central Valley

Copyright © 2019

By

Sarah Wells Shivers

ACKNOWLEDGEMENTS

I owe a lot of gratitude to my advisor, Dar Roberts, who helped shape me into the remote sensing scientist that I am today. I started graduate school not even knowing what remote sensing was. Dar recognized my potential before I had the confidence to, took me into the VIPER lab, kept me funded throughout the entire PhD, and trained me into the researcher and scientist I am today. I am thankful for his mentorship and support.

I also want to thank my committee members Joe McFadden and Naomi Tague. Joe provided excellent advice, thorough feedback, and much-appreciated encouragement throughout the entire dissertation. I always gained a lot from each conversation with him. Naomi added a valuable expertise in eco-hydrology that enhanced my dissertation.

Thank you to Cohort 2013 for the bonfires, camping trips, scavenger hunts, and nights at American Ale. You all made graduate school a lot of fun.

Thank you to the Geography Department – faculty, staff, and graduate students. You've been a wonderful community to be a part of for the last 5+ years. Special thanks to Hugo Loaiciga for advising me for the first year and to Charles Jones for helping me think through the water vapor work.

Thank you to the VIPER Lab, including Seth Peterson, Erin Wetherley, Susan Meerdink, Mingquan Chen, Zach Tane, Alana Ayasse, David Miller, Fernanda Ribeiro, Gabriel Daldegan, Chris Kibler, and Rachel Green. Your feedback and support was critical to my success.

I am very grateful for the funding I received from the National Science Foundation Graduate Research Fellowship that gave me the resources to fully focus on this research. Thanks to my additional funding sources: Jack and Laura Dangermond, JPL, TAships from the Geography Department, the Army Research Lab, the UCSB Academic Senate, and RAships with Dar.

Thank you to my family, especially my parents Olin and Nancy Shivers and my sister Mackenzie Shivers, for their support, advice, encouragement, and love over the past six years.

And last, but certainly not least, thank you to my husband James and dog Atlas for the hikes and the walks on the beach, the laughs, the encouragement, the emotional and financial support, and for making our home a happy place to come back to at the end of each day. This dissertation would not have been possible without your support and love.

VITA OF SARAH WELLS SHIVERS
February 2019

EDUCATION

Bachelor of Arts in International Relations and Community Health, Tufts University, June 2010 (summa cum laude)
Doctor of Philosophy in Geography, University of California, Santa Barbara, March 2019 (expected)

PROFESSIONAL EMPLOYMENT

Graduate Research Assistant, Earth Research Institute	09/2018-03/2019
Graduate Research Assistant, NASA Jet Propulsion Laboratory	05/2018-11/2018
Graduate Research Assistant, University of California Santa Barbara	10/2016-03/2017
	04/2015-10/2015
Visiting Researcher/Intern, U.S. Army Research Laboratory (ARL West)	06/2016-09/2016
Teaching Assistant, University of California Santa Barbara	09/2013-03/2015

PUBLICATIONS

Shivers, S.W., Roberts, D.A., & McFadden, J. (2019). Using paired thermal and hyperspectral aerial imagery to explore land surface temperature variability and assess stress within California orchards. *Remote Sensing of Environment*, Volume 222, 2019, Pages 215-231.

Shivers, S.W., Roberts, D.A., McFadden, J., & Tague, C.N. (2018). Using imaging spectrometry to study changes in crop area in California's Central Valley during drought. *Remote Sensing*, *10*(10), 1556.

Borel-Donohue, C. C., **Shivers, S. W.**, & Conover, D. (2017). Spectral and spatial variability of undisturbed and disturbed grass under different view and illumination directions. In *SPIE Defense+ Security* (pp. 101980I-101980I). International Society for Optics and Photonics.

Loáiciga, H. A., Sadeghi, K. M., **Shivers, S**., & Kharaghani, S. (2015). Stormwater control measures: Optimization methods for sizing and selection. *Journal of Water Resources Planning and Management*, *141*(9), 04015006.

AWARDS

NASA Jet Propulsion Laboratory Subcontract, 2018
Doctoral Student Travel Grant, UC Santa Barbara Academic Senate, 2018
National Institute for Food and Agriculture Student Travel Award, 2018
Dangermond Travel Award, UC Santa Barbara, 2015, 2016, 2017, 2018
National Science Foundation Graduate Research Fellowship, 2015

ABSTRACT

Using Imaging Spectrometry and Thermal Imagery to Study Agriculture During Severe Drought in California's Central Valley

by

Sarah Wells Shivers

In California, predicted climate warming increases the likelihood of extreme droughts. As irrigated agriculture accounts for roughly 80% of the state's managed water supply, agriculture simultaneously shows high vulnerability to a warming climate while also offering the greatest opportunity to mitigate the impact of future droughts through adaptation strategies. This dissertation took advantage of hyperspectral Airborne Visible/Infrared Imaging Spectrometer (AVIRIS) and thermal MODIS/ASTER Airborne Simulator (MASTER) imagery collected by the HyspIRI Airborne Campaign over three years of a multi-year drought to measure agricultural response to changes in water availability and highlight the potential of remote sensing to aid in future agricultural management during water-limited times. In Chapter 2, I used the Random Forest classifier to classify crops into categories of similar water usages, assess the accuracy at which hyperspectral imaging could be of use for agricultural mapping, and evaluate changes in crop plantings with drought. The results showed overall field-level accuracies of 94.4% with AVIRIS, as opposed to 90.4% with Landsat OLI and 91.7% with Sentinel, indicating that hyperspectral imagery has the potential to identify crops by water-use group at a single time step at higher accuracies than multispectral sensors. With these classifications, I

quantified shifts in crop plantings over drought and found a prioritization of high-value, perennial crops over lower-valued annual plantings. In Chapter 3, I used paired AVIRIS and MASTER imagery to assess crop stress in fruit and nut orchards using an approach that accounted for thermal complexity within the landscape, without the need for ancillary environmental measurements. I used surface characteristics obtained by AVIRIS data to model expected pixel temperatures. These temperatures were compared to measured temperatures as a way of assessing crop stress. Crop species showed significantly different temperature distributions independent of fractional cover ($F(10, 33135) = 735$, $p < 0.001$ for 2013, with similar results in 2014 and 2015). Crop residuals were found to increase as the drought progressed with average residuals of 0.14°C in 2013, 0.97°C in 2014, and 1.1°C in 2015. In addition, crops with the highest LST residuals had the largest reductions in yield during the study period. In Chapter 4, I analyzed spatiotemporal patterns of water vapor as they varied across a diverse and dynamic agricultural scene. I tested a set of hypotheses to better understand surface-atmosphere interactions and their ability to be evaluated through AVIRIS-derived column water vapor estimates. Results showed a positive correlation between crop water use and the frequency with which that crop showed directional alignment between wind and water vapor ($r=0.42$). We also found patterns of water vapor across the region that support advection of moisture across the scene. Results conclude that accumulation of water vapor above fields in these scenes is observable with water vapor imagery while advection at the field level is obscured by variable winds, differences in field structure and composition, and smaller-scale patterns of vapor. Overall, this dissertation enhances scientific and social ability to monitor and assist in food and water resource management with remote sensing during drought.

TABLE OF CONTENTS

Chapter 1: Introduction

California's agricultural sector critically affects both the national food supply and regional water resources. California has the largest agricultural sector in the country, producing two thirds of the fruits and nuts in the United States and approximately one third of its vegetables (NASS, 2013). California's crop supply is also significant to the United States in that many crops grown in the state, such as almonds, garlic, olives, raisin grapes, pistachios, and walnuts, are exclusively produced there (CDFA, 2018). However, while California's more than 400 commodities (Starrs & Goin, 2010) are central to US food supplies, they also necessitate high water inputs. High crop production and a semi-arid climate result in agricultural needs using over eighty percent of the state's managed water supply (CA DWR, 2018). This reliance on irrigated inputs means that yearly crop prices and food supplies in the United States are susceptible to changes in the available water supply of California and impacted by local water management decisions (Cooley et al., 2015; Howitt et al., 2015). As California's water supply becomes increasingly unpredictable due to changes in climate, this interconnection of food and water supplies at local to national scales is ever more important to understand.

California's highly variable water supply is a factor of its natural climatology but is further exacerbated by larger climate trends shaped by manmade influences. California has, for centuries, experienced oscillations between wet and dry periods that result in California having the greatest variations in annual precipitation of any state in the country (CA DWR, 2017). However, over the past century, an increase in surface temperature by 0.6-0.7° C has led to changes in California that are attributable to human GHG emissions (Barnett et al., 2004) and further affect water availability: earlier spring snowmelt (Stewart et al., 2005), an

increase in percent of precipitation as rain rather than snow (Knowles et al, 2006), warmer winter and spring temperatures (Cayan et al, 2001), and less snow accumulation over the last fifty years (Mote et al, 2005). Climate change will continue to augment the patterns of precipitation in California and intensify effects on water resources and agriculture. By early in the 21st century, the Bureau of Reclamation predicts that the Central Valley will experience a 1-degree Celsius (C) rise in annual average temperature and a 2-degree C increase by mid-century that will likely be accompanied by a north-to-south trend of decreasing precipitation (U.S. Department of the Interior, 2014). This shift in temperature is projected to increase the frequency, intensity, and duration of droughts over the next century (Burke et al., 2006) that will make our current water system performance levels impossible to sustain in the Central Valley (Barnett et al. 2004).

One way to prepare for the anticipated increase in drought is to study past events as an indicator of future effects. From 2012 to 2016 California experienced its worst drought in history (Griffin & Anchukaitis, 2014). Water allotments were cut across the board and farmers, as the users of the majority of the state's water, were especially hard hit (CA Department of Water Resources, 2014). With the State Water Project and the Central Valley Project allocations cut to zero in some areas, agricultural communities in the Central Valley faced surface water reductions of an estimated 8.1 billion cubic meters (bcm) a year from 2013 to 2014, amounting to a 36% reduction in surface water availability for farms (Howitt et al., 2014). The study found that a 62% increase in groundwater extraction partially compensated for the reduction in surface water but threatened the health of California's aquifers and moreover, still left farmers with an overall deficit of 1.9 bcm/y (out of 32.1 bcm used in a normal year; Howitt et al., 2014). This extreme event and

climatological anomaly presents an opportunity to better understand how managed crops are impacted by water limitation. As lack of water will be a major limiting factor for agricultural production within the next century (Rijsberman, 2006), patterns of crop water use and their response to reduced water availability need to be carefully analyzed so impacts to long-term food and water security can be better understood as we move into a new climate regime.

Remote sensing provides new opportunities to monitor agricultural change with drought and capture spatial variations and trends in plant water use that traditional on-the-ground methods like county-level reporting, lysimeters and eddy flux towers are unable to do given their limited spatial scope and significant time and labor inputs (Gowda et al., 2008). Current crop monitoring initiatives in the United States primarily rely on imagery from earth-observing satellites such as Landsat (spatial resolution ~30m, temporal resolution ~16 days), Moderate Resolution Imaging Spectroradiometer (MODIS: spatial resolution 0.25-1 km, temporal resolution ~1-2 days) and the Advanced Spaceborne Thermal Emission and Reflection Radiometer (ASTER; spatial resolution 15-90 m, temporal resolution ~16 days) to map crops and assess health and water use information (Gowda et al., 2008). However, a new satellite, the Surface Biology and Geology (SBG) Mission, has been proposed as an improvement in both spatial and spectral performance for ecosystem study (National Academies of Sciences, Engineering, and Medicine, 2018). The SBG Mission will combine two sensors, a hyperspectral sensor in the visible through shortwave infrared at a 30 m resolution and a thermal sensor at a spatial resolution of 60 m for global coverage and a 5-19 day revisit. This mission has the potential to improve ability to assist crop and water managers in dynamic and diverse environments, such as the Central

Valley of California, with resource accounting and drought response by capturing refined spectral information at a spatial scale that is fine enough to resolve individual fields. With the impending launch of this satellite, it is important to determine its scientific capabilities for routine observation of crops in California at a level that is of use to water managers.

To test the capabilities of the SBG sensor, the Hyperspectral Infrared Imager (HyspIRI) Airborne Campaign flew the Airborne Visible/Infrared Imaging Spectrometer (AVIRIS) and MODIS/ASTER Airborne Simulator (MASTER) sensors on NASA's ER-2 plane throughout California from 2013 to 2017 to simulate expected datasets from SBG (Lee et al., 2015). AVIRIS is a 224 band imaging spectrometer that captures spectral information from 350 to 2500 nm at ~10 nm increments (Green et al., 1998). MASTER is a thermal sensor that captures 8 bands of emissivity between 4-12 μm, used to represent the proposed SBG thermal bands (Hook et al, 2001). The AVIRIS data was resampled to a resolution of 18 m while the MASTER data was resampled to a 36 m resolution. This paired dataset was flown over a portion of the Southern Central Valley seasonally while the state experienced severe drought effects. This unique dataset allows for study of remote sensing capabilities while also providing valuable information as to the response of crops in California to drought.

The goal of this dissertation is to use data from the HyspIRI Airborne Campaign to evaluate how hyperspectral and thermal imagery can be used to improve upon current initiatives to account for and manage food and water resources in the face of a changing climate. This research will study patterns of agriculture and crop water use in the Central Valley as they shift throughout the course of an intense drought period from 2013-2015. These patterns will be investigated using imaging spectrometry from AVIRIS and thermal

imaging from MASTER by mapping crops into relevant water use groups and then analyzing three indirect measures of crop water use from the imagery: choice of crop plantings, land surface temperatures, and water vapor patterns. Moreover, this dissertation will serve as a proof of concept for actively monitoring and measuring agriculture from space when the proposed SBG satellite is launched.

In Chapter 2, I use three hyperspectral images acquired from AVIRIS over the course of the 2013-2015 drought in the Central Valley of California to both evaluate the performance of hyperspectral imagery for crop classification and to study farmer decision-making with drought. A random forest classifier is run on the AVIRIS imagery to classify crops into groups of similar water use. Results are then compared to equivalent classifications using Landsat Operational Land Imager (OLI) and Sentinel-2 imagery. The AVIRIS results are analyzed for portability and band importance. The results of this classification are then used to study the prevalence of crops as they change with increasing drought. Analysis highlights the economic and environmental drivers of planting decisions, and what this means for the future of California agriculture.

In Chapter 3, I use spatially coincident AVIRIS and MASTER imagery from 2013, 2014 and 2015 to study the health of perennial crops over drought. First, I use a mixing model on AVIRIS imagery to decompose the scene into its fractional makeup of green vegetation (GV), non-photosynthetic vegetation (NPV), and soil. Next, I model the expected temperature of each pixel as the fractional linear sum of its thermal components. I then calculate a thermal residual for each pixel as the difference between its measured temperature from MASTER and the modeled temperature. This method strips away thermal variability due to air temperature, time of day, fractional cover, structure, and moisture to

allow for direct thermal comparisons between pixels and crop species. Thermal variability within agricultural fields is quantified and crop health is assessed.

In Chapter 4, I evaluate spatiotemporal patterns of water vapor as they occur over agricultural fields in the Central Valley to evaluate the potential of this imagery to assist with agricultural applications. I use pixel-level column water vapor estimates derived from AVIRIS radiance imagery, surface characteristics obtained from AVIRIS reflectance imagery, and interpolated maps of wind to investigate relationships between the atmosphere and the surface. I propose and test a set of hypotheses for how water vapor will interact with the landscape in a diverse and complex agricultural scene at the pixel, field and scene scales. Results and analysis further knowledge of opportunities and limitations for using water vapor imagery to better understand crop water use.

Chapter 2: Using imaging spectrometry to study changes in crop area in California's Central Valley during drought

With Dar A. Roberts, Joseph P. McFadden and Christina Tague

This chapter is based on a manuscript published in the journal of *Remote Sensing*:

Shivers, S.W., Roberts, D.A., McFadden, J., & Tague, C.N. (2018). Using imaging spectrometry to study changes in crop area in California's Central Valley during drought. *Remote Sensing*, *10*(10), 1556.

2.0. Abstract

In California, predicted climate warming increases the likelihood of extreme droughts. As irrigated agriculture accounts for 80% of the state's managed water supply, the response of the agricultural sector will play a large role in future drought impacts. This study examined one drought adaptation strategy, changes in planting decisions, using Airborne Visible/Infrared Imaging Spectrometer (AVIRIS) imagery from June 2013, 2014, and 2015 from the Central Valley of California. We used the random forest classifier to classify crops into categories of similar water use. Classification accuracy was assessed using the random forest out-of-bag accuracy, and an independently validated accuracy at both the pixel and field levels. These results were then compared to simulated Landsat Operational Land Imager (OLI) and simulated Sentinel-2B results. The classification was further analyzed for method portability and band importance. The resultant crop maps were used to analyze changes in crop area as one measure of agricultural adaptation in times of drought. The results showed overall field-level accuracies of 94.4% with AVIRIS, as opposed to 90.4% with Landsat OLI and 91.7% with Sentinel, indicating that hyperspectral imagery has the potential to identify crops by water-use group at a single time step at higher accuracies than multispectral sensors. Crop maps produced using the random forest classifier indicated that the total crop area decreased as the drought persisted from 2013 to 2015. Changes in area by crop type revealed that decisions regarding which crop to grow and which to fallow in times of drought were not driven by the average water requirements of crop groups, but rather showed possible linkages to crop value and/or crop permanence.

2.1. Background

Although California faces substantial variability in interannual precipitation and is accustomed to multi-year dry periods, the 2012 to 2016 drought was exceptional in its severity, and may be emblematic of greater shifts in California's climate associated with anthropogenic warming (Diffenbaugh et al., 2015; Griffin and Anchukaitis, 2014; Swain et al., 2014). Climate projections for California indicate that mean and extreme temperatures are likely to increase over the next century, which will increase the risk of experiencing future droughts of the severity of the 2012–2016 event (AghaKouchak et al., 2014; Swain et al., 2014). Future droughts will undoubtedly continue to put strain on water supplies, but the magnitude and extent to which these events impact water resources will depend not only on the characteristics of the drought, but also on the adaptive responses of people (AghaKouchak, 2015; Howden et al., 2007; Lobell et al., 2008; Palazzo et al., 2017). In California, where the agriculture sector uses roughly 80% of the state's managed water (CA DWR, 2014), agriculture simultaneously shows high vulnerability to a warming climate (Lobell et al., 2006; Schlenker et al., 2007) while also offering the greatest opportunity to mitigate the intensity of future drought impacts through adaptation strategies (Medellín-Azuara et al., 2008; Tanaka et al., 2006; Vermeulen et al., 2010). Consequently, it is critical to study how we can monitor crop management response in real-time in order to assist with policymaking during drought and analyze the ways in which the long-term sustainability of food and water security can be improved. This research used annual hyperspectral remote sensing imagery to assess the accuracy at which imaging spectroscopy can be used to map crops into categories of similar water demand and analyze changes in cropping patterns in a portion of the Central Valley. The study takes advantage of data collected over three years of

a multi-year drought as a unique opportunity to measure agricultural response and adaptation in times of drought.

Climate change is likely to significantly affect regional agricultural patterns and crop yields (Adams et al., 1990), in part due to management decisions such as fallowing fields or switching crop varieties or species (Challinor et al., 2014; Tortajada et al., 2017). Therefore, monitoring how crop patterns change during droughts is a direct measure of adaptive response. Cropping decisions impact society in multiple ways by altering regional water requirements (Allen et al., 1998), food yields (Challinor et al., 2014), economic production (CDFA, 2016), and pesticide exposure (Nuckols et al., 2007). Consequently, accurate and timely crop maps are necessary to support long-term adaptation planning for a broad range of sectors, and are of use to farmers, managers, policymakers, and scientists. Remote sensing has the potential to map crops and monitor changes in crop area more efficiently and frequently than time and labor-intensive on-the-ground crop accounting. Hyperspectral imagery, which samples hundreds of spectrally contiguous wavelengths, has the potential to identify crops at a single time point with a single sensor at higher accuracies than a broadband sensor (Galvão, et al., 2016). This ability is critical to enabling managers and scientists to stay abreast of rapidly changing planting choices and assess current risks, which is a need that current mapping initiatives with remote sensing are unable to fulfill.

Most remote sensing mapping initiatives in the United States rely on satellites such as Landsat and the Moderate Resolution Imaging Spectrometer (MODIS) because of their large spatial and temporal coverage, ease of accessibility, and free availability (Craig, 2001; Lobell and Asner, 2004; Massey et al. 2017; Ozdogan, 2010; Wardlow and Egbert, 2008; Yan and Roy, 2016; Zhong et al., 2011). The National Agricultural Statistics Service (NASS)'s

Cropland Data Layer (CDL) is the most comprehensive current agricultural mapping initiative for the United States with an easily accessible crop map published at yearly intervals at a 30-m resolution (USDA, 2016). It relies on data from Deimos-1, the United Kingdom's Disaster Monitoring Constellation 2 (UK-DMC 2), and Landsat 8 Operational Land Imager (OLI) and produced an overall accuracy of 81.1% in California in 2016, with accuracies of crop groups ranging from a low of 32.8% for berries to 77.6% for forage crops. Although widely used and highly useful, the CDL has limitations concerning reproducibility and timeliness. First, by using three sensors, not all of which produce publicly available data, reproducing this map or using this methodology on a different study area or at a different time would not be possible. Furthermore, with maps published at the end of each year, the CDL does not offer near real-time or mid-growing season assessments of crop area.

Another method of crop mapping uses multi-temporal MODIS imagery to classify crops using annual crop phenology for identification (Chang et al., 2007; Lobell and Asner, 2004; Wardlow and Egbert, 2008; Zhong et al., 2011). These studies illustrate the ability of time series datasets to produce detailed and accurate crop classification maps at the end of an agricultural year in a single study area, but this methodology also faces challenges that hinder its practical and scientific usefulness in California. First, the spatial resolution of MODIS is not fine enough to individually classify many fields. For example, the average size of a field in the area of this study is approximately 0.2 km^2. Therefore, even at its finest resolution of 250 m, most MODIS pixels will result in mixtures of different fields or crop types, and are therefore best suited for croplands at larger scales (Lobell and Asner, 2004). Second, multi-temporal crop mapping is limited in its spatial scope due to a spatial variation in phenology that would decrease the accuracy if it was applied over a large spatial area (Zhang et al.,

2003). Third, the co-registration of multiples images and the need for cloud-free images create challenges for time-series analysis that single-data hyperspectral analyses do not face (Key et al., 2001). Finally, the need for multiple images throughout time obviates the ability to conduct real-time crop assessments.

Hyperspectral imagery can act as a complement to these current crop-mapping initiatives, as it has the potential to identify crops at a single time point with greater accuracy than broadband sensors, and therefore can provide mid-season assessments of crop area without a yearly time-series (Galvão et al., 2016; Mariotto et al., 2013; Thenkabail et al, 2002;2004; 2013). Discriminating crop types is challenging due to differing biophysical traits, development stages, variable management practices, regional weather and topography, and the timing of plantings (Galvão et al., 2016). Despite these complications, various studies have successfully shown the ability to use hyperspectral imagery to classify crops and cultivars (Bandos et al., 2009; Camps-Valls et al., 2003; Galvão et al., 2005; Galvão et al., 2009; Mariotto et al., 2013; Rao, 2008; Thenkabail et al 2013). By discriminating crop types with a single image from one time point, hyperspectral imagery can serve as a time-critical agricultural management tool, providing scientists, farm managers, and policymakers with improved information regarding the agricultural landscape and on-the-ground food and water needs. This study uses airborne hyperspectral imagery over a portion of the Central Valley to assess the accuracy of imaging spectroscopy for agricultural classifications and conducts a case study to display the utility of these classifications for analyzing changes in farming decisions. The results of this study, while limited in their spatial scope due to the use of airborne imagery, are salient in light of recently available Sentinel-2 data and the proposed HyspIRI mission, which would provide repeat, global hyperspectral imagery.

This paper explores the use of hyperspectral imagery for agricultural management in drought scenarios with the following two goals: (1) to study the accuracy to which we can map crops in California's Central Valley into groups of similar water use using hyperspectral imagery, and (2) to analyze the produced classification maps from 2013, 2014, and 2015 in the context of the drought by examining the crop area changes in relationship to average crop water use, average crop value, and crop annual/perennial status. We expected to find consistency with previous analyses of the drought that found that higher-value, perennial crops were prioritized over lower-value annual crops over the course of the drought (Tortajada et al., 2017).

2.2. Methods

2.2.1. Study Area

This research focused on a 3470 km^2 transect of the Central Valley of California that reaches from Kern County to Fresno County, and was flown as part of a large trans-state flight path that is referred to as the "Soda Straw" in NASA's Hyperspectral Infrared Imager (HyspIRI) Airborne Campaign plan (Figure 2.1). The study area includes portions of three of the top four leading agricultural counties in California, Fresno, Tulare, and Kern, as well as portions of Kings County (CDFA, 2016). This area includes thousands of crop fields of varying sizes, crop types, land managers, and irrigation practices (Johnson & Cody, 2015). The greater study area in which the agricultural fields reside is the Tulare Lake Hydrologic Region, which comprises the southern third of the Central Valley, and is the largest agricultural region in California with about 1.2 million irrigated hectares within the 4.4 million hectares that it covers (CA DWR, 2009). The region is prosperous for agriculture partially because of its long growing season, with moist winters often blanketed with fog and

dry summers (CA DWR, 2009). While prosperous for agriculture, Tulare Lake is the driest region of the Central Valley, receiving an average of less than 25.4 cm of precipitation a year (CA DWR, 2009; Carle, 2004).

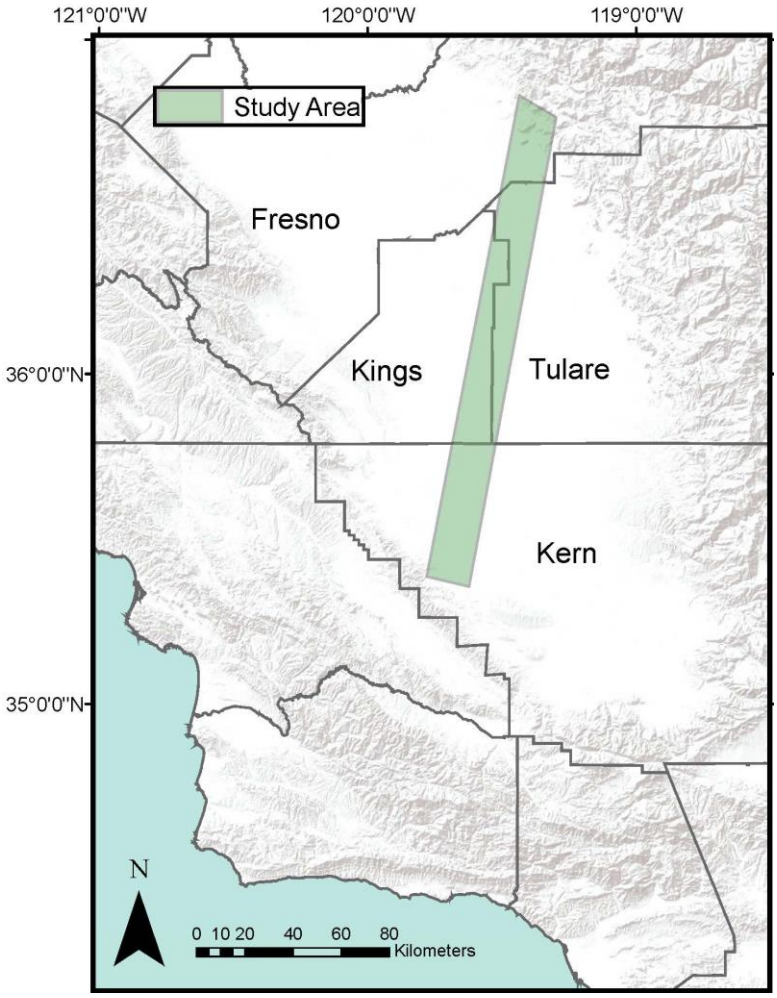

Figure 2.1. Study area with county boundaries.

2.2.2. Datasets

2.2.2.1. Imagery

This research focused on three images of the Central Valley of California collected by the Airborne Visible/Infrared Imaging Spectrometer (AVIRIS) during the course of the 2012–2016 drought. AVIRIS is a 224-band imaging spectrometer that captures wavelengths

between 350–2500 nm at 10-nm increments (Green et al., 1998). The imagery was acquired from NASA's Jet Propulsion Lab (JPL), which pre-processed the imagery and produced a data product of orthorectified, atmospherically corrected reflectance at a spatial resolution of 18 m (Thompson et al., 2015). Data was acquired from the JPL ftp (https://aviris.jpl.nasa.gov/data/AV_HyspIRI_Prep_Data.html). Further processing of the reflectance data included a rotation and secondary orthorectification using 1-m digital orthophoto quarter quads (DOQQ) from the National Agriculture Imagery Program (NAIP) that were resampled to 18 m. We used Delaunay triangulation to georectify the AVIRIS imagery to the NAIP imagery, using approximately 250 ground control points per flight line. Due to atmospheric absorption and the noise of the reflectance product, AVIRIS bands 1–5, 61–63, 81, 106–120, 152–174, and 220–224 were not used, leaving a total of 172 bands for further analysis. This imagery was collected as part of the HyspIRI Airborne Campaign, a NASA mission that captured airborne imagery from various areas of California between 2013–2017 to investigate the capabilities of combined hyperspectral and thermal sensing for a proposed satellite mission with global coverage (Lee et al., 2015). We used imagery from three flights that were flown on 6 June 2013, 3 June 2014, and 2 June 2015, capturing the peak summer growing season for many Central Valley crops.

The imagery was captured during severe drought conditions in California with high temperatures and persistent below-average rainfall, which led to a state of drought emergency declared in January 2014 and lifted in April 2017 (USGS, 2018). The three-year event from 2012 to 2014 is estimated to be the most severe drought in 1200 years, while the cumulative effect of the drought from 2012 to 2015 is unprecedented in its severity (Griffin & Anchukaitis, 2014; Robeson, 2015). As another metric of the severity of the drought, the

United States (US) Drought Monitor reported that for the week closest to the image acquisition in 2013, over 53% of the state was facing severe, extreme, or exceptional drought. By June 2014, that percentage was up to 100%, and by June 2015, over 93% of the state still remained in these most severe drought categories (US Drought Monitor, 2018).

2.2.2.2. Crop Polygons

To train and validate the crop classification, we relied upon digitized polygons of crop fields provided by Kern, Kings, Fresno, and Tulare counties. The Kern County data layer was acquired through the Kern County Spatial Data website (http://www.kernag.com/gis/gis-data.asp). The Kings, Tulare, and Fresno shapefiles were acquired from each of the respective counties at the request of the researcher. These crop layers are compiled each year as part of a statewide pesticide permitting and use reporting program, which requires farmers in California to obtain permits for any pesticide use. The program resulted in county shapefiles, which detailed the distribution of crops and their pesticide use, being distributed to the public at the discretion of each county. Training and validation data were filtered to only include crops that were registered as being planted prior to and harvested after the flight date. Fields registered as containing interplantings and multicrops accounted for roughly 5% of crop polygons, and were excluded. It needs to be noted that these geographic information system (GIS) data layers obtained from the counties were not guaranteed to be comprehensive. In fact, this study operates on the assumption that the validation layers provide information on only a portion of the total study area, and are not exhaustive. Therefore, the increase or decrease in the number of validation polygons for each year cannot be taken to be indicative of the actual change in crops, but rather indicative of the completeness of the validation data.

2.2.3. Spectral Mixture Analysis

In order to separate soil or fallow pixels from those of agricultural plant matter, a spectral mixture analysis was run on each of the three images to obtain fractional green vegetation cover. Multiple Endmember Spectra Mixture Analysis (MESMA, Roberts et. al 1998) uses a linear mixture model to unmix pixels into fraction images while allowing the number and types of endmembers to vary on a per-pixel basis, thus better accounting for endmember variability. Pixels were modeled as a mixture of green vegetation (GV), soil, non-photosynthetic vegetation (NPV), and shade. Image endmembers were chosen from each of the three images from 2013, 2014, and 2015 by selecting pixels with high overall reflectance from each of the three endmember categories that were well-distributed spatially throughout the image in order to capture the variability from north to south along the flight line. A combined library of all of the chosen endmembers, consisting of eight NPV, 10 Soil, and 21 GV endmembers, was used for analysis in order to obtain consistent results throughout the years. MESMA was partially constrained by requiring shade fractions to vary between 0–0.8, and setting a maximum allowable root mean squared error (RMSE) of 0.025. The spectral mixture result was then shade normalized by dividing each non-shade component, GV, NPV, and soil by the sum total of all of the non-shade components in that pixel to obtain physically realistic fraction estimates (Adams et al., 1993). Only those pixels that contained 50% or more shade-normalized GV were chosen for training and validation, as this was decided as the threshold for classifying a pixel as a crop.

2.2.4. Classification

2.2.4.1. Class Selection

Due to the high diversity of crop species in the Central Valley, we focused on a smaller set of crop classes that would be of the most practical use to stakeholders such as water managers, farmers, and scientists. Crops were classified into categories defined and used by the California Department of Water Resources (DWR) to estimate water use (Table 2.1; CA DWR, 2017). The crops within each category have similar rates of development, rooting depths, and soil characteristics, and are therefore presumed to have similar water requirements. Categories were included in the classification if they were prominent in the area, defined as ≥20 fields of that category, each of which contained ≥50% green vegetation, in the validation layers (Table 2.2). The nine crop categories that had a sufficient number of fields to be included in this study were alfalfa, almonds and pistachios, corn, cotton, other deciduous crops, other truck crops, subtropical, tomatoes, and vines. Other crops that are grown in the area but are not being studied included cucurbits, grains, pasture, safflower, and sugar beet. Since these "other" crops are not similar in structure or phenology, we did not attempt to group them into a combined category for classification. In other agricultural regions where less frequent crops show a higher degree of similarity, adding an "other crops" group to the classification could be an appropriate way to decrease error. However, the number of fields and total area for each crop show that all of the "other" crops accounted for less than 1% of the total validated area in each of the three years, leading us to the assumption that the error due to the omission of these crops in our classification and crop area calculations will be low.

Table 2.1. Crop groupings from California Department of Water Resources (DWR).

Crop Class	Definition	Included in Study
Grain	Wheat, barley, oats, miscellaneous grain and hay, and mixed grain and hay	No
Rice	Rice and wild rice	No
Cotton	Cotton	Yes
Sugar Beet	Sugar beets	No
Corn	Corn (field and sweet)	Yes
Dry Bean	Beans (dry)	No
Safflower	Safflower	No
Other Field	Flax, hops, grain sorghum, sudan, castor beans, miscellaneous fields, sunflowers, hybrid sorghum/sudan, millet, and sugar cane	No
Alfalfa	Alfalfa and alfalfa mixtures	Yes
Pasture	Clover, mixed pasture, native pastures, induced high water table native pasture, miscellaneous grasses, turf farms, bermuda grass, rye grass, and klein grass	No
Processing Tomato	Tomatoes for processing	Yes, combined with fresh
Fresh Tomato	Tomatoes for market	Yes, combined with processing
Cucurbit	Melons, squash, and cucumbers	No
Onion Garlic	Onions and garlic	No
Potato	Potatoes	No
Other Truck Crops	Artichokes, asparagus, beans (green), carrots, celery, lettuce, peas, spinach, flowers nursery and tree farms, bush berries, strawberries, peppers, broccoli, cabbage, cauliflower, and brussels sprouts	Yes
Almond Pistachio	Almonds and pistachios	Yes
Other Deciduous Crops	Apples, apricots, cherries, peaches, nectarines, pears, plums, prunes, figs, walnuts, and miscellaneous deciduous	Yes
Subtropical	Grapefruit, lemons, oranges, dates, avocados, olives, kiwis, jojoba, eucalyptus, and miscellaneous subtropical fruit	Yes
Vine	Table grapes, wine grapes, and raisin grapes	Yes

Table 2.2. Number of validation fields and total area for fields containing ≥50% green vegetation.

Crops	Number of Fields	Total Area (km^2)
Studied Crops		
Alfalfa	340	954.4
Almond/Pistachio	442	3305.3
Corn	97	236.8
Cotton	22	64.6
Other Deciduous Crops	2174	1517.8
Other Truck Crops	22	76.5
Subtropical	634	769.5
Tomato	29	87.6
Vine	350	478.1
Other Crops		
Cucurbit	3	1.1
Grain	1	5.2
Pasture	8	13.7
Safflower	3	21.8
Sugar Beet	4	8.0
Uncultivated	17	15.0

2.2.4.2. Random Forest

The random forest classifier (Breiman, 2001) is an ensemble classification and regression technique that creates a forest of classification trees by randomly selecting subsets of the training data with replacement for each tree, randomly selecting a variable to split at each node, and then creating a multitude of decision trees that vote for the most popular class. Random forest was chosen for this study due to its computational efficiency and proven high performance (Gislason et al., 2006; Pal 2005). Five hundred trees were computed using 150,000 cases of nine crop classes with 172 spectral variables.

We randomly selected fields from each year to be used for either training or validation in order to minimize inflated accuracies due to spatial autocorrelation. Seventy percent of fields were assigned as training data, while the other 30% were set aside for independent validation. From the training fields, 50,000 pixels from each year were randomly chosen from

the pixels that contained ≥50% green vegetation, and then combined, creating a training set of 150,000 pixels across the three dates. As suggested by Millard and Richardson (2015), pixels were randomly sampled to create a training dataset that was representative of the true class proportions within the study area. A random forest was generated from these 150,000 pixels, to be used to classify each of the three images.

A 50% GV threshold was used as the cutoff for selecting pixels for training and validation in the random forest in order to maximize accuracy while also maintaining validation data for the most infrequent categories, particularly the tomato, cotton, and other truck crop classes that had the fewest training fields. To determine the threshold, 10 trial random forests were run to estimate the classification accuracy for each crop class using threshold levels ranging from 10% GV to 100% GV at 10% increments. Each run used 10,000 randomly selected pixels and populated 500 trees. We found that while the majority of the crop classes increased in accuracy as the threshold increased, the tomato class began declining in accuracy after the 50% threshold due to a significantly reduced training sample size, and there were no training or validation data available in our study area when the GV threshold was ≥80% (Figure 2.2). Therefore, in order to include tomatoes in our classification, we chose a 50% GV threshold. Additionally, mixed pixels may not be spectrally similar to the pure pixels of the classes that they contain, so using only pure pixels to train a classifier can increase the error in areas with a high proportion of mixed pixels (Foody & Cox, 1994). To this point, we aimed to choose a threshold that could capture diversity within each crop category, and felt that a high GV threshold would be restrictive in that it may exclude younger crops or certain species of crops within each class (e.g., widely spaced trees in orchards). Therefore, 50% was chosen as a compromise between attaining

high accuracy within all of the classes while also fairly representing the diversity within each crop class. Training a classifier on mixed pixels for agricultural applications has been shown to have similar accuracy as training on pure pixels (Foody & Mather, 2006).

For each year, a pixel-level classification was generated using the multi-year random forest. From this image classification, independent validation was conducted using the 30% of fields that were not used for training. From the validation fields 10,000 pixels containing at least 50% or more green vegetation were randomly chosen from each image for a total of 30,000 validation pixels over the three dates.

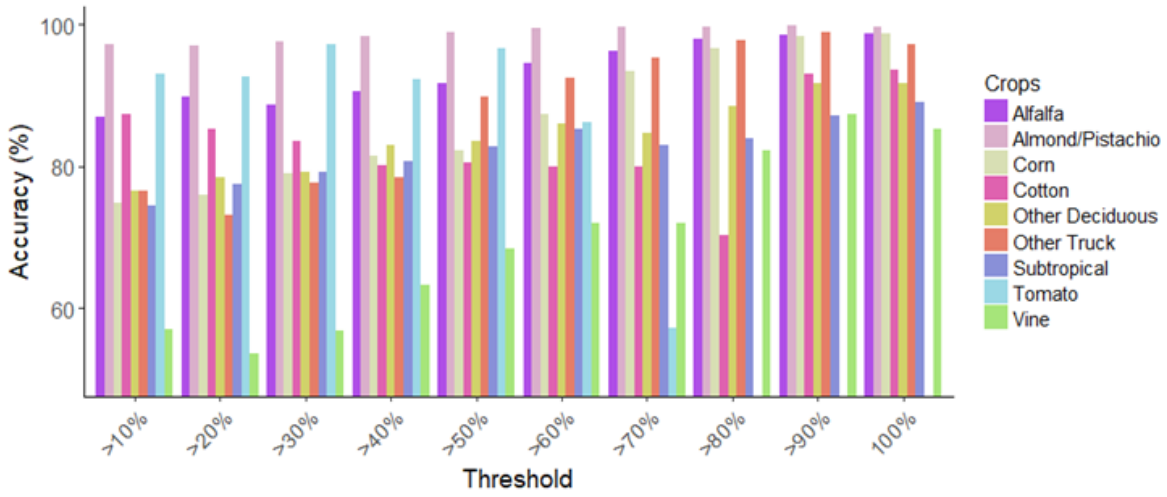

Figure 2.2. Out-of-bag (OOB) accuracy for each of the nine crop categories at different pixel green vegetation (GV) fraction threshold levels.

2.2.4.3. Field-Level Reclassification

Since multicroppings or interplantings were excluded from the training and validation, each field was assumed to be growing only one crop type. Therefore, to improve the results of the classifier for analysis of changes in crop area, a majority filter was applied to the random forest classification result to reclassify each pixel of a field as the crop category to which the plurality of pixels in that field were classified. For example, if 10% of the pixels

in a field were classified as tomato, 30% as alfalfa, and 60% as corn, all of the pixels in that field were reclassified as corn. Fields and their boundaries were defined from the crop polygon validation database. Only fields that contained a certain threshold of green vegetation were included in the field level reclassification in order to remove fallow fields from analysis. Two different field-level GV thresholds, 25% and 50%, were chosen to assess the impact of a field-level threshold on accuracy results. Final crop planting assessments were conducted using the 50% field-level threshold for an increased accuracy of analysis.

2.2.5. Accuracy Assessments

Three different classification accuracies were computed and will be discussed. The first is the pixel-level out-of-bag (OOB) error calculated by the random forest. The OOB error is an estimate of error that uses subsampling and bootstrapping to estimate the error of a sample, using only trees of the random forest that do not include the data point being validated (Breiman, 2001). The second reported accuracy is pixel-level independent validation using classified pixels that were not included in training the random forest and were not in the same field as any pixel in the random forest training set. The third accuracy is a field-level accuracy using the majority reclassification of pixels in each field.

2.2.5.1. Multispectral Imager Comparisons

To assess the benefit of a 224-band spectrometer such as AVIRIS over more commonly available multispectral sensors, a random forest classifier was run with simulated Landsat Operational Land Imager (OLI) and simulated Sentinel-2B data for accuracy comparison. AVIRIS images from all three of the dates were spectrally convolved to Landsat OLI bands 1–7 and 9 and to all of the bands of Sentinel-2B. The spatial resolution was kept constant at 18 m. These simulated images were then run in random forest using 500 trees, the same nine crop categories, and the same 150,000 training points that were used for the AVIRIS classification. OOB accuracy at the pixel level and field level were both computed for analysis.

2.2.5.2. Portability Analysis

To evaluate the portability of this method to images that are not included in the classification, three trial random forests were run where each random forest was trained with two of the study images, and then tested on the third image. For each of these random forest runs, 50,000 pixels from each of the two training dates were used to train the random forest, which populated 500 trees. Field-level accuracy is assessed for each of the three resultant classifications.

2.2.6. Case Study on Farmer Decision-Making

Using random forest and the majority-filtered reclassification with a 50% GV threshold, predictive crop maps were generated for each year. After random forest was run on each AVIRIS image, a multi-year field polygon layer was used to identify individual fields for majority reclassification. Therefore, classified fields were not constrained to those fields that were included in the validation layer from a specific year, but could include any field in the

study area that contained 50% or more green vegetation, whether it was registered as part of the validation layer or not. From these maps, crop area was assessed to analyze changes in cropping patterns within the study area over the course of the drought. We then used these maps to evaluate the hypothesis that higher-value, perennial crops were prioritized during the drought by analyzing factors including water use, economic value, and crop lifespan against the change in the planted area.

2.3. Results

2.3.1. Classification Accuracy

Comparative error between the three accuracy assessments were broken down by class and year (Table 2.3), and then each accuracy assessment was individually analyzed and broken down by crop class in tables 4–6.

Table 2.3. Accuracies by crop class and year. Independent pixel and field-level validations report accuracy as the average of the producer's accuracy (sensitivity) and user's accuracy (positive predictive value).

Crops	Out-of-Bag Accuracy	Independent Validation Pixel-Level Accuracy by Year (%)			Field-Level Accuracy after Majority Filter with 50% GV Threshold (%)		
	All Years	2013	2014	2015	2013	2014	2015
Alfalfa	93.7	94.5	87.6	93.0	94.2	94.7	97.1
Almond and Pistachio	98.8	96.1	96.2	94.2	88.9	91.7	95.6
Corn	90.9	93.1	77.0	95.1	98.3	93.8	94.1
Cotton	86.2	73.5	45.7	21.5	73.3	83.3	85.7
Other Deciduous	90.2	86.1	82.6	85.0	95.6	95.3	96.6
Other Truck	88.0	76.4	78.6	NA	100.0	100.0	68.8
Subtropical	88.0	83.9	81.8	80.6	92.3	93.2	92.9
Tomato	97.2	NA	92.3	89.2	100.0	100.0	97.1
Vine	84.5	77.2	70.2	83.5	88.3	90.6	93.4

Table 2.4. Error matrix for pixels (150,000 total) assessed using random forest OOB accuracies. Abbreviations are used for crop groups: Alfalfa (AF), Almond/Pistachio (AP), Corn (CR), Cotton (CT), Other Deciduous Crops (OD), Other Truck Crops (OT), Subtropical (ST), Tomato (TO), and Vine (VI). Crop group accuracies assessed by user's (positive predictive value) and producer's (sensitivity) accuracies. Overall OOB accuracy reported.

		Reference Data									
		AF	**AP**	**CR**	**CT**	**OD**	**OT**	**ST**	**TO**	**VI**	**Total**
Classified	AF	17,733	295	8	13	521	4	71	16	256	18,917
	AP	34	64,449	1	7	497	3	178	8	42	65,219
	CR	50	126	3645	17	160	1	3	2	4	4008
	CT	40	88	3	1347	62	0	5	3	14	1562
	OD	194	1514	7	11	26,821	0	837	12	283	29,679
	OT	36	23	0	7	111	1877	12	2	66	2134
	ST	36	694	1	7	1205	8	15,067	5	96	17,119
	TO	18	14	1	0	3	0	4	1660	8	1708
	VI	240	212	1	12	858	10	150	8	8109	9600
	Total	18,381	67,415	3667	1421	30,238	1903	16,327	1716	8878	
	User's Acc.	93.7%	98.8%	90.9%	86.2%	90.4%	88.0%	88.0%	97.2%	84.5%	
	Producer's Acc.	96.5%	95.6%	99.4%	94.8%	88.7%	98.6%	92.3%	96.7%	91.3%	
	OOB Acc.	93.8%									

Table 2.5. Error matrix for independently validated pixels (30,000) by crop type for all of the years combined. Accuracy assessment includes the user's (positive predictive value) and producer's (sensitivity) accuracies for each crop and the total overall kappa and accuracy. Abbreviations are used for crop groups: Alfalfa (AF), Almond/Pistachio (AP), Corn (CR), Cotton (CT), Other Deciduous Crops (OD), Other Truck Crops (OT), Subtropical (ST), Tomato (TO), and Vine (VI).

		Reference Data									
		AF	**AP**	**CR**	**CT**	**OD**	**OT**	**ST**	**TO**	**VI**	**Total**
Classified	AF	3891	12	22	8	52	3	2	43	85	4118
	AP	66	12,395	46	94	313	1	189	5	75	13,184
	CR	42	1	971	2	13	0	0	0	0	1029
	CT	15	3	13	161	5	3	0	0	2	202
	OD	226	256	75	48	5479	21	305	3	283	6696
	OT	0	0	1	0	4	55	0	0	1	61
	ST	45	70	2	5	289	4	2404	1	145	2965
	TO	9	1	2	0	3	0	1	292	0	308
	VI	52	13	2	5	87	10	20	4	1244	1437
	Total	4346	12,751	1134	323	6245	97	2921	348	1835	
	User's Acc.	94.5%	94.0%	94.4%	79.7%	81.8%	90.2%	81.1%	94.8%	86.6%	
	Producer's Acc.	89.5%	97.2%	85.6%	49.8%	87.7%	56.7%	82.3%	83.9%	67.8%	
	Kappa	0.86									
	Overall Acc.	89.6%									

Table 2.6. Error matrix for reference fields (4110 total) from the majority filter reclassification for all of the years combined. This error matrix only includes fields with 50% of more green vegetation. Accuracy assessment includes the user's (positive predictive value) and producer's (sensitivity) accuracies for each crop and the total overall kappa and accuracy. Abbreviations are used for crop groups: Alfalfa (AF), Almond/Pistachio (AP), Corn (CR), Cotton (CT), Other Deciduous Crops (OD), Other Truck Crops (OT), Subtropical (ST), Tomato (TO), and Vine (VI).

		Reference Data									
		AF	**AP**	**CR**	**CT**	**OD**	**OT**	**ST**	**TO**	**VI**	**Total**
Classified	AF	324	0	1	3	4	0	1	1	4	388
	AP	1	432	2	2	44	0	12	0	5	498
	CR	2	0	92	1	1	0	0	0	0	96
	CT	1	0	0	15	1	0	0	0	0	17
	OD	9	6	2	1	2095	4	42	0	38	2197
	OT	0	0	0	0	0	17	0	0	0	17
	ST	2	4	0	0	24	0	578	0	6	614
	TO	0	0	0	0	0	0	0	28	0	28
	VI	1	0	0	0	5	1	1	0	297	305
	Total	340	442	97	22	2174	22	634	29	350	
	User's Acc.	95.9%	86.7%	95.8%	88.2%	95.4%	100%	94.1%	100%	97.4%	
	Producer's Acc.	95.3%	97.7%	94.8%	68.2%	96.4%	77.3%	91.2%	96.6%	84.9%	
	Kappa	0.91									
	Overall Acc.	94.4%									

2.3.1.1. Out-of-Bag Accuracy

The random forest classifier showed high overall accuracy of 93.8% when accounting for all of the years and all of the crops. Table 2.4 details the errors by crop class through an error matrix that sums to 150,000 points, which is the number of pixels that was used to train and build the random forest. With over two million possible training pixels, the pixels used in the random forest account for 7.4% of the total. All of the crops had user and producer accuracies over 84%, and alfalfa, almond and pistachio, corn, and tomatoes resulted in accuracies of over 90%. Since training pixels were selected randomly throughout the image, the number of pixels per class was representative of the proportional crop area in the study site. Therefore, the number of pixels was highly variable by class, with almond and pistachio

pixels amounting to more than 64,000, while less prevalent crops such as tomato, cotton, and other truck crops had fewer than 2000 pixels each.

2.3.1.2. Independent Validation

Independent validation produced an overall accuracy of 89.6% when accounting for all of the years and all of the crops, which was lower than the OOB accuracy by around 4%. This decline in accuracy when validating independently is likely because the independent validation accounted for the potential of spatial autocorrelation, which is likely to inflate OOB results. The OOB assessment used the same data for training the classifier as for validation, whereas the independent validation relied on 30,000 pixels randomly selected from polygons separate from those used in training. These 30,000 pixels made up only 1.6% of the 1.87 million potential validation pixels; those with GV greater than 50% that were not used in the random forest. The tree categories, almond/pistachio, other deciduous, and subtropical had the highest consistency between years with overall accuracies changed by less than 4% between the years (Table 2.3). Cotton and truck crops were less consistent in accuracy from year to year than the other crop categories, and this inconsistency may be due, in part, to these two classes having two of the three fewest numbers of pixels used in the random forest. Accuracy for other truck crops in 2015 was not applicable (NA), because the user's accuracy was NA for that year (zero correctly classified truck crop pixels/zero total classified truck crop pixels). Accuracy was NA for tomato fields in 2013 because no tomato pixels were identified in the validation layer for that year. Despite this omission, tomatoes were included in the study, as they are a major crop group in the area with a sufficient number of training and validation polygons from 2014 to 2015.

Table 2.5 details the errors associated with each crop type. The classification of alfalfa resulted in high accuracies of near or over 90%. Almond and pistachio trees showed consistently high user and producer accuracies of 94.0% and 97.2%, respectively. The random forest was more likely to erroneously classify other crop classes as almond and pistachio than it was to misclassify almond and pistachio trees. This result was likely because the pixels of almond and pistachio trees were very prevalent in the study area, leading to a large amount of randomly sampled pixels for training, and leading the classifier to favor this class over less frequently occurring classes. Other deciduous crops and subtropical crops were most likely to be misclassified by or as each other or as almond and pistachio, illustrating that tree crops were likely to be misclassified as another tree crop. Importantly, the three tree crop categories showed a tendency toward being overmapped, while the other six classes of non-tree species were all undermapped by the classifier. Of those, cotton and other truck were the most likely to be undermapped, with producer's accuracies of 49.8% and 56.7%, respectively. The results showed that the classes that were more prevalent and had more validation data were more likely to have higher accuracy than the infrequent classes.

2.3.1.3. Field-Level Validation after Majority Filter

The final majority-filtered reclassification of pixels to create fields that contained only one crop type had the highest accuracy at 94.4%. The overall accuracy is computed as the percentage of total fields that were correctly classified using random forest and a majority filter. The higher field-level accuracy obtained by the reclassification confirmed assumptions that using a majority filter would smooth out the stray pixels that may lie between rows of crops or that capture weeds or other plant matter growing near the crop, which may lead to classification confusion. When assessing the majority-filtered reclassification results by year

(Table 2.3), seven of the nine classes had accuracies over 80% in all three years, with other truck crops and cotton being the exceptions. An important finding is that the field-level classification improved the pixel-level classification the majority of the time when a 50% GV threshold was used at the field level. When assessing pixel and field-level accuracies over all three years (tables 5 and 6), the only accuracy that decreased from the pixel to the field level was the user's accuracy of almond and pistachio orchards. As the most common crop category, assessing the accuracy at the field level increased the overmapping of this class. However, all of the other user and producer's accuracies increased. When looking at the accuracies separated by year and by class (Table 2.3), 22 of the 27 classes improved in accuracy from the pixel to the field level.

The field-level accuracies in tables 3 and 6 were computed using a 50% GV threshold, meaning that only fields that had at least 50% green vegetation or more were included in the accuracy assessment. The GV threshold represents a trade-off between accuracy and inclusivity. A higher GV threshold will decrease the risk of including fallow fields in the classification, but it will also increase the risk of excluding fields of crops that should be included. Table S1 details accuracy by class with a 25% threshold for comparison. Using a 50% GV threshold increases both user and producer's accuracies for all of the crops over the 25% GV threshold, while excluding almost 1700 fields with an average green vegetation fraction between 25–50%. When the higher threshold is used, infrequent crop categories such as cotton and other truck crops increase substantially in producer's accuracy, and prevalent crop categories, such as almond/pistachio and other deciduous crops, increase substantially in user's accuracy. The random forest is most likely to classify ambiguous pixels as one of

the most common classes, and therefore overclassifies common classes and underclassifies rarer classes when a lower field threshold is used.

With a 50% GV threshold, alfalfa, corn, other deciduous, subtropical, and tomato crops all showed user and producer accuracies over 90%. Of all of the crop categories, cotton had the lowest user and producer accuracies. The low accuracy of cotton may be attributable to a few different reasons. First, the sample size was small (22 fields with greater than 50% GV), so training data was limited. Second, early June was likely not the best time of year for the classification of cotton, because cotton is planted in March and April, but does not reach maturity for 180–200 days (CCGGA, 2017). Later in the summer may be a better time of year for quantifying total cotton extent. However, while the user and producer accuracies of cotton were low, only 22 fields of 4110 total fields in our dataset were planted in cotton. Therefore, the overall classification accuracy is not impacted much by this error.

2.3.1.4. Band Importance

To better understand the success of the random forest classifier, the mean decrease accuracy (MDA) was calculated for each wavelength (Figure 2.3). MDA can be interpreted as the number of pixels that would be misclassified if a given wavelength was removed from the random forest classifier. The 400–750 nm range, encompassing visible and red-edge portions of the spectrum, showed overall higher MDA scores than the near infrared (NIR) or shortwave infrared (SWIR) regions. The red-edge region in particular had the highest MDA score, followed by the blue region in the 400-nm range. Additionally, wavelengths on the edge of bands that were removed due to the high influence of water vapor showed higher importance than bands that did not border a water vapor region. For example, the NIR band at 957 nm showed a higher MDA score than any other band in the NIR. Some possible

explanations for these results will be explored further in the discussion. Although 704 nm had the highest MDA, only about 80 pixels would be misclassified out of 150,000 if it were removed. The small error is likely due to the high correlation between bands.

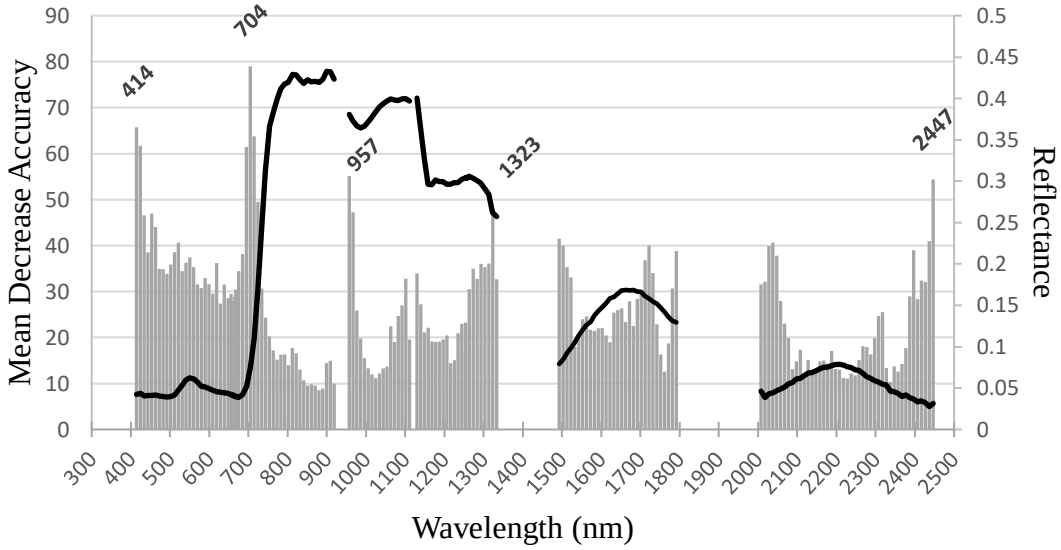

Figure 2.3. Mean decrease accuracy (MDA) is plotted for each wavelength on the primary *y*-axis, while a green vegetation spectrum is overlaid on the secondary *y*-axis in order to highlight which bands and band regions were most important for the random forest classification. A higher mean decrease accuracy score denote bands of higher significance.

2.3.1.5. Landsat and Sentinel Comparisons

We used pixel-level and field-level classification accuracies to compare the results of the random forest classifier on AVIRIS, Landsat-simulated, and Sentinel-simulated data (Figure 2.4). The Landsat and Sentinel-2 simulated datasets had the same spatial resolution and signal-to-noise ratio (SNR) as the AVIRIS data. The only difference between the three datasets was their spectral resolutions. The results showed that AVIRIS performed better than or on par with either of the simulated sensors at both the pixel and field levels. Overall field-level accuracies were 90.4% with Landsat and 91.7% with Sentinel, as opposed to 94.4%

with AVIRIS. Overall accuracies for both Landsat and Sentinel for all of the crop classes remained high with over 70% accuracy at the field level. The accuracies of the three sensors were within 10% of each other at the field level for every crop. Sentinel was less accurate than AVIRIS for most of the crop categories, but it was more accurate than Landsat.

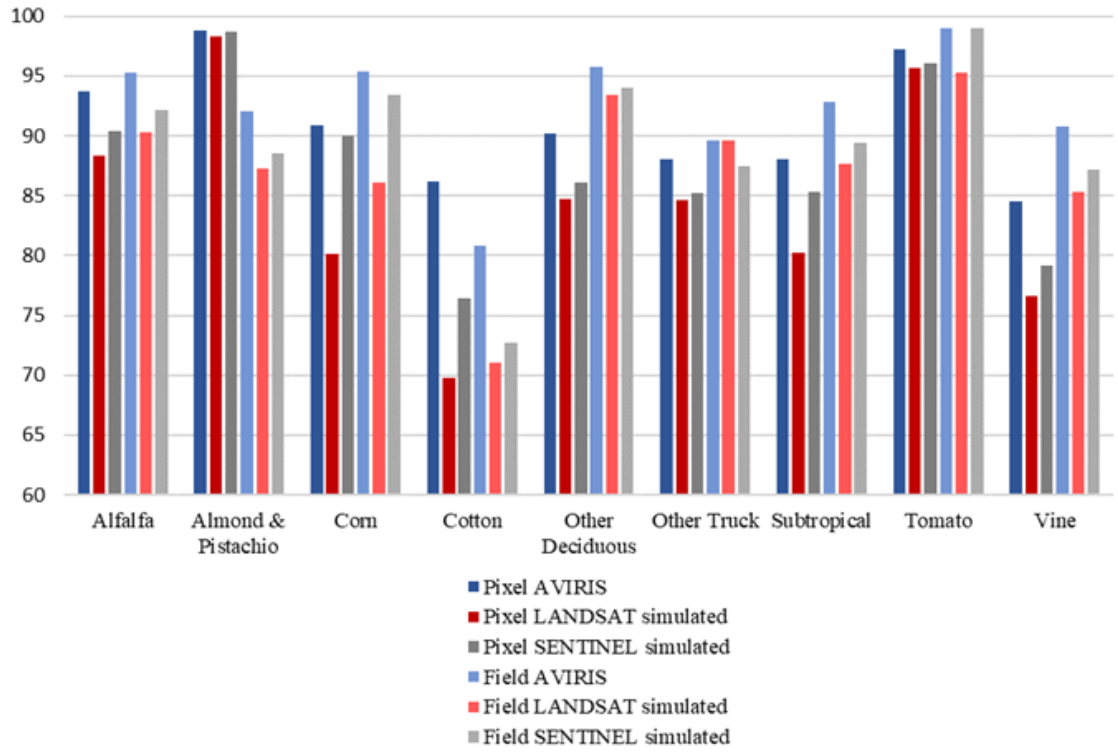

Figure 2.4. Pixel-level and field-level percent accuracies for random forest run with the Airborne Visible/Infrared Imaging Spectrometer (AVIRIS), Landsat-simulated, and Sentinel-2B-simulated imagery. Pixel-level accuracy reported as the random forest OOB accuracy. Field-level accuracy is reported as the average of the producer's and user's accuracies for all three years. Field-level accuracies contained all of the classified fields with 50% GV or more.

2.3.1.6. Portability Assessment

The portability of the hyperspectral random forest classification was tested by training the random forest on two of the three years, and then using that random forest to classify the third year. Accuracy was assessed at the field level. The results of the portability runs show

high variability in accuracy between years (Table 2.7). For example, other deciduous crops had a high accuracy of approximately 87% when classifying fields in 2013 and 2015, but accuracy of only 54.1% in 2014. Other truck crops and cotton had the lowest accuracies in every year, with tomato crops being completely unable to be classified without a multi-year library, and cotton having a highest yearly accuracy of only 32.1%. Other truck crops and tomatoes had NA accuracies in some years, which resulted from a user's accuracy of NA that was calculated when dividing zero correctly classified fields by zero total fields classified as that crop. Almond and pistachios had the greatest consistency in accuracy across the three years, with changes in accuracy of less than 10% between the three years.

Table 2.7. Field-level accuracies, reported as the average of the producer's and user's accuracies, for random forest (RF) runs trained on the two years that it was not used to classify. The percentage decrease in accuracy is the difference between the accuracy of RF trained with all three years (Table 2.3) and the RF trained with two years. Field-level classification used a majority filter on fields with 50% GV or higher.

Crops	**Field-Level Accuracy (%)**			**Percent Decrease in Accuracy**		
	2013 Trained on 2014 and 2015	**2014 Trained on 2013 and 2015**	**2015 Trained on 2013 and 2014**	**2013**	**2014**	**2015**
Alfalfa	74.7	54.1	87.4	19.5	40.6	9.7
Almond and Pistachio	71.1	66.7	70.5	17.8	25.0	25.1
Corn	86.7	68.8	89.9	11.6	25.1	4.2
Cotton	28.3	0	32.1	45.0	83.3	53.6
Other Deciduous	87.0	54.1	87.3	8.6	41.2	9.3
Other Truck	NA	NA	0	NA	NA	68.8
Subtropical	78.2	62.3	66.5	14.1	30.9	26.4
Tomato	100	NA	61.8	0	NA	35.3
Vine	71.9	61.3	78.3	16.4	29.3	15.1

2.3.2. Central Valley Case Study: Changes in Cropping Patterns

Visual analysis of the crop classification maps from 2013, 2014, and 2015 showed overall good cohesion between the general spatial patterns throughout time. Figure 2.5 shows the field-level classification of the study area from 2013 as an example of the overall cropping patterns that did not shift over the course of the drought, while figures 6 and 7 highlight finer scale changes in cropping over the course of the drought. The subtropical, other deciduous, and vine crops were concentrated in the northern part of the study area, and the almond and pistachio fields were mainly in the southern portion of the site. The other crop types were scattered throughout the flight line.

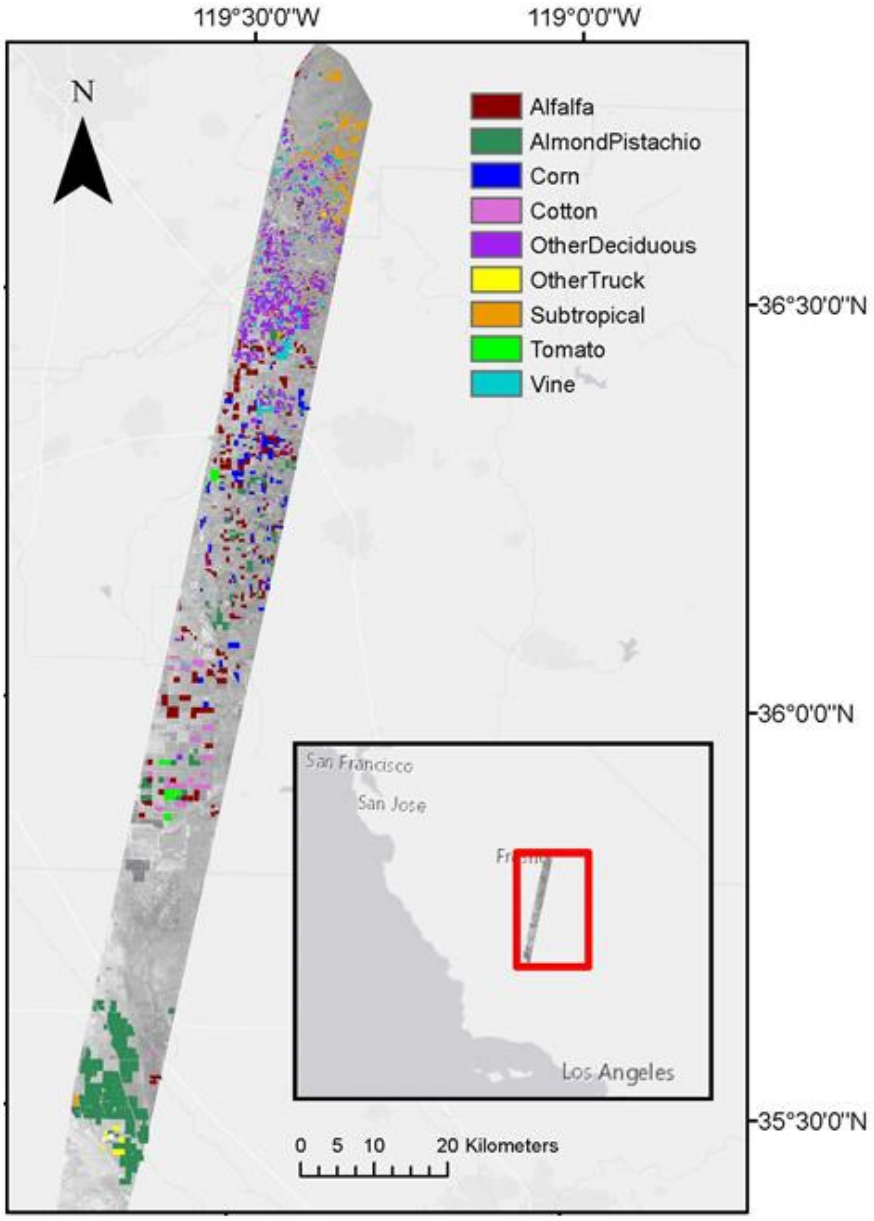

Figure 2.5. 2013 classification map using the majority filter.

The number of fields classified in each year declined over time, with a decrease of around 100 fields a year (Table 2.8). Table 2.8 also details the percentage of these classified fields that were included in the validation layer for that year. The results showed that overall, 58.7% of the classified fields were not included in the validation polygon layer. This discrepancy reflected incomplete data in the county crop maps, indicating that a majority of the actively growing fields in the study area were not recorded in the pesticide-permitting database. This underscores the value of remote sensing methods for analyzing the planted crop area.

Table 2.8. Number of classified fields each year.

	Classified Fields
2013	
Percent included in validation layer	39.0%
Percent not included in validation layer	61.0%
Total number classified	3469
2014	
Percent included in validation layer	36.4%
Percent not included in validation layer	63.6%
Total number classified	3361
2015	
Percent included in validation layer	48.9%
Percent not included in validation layer	51.1%
Total number classified	3235

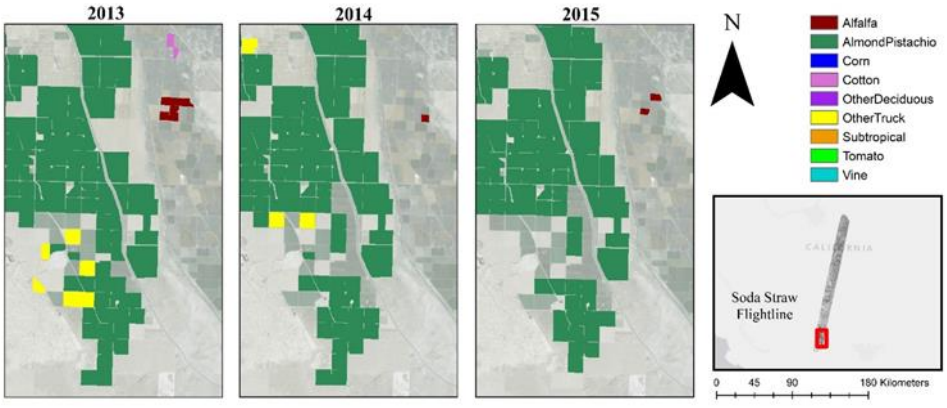

Figure 2.6. Portion of the southern study area (midpoint: 35°27′42 E, 119°40′33 N), illustrating the decrease in area of other truck crops, alfalfa, and cotton over the drought with relative stability in area of almond and pistachios.

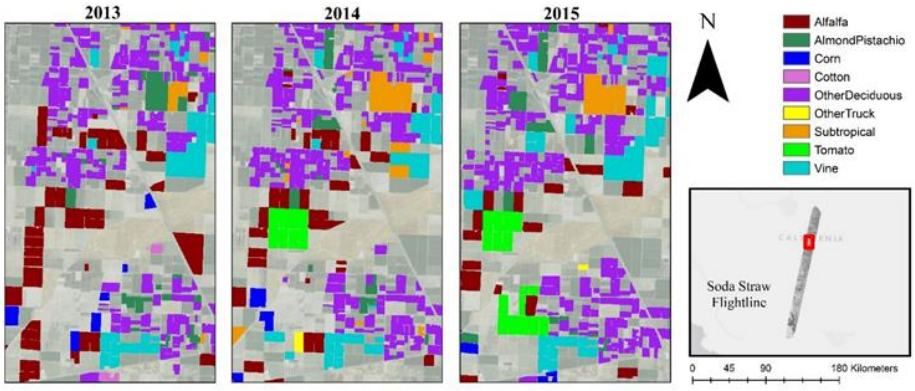

Figure 2.7. Portion of the northern study area (midpoint: 36°20′36 E, 119°28′30 N) highlighting an increase in tomato extent over the course of the drought as well as a decrease in alfalfa extent.

Summation of the crop area from 2013 to 2015 (Table 2.9) showed that, similar to the number of fields classified, the overall crop area declined each year, with approximate declines of 32 km^2 over two years. Alfalfa, cotton, corn, and truck crops all showed marked declines from 2013 to 2015 with decreases in area of approximately 29%, 50%, 84%, and 89%, respectively, in those two years, as exemplified in Figure 2.6. Tree crops including almond and pistachio, other deciduous trees, and subtropical crops showed some fluctuations over the three years, but had overall greater consistency over time than the other crop classes. From 2013 to 2015, those three tree crop categories showed the smallest fluctuations in crop area, with less than 7% overall change for any of those groups. Tomatoes and vines were the two categories that increased over the course of the drought, with tomatoes showing a 128% increase and vines a 34% increase from 2013 to 2015 (Figure 2.7; Table 2.9).

Table 2.9. Classified crop area.

Crops	Cropland (km^2)			Change in Area		
	2013	**2014**	**2015**	**2013 to 2014**	**2014 to 2015**	**2013 to 2015**
Alfalfa	68.6	57.1	48.7	−16.8%	−14.6%	−28.9%
Almond and Pistachio	124.9	131.5	128.2	5.3%	−2.5%	2.6%
Corn	25.1	14.0	12.7	−44.3%	−9.5%	−49.6%
Cotton	17.2	1.5	2.7	−91.4%	85.4%	−84.1%
Other Deciduous	74.2	77.8	76.7	4.8%	−1.4%	3.4%
Other Truck	3.4	3.4	0.4	0.3%	−89.4%	−89.4%
Subtropical	26.6	34.7	24.9	30.3%	−28.4%	−6.7%
Tomato	6.9	5.7	15.8	−18.0%	178.2%	128.0%
Vine	16.0	17.7	21.2	11.0%	19.7%	32.9%
Total	362.9	343.3	331.2	−5.4%	−3.5%	−8.7%

2.3.3. Central Valley Case Study: Crop Area in Relation to Environmental and Economic Drivers

Using average water inputs per area in the Tulare Lake Hydrologic Region for each of these crop categories, the estimated required water inputs are shown in Table 2.10. The overall water requirement of the study site was estimated to have declined over the course of the drought by around 0.02 km^3 of water yearly, due to increases in fallowed land. Figure 2.8 shows an average water requirement per crop group by the change in planted area from 2013 to 2015 to better understand whether the water requirement of a crop was a key factor in planting decisions. This analysis revealed no strong correlation between the change in crop area and average water inputs, showing that the crops that needed the largest water inputs did not experience larger declines in area than the crops that required less water.

Table 2.10. Estimated water inputs per year calculated using the median water application by crop type in the Tulare Lake Hydrologic Region from 1998 to 2010 (CA DWR, 2017) and the classified area (Table 2.9).

	Average Water Application per Hectare (Thousand m^3)	Total Water Application (km^3 Multiplied by 1000) Calculated with the Classification Maps		
		2013	2014	2015
Alfalfa	15.1	103.9	86.5	73.8
Almond and Pistachio	12.4	154.6	162.7	158.7
Corn	9.6	24.2	13.5	12.2
Cotton	9.4	16.1	1.4	2.6
Other Deciduous	11.9	88.2	92.4	91.2
Other Truck	4.3	1.5	1.5	0.2
Subtropical	9.8	26.1	33.9	24.3
Tomato	6.9	4.8	3.9	10.9
Vine	8.2	13.0	14.5	17.3
Total		432.3	410.3	391.1

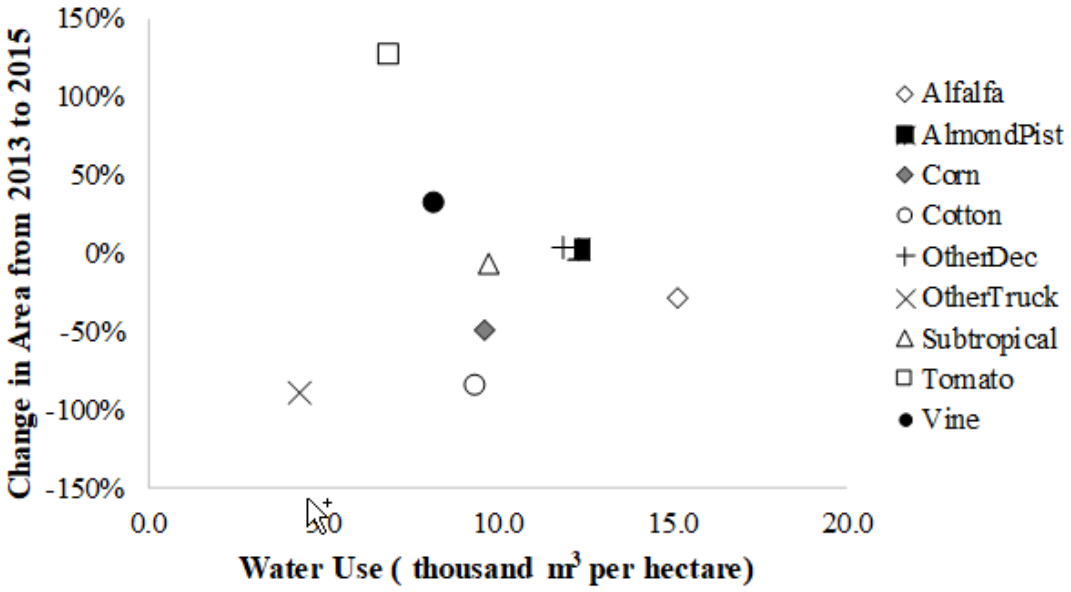

Figure 2.8. Assessing correlation between the change in crop area over the drought (Table 2.9) and the average water use of each crop (Table 2.10).

Crop market value, crop value per unit water, and shifts in value over the drought may have played a role in planting decisions. It is interesting to note that tomatoes and grape vines were the two crops that showed increases in area as the drought progressed, and they are also the crops that have a high value per area. In 2014, fresh tomatoes had an average value in

California of $27,088 per hectare and grapes (all varieties, wine and raisin) of $14,960 per hectare. By contrast, the value per hectare for alfalfa, corn, and cotton were $3121, $1915, and $5772, respectively (CDFA, 2015). While a detailed economic analysis is outside of the scope of this paper, the increase in area of higher value crops over the course of the drought is noteworthy and warrants further study.

Finally, crop lifespan was analyzed in conjunction with changes in cropping area. Figure 2.9 shows changes in cropping area from 2013 to 2015 segmented by the average number of years that a crop is in production once planted. The results showed the greatest declines occurred in annual crops. The mid-lifespan group had smaller percentage declines, and the long lifespan group showed a small increase in the percentage of crop area over the span of the drought. The results indicated that there is a correlation between lifespan and change in crop area that is likely to be of importance when studying the agricultural impacts of future drought events.

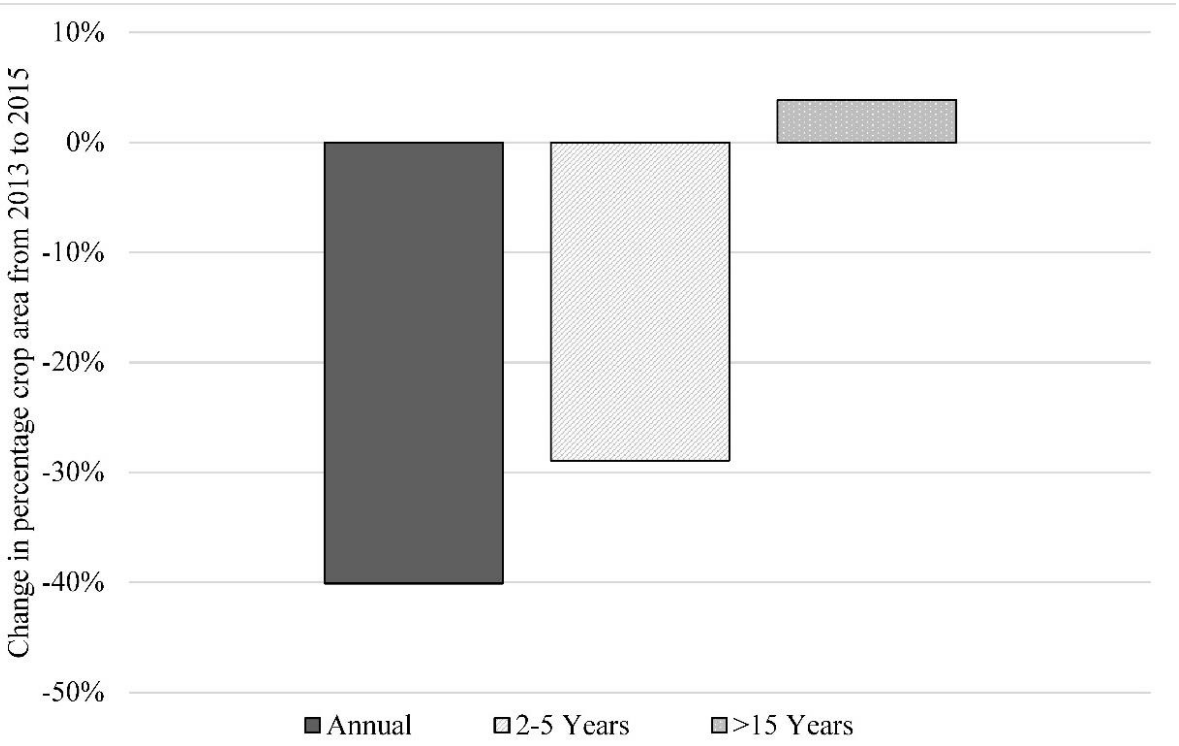

Figure 2.9. Change in percentage crop area by crop lifespan. Annual crops include corn, cotton, other truck crops, and tomatoes. The two to five-year range includes alfalfa. The greater than 15-year group includes almond/pistachio, other deciduous crops, subtropical, and vines.

2.4. Discussion

2.4.1. Challenges and Caveats

Mapping crops is an integral part of understanding the water budget and needs of agricultural areas. However, mapping managed vegetation with remote sensing presents a set of challenges that are unique from natural vegetation. For one, annual crops are regularly planted, grown, harvested, and fallowed within a few months' time. Land cover can change rapidly, and fields include crops in various stages of growth that may lead to large variations in plant cover, soil fraction, and shade. Secondly, crops are actively managed. Two fields of the same crop, side by side, may receive different management strategies in regard to pesticides, planting geometry, soil additives, soil type, irrigation system and schedule, and

the timing of planting. These differences may lead to significant spectral variations within crop types (Galvão et al., 2016; Pinter et al., 2003). Thirdly, because crops are commonly rotated and fallowed, validation information needs to be precise in time in order to accurately capture the agricultural landscape that coincides with the flight schedule. The goal of this study was to determine how useful remotely sensed crop maps could be, given these caveats, for agricultural management at a regional level.

Our estimates of crop extent may have been affected by different sources of error. First, because this study used a cutoff of 50% green vegetation or more at the pixel and field level, the final map likely undermapped crop area. Of the 8272 total fields registered in the validation data layers as having a crop growing at the time of the flights, 4114 (49.7%) had between zero and 50% green vegetation as assessed by MESMA, and were therefore not included in the analysis. Fields with less than 50% GV fraction could be indicative of recent harvests, new plantings, young crops, or fallowed land, which do not all result in the undermapping of active crop area. Additionally, because of this threshold, yearly changes in crop extent, particularly of tree crops, could indicate growth of a crop instead of a new planting. For example, a field of almond trees may have a 45% green vegetation fraction in 2013, 48% in 2014, and 51% in 2015. In this case, the almond field would only be mapped in 2015, and would imply a sudden increase in planted almond extent, although it had existed for multiple years. Underestimating area is not unique to our study; it is a challenge of hard classifications in general. Areal estimation of classes that are changing tend to be underestimated, while the magnitude of that change is overestimated when classified pixels are multiplied by the pixel size to the estimated area (Foody, 2002). One possible solution is to apply a regression correction such as implemented by the National Agricultural Statistics

Service's Cropland Data Layer (CDL). The CDL correction uses a sample site with ground-truth area data to formulate a regression between CDL estimates and truth that is then applied to the CDL data to adjust the estimates (Johnson, 2013). Such a correction would be advantageous for future studies, but it does require additional on-the-ground validation data that was not available for this study.

Second, some green fields in the study area contained a crop that was not included in one of the nine mapped crop groups. However, the crops that were not included in the study comprised less than 1% of the crop area, so the errors associated with their absence in the study are assumed to be low. Third, crop rotation may be one reason that the extent of annual crops fluctuated more than the perennial crops. Crop rotation was not accounted for in our crop extent estimates, as one image per year is not adequate for capturing such changes. However, if crops are being rotated, we would still expect the total area of annual crops to stay somewhat stable through time, even if specific annual crops showed large fluctuations. Our finding that the total area of annual crops declined with drought is therefore not likely to be attributable to crop rotation.

Finally, given that the study only used one time point in June for each of the three years, changes in estimated area could be indicative of a change in the timing of planted crops in addition to actual fallowing or crop substitution. For example, if farmers planted their tomato fields three weeks later in 2014 than they planted them in 2013, the tomatoes may not have reached the 50% green vegetation threshold by early June in 2014, which would have led to underestimates of tomatoes in that year. Other studies have relied on time series analyses to confirm fields as fallow (Alcantara et al., 2012; Wu et al., 2014), which suggests that a

satellite-based imager with a moderate spatial resolution such as Landsat OLI could be used in tandem with aerial imagery to enhance the validity of fallowing results.

2.4.2. Crop Classification with Imaging Spectroscopy

The classification results showed high overall accuracies of over 89% at the pixel level and 94% at the field level. High accuracy was expected, in accordance with previous studies that have discriminated crop types with hyperspectral sensors, but these results are unique in that they discriminate crops in a highly diverse agricultural landscape as compared to previous studies that largely focused on large-plot, staple crops (Bandos et al., 2009; Camps-Valls et al., 2003; Galvão et al., 2005; Galvão et al., 2009; Mariotto et al., 2013; Rao, 2008). Therefore, the results of this classification enhance the practical relevance of using an imaging spectrometer in agricultural areas that host a large variety of crop species, such as California.

The accuracies obtained in this study from AVIRIS exceeded those from simulated Landsat OLI and Sentinel-2B imagery, although even the Landsat and Sentinel results had high accuracies at the field level of above 85% accuracy for eight of the nine crop categories. The increased accuracy of AVIRIS over multispectral sensors is in contrast with the results of Clark (2017), who found no classification improvement of hyperspectral data over multispectral data when classifying land cover in California, but showed similar results to Platt and Goetz (2004), who found modest advantages of AVIRIS over Landsat for classifications at the urban–rural fringe. Since true Landsat and Sentinel imagery will have coarser spatial resolutions and a worse signal-to-noise ratio, we hypothesize that the accuracies of this classification would decrease if actual imagery, and not simulated imagery, were used. However, given the high accuracies of the simulated data, it seems that the extra

spectral bands of AVIRIS, while somewhat advantageous for crop classification, do not confer a large added benefit over the 12 Sentinel bands.

The sensor comparison and the results of the band importance analysis imply that 172 spectral bands, such as those that were used in this study, are somewhat redundant and could likely be pared down without losing much accuracy. The band analysis highlighted the most important wavelengths and regions of the spectrum for the random forest classifier, and pointed to biochemicals and structure as drivers of crop discrimination. The 400–750 nm region was particularly significant, especially the blue and red-edge regions, showing that the shape of the green peak and the chlorophyll absorptions provide valuable information for crop discrimination. The red-edge region has been shown to vary by vegetation stress, species, and time of year, which can all change the slope and inflection point of the red edge [67–69]. The blue region is sensitive to chlorophyll-a absorption and has been linked to senescence, carotenoids, and browning (Thenkabail et al., 2004; Tucker, 1977). The finding that these two regions are important for crop discrimination is similar to Immitzer et al. (2006), who found the red edge and the blue bands to be the two most important bands for crop classification using Sentinel-2 data. Sentinel-2 contains three bands in the highly valuable red-edge region that may partially account for its ability to classify crops at accuracies that rival AVIRIS. However, when comparing the blue region, this study found bands 414 nm and 424 nm to be of high value for crop discrimination, which are shorter than the Sentinel blue band at 490 nm. The importance of the shorter wavelength blue bands, bordering on the ultraviolet (UV) region, suggests that the UV may contain a wealth of crop information concerning characteristics such as wax deposition and metabolites such as flavonoids and phenolics (Kakani et al., 2003) that could be utilized for discrimination if

atmospheric scattering did not inhibit its use. Outside of the visible range, the liquid water feature at 957 nm was identified as important, and many of the bands near the edges of liquid water regions show high band importance. This result suggests that plant water content and structure are important drivers of discrimination (Clark, 2017).

While AVIRIS showed modestly higher accuracies for single image crop classification over Sentinel-2 and Landsat OLI, hyperspectral and multispectral imagers each have unique strengths that can be complementary for agricultural analysis. Multispectral data may be preferred to hyperspectral data for its ease of use, shorter processing times, and high temporal resolution. With rich time series of data, multispectral imagers are especially valuable for agricultural analysis in application areas such as crop rotation, fallowing, and crop development, and have shown high accuracies when discriminating crops using time series (Vuolo et al., 2018; Wardhoff et al., 2017; Wardlow & Egbert, 2008; Wu et al., 2014). However, time-series data is not always acquirable, especially in cloud-prone areas. Hyperspectral imagers have high discriminating power that allow for more accurate single-date classifications that would be highly useful in these areas. The added information in hyperspectral spectrometers also allow for more accurate mid-season growing assessments before time-series data become available. Moreover, beyond classifications, the narrow bands of hyperspectral imagers make them well-suited for attaining biochemical and physiological plant information (Galvão et al., 2013, Thenkabail et al., 2013). Therefore, the combination of these two technologies can allow for classifications under a broad range of circumstances (mid-season versus end of season) and spatial areas (cloud prone versus clear) combined with additional analyses of biochemical properties, fallowing patterns, and development that can be of high importance for agricultural researchers and managers.

The increased accuracy of field-level classification results over pixel-level results with AVIRIS suggest that it would be important to first develop an accurate map of agricultural field boundaries if this method were to be applied in other agricultural areas where GIS data on farms do not already exist. A possible solution is to use an automated computational methodology that extracts individual crop fields from Landsat ETM and TM time series, as detailed in Yan and Roy (2016). This field extraction technique or other object-oriented methods could be used to identify fields for future crop classification studies.

One challenge of mapping crops is the portability of a methodology across time. First, crops imaged at different times are in many different phenological stages. We aimed to capture phenological variability through a multispectral library as suggested by Dudley et al. (2015), who found that the more variability that is captured within the training data, the more portable the method. We hypothesize that the high degree of variability between accuracies trained on two images and tested on a third is attributed partially to how much of the total variability was captured by the two images. For example, the accuracy of corn in 2014 and trained with 2013 and 2015 was 68.8% as compared with 86.7% and 89.9% in the other two years. It is possible that corn in 2013 and 2015 was in a more similar phenological stage than the corn in the 2014 imagery, so a training library from 2013 and 2015 was unable to capture the spectral variability of corn in 2014. These results suggest that a larger training dataset that includes more variability through additional spectra from other years or other times of year could enhance the portability. Second, portability has to do with the consistency of the dataset and data products. The reflectance retrieval of the AVIRIS images left visible spectral artifacts that varied by image date. Since AVIRIS is an airborne spectrometer and the data products are not automated to the same degree as those from a satellite such as Landsat, there

is variability between image products that make portability even more challenging. A spaceborne imaging platform would minimize these challenges and increase the consistency of the products.

It is important to note that the assessed accuracies of this study's classification are with the assumption that the validation layer is 100% accurate, which may not be true. Given that the accuracy of the validation layer relies upon timely and accurate permit filing by farmers and the appropriate registration of such information by the county, errors may be present in the data. However, if there are errors in the validation layer, they would contribute to confusion in the classification, thereby producing an accuracy that is lower than it really is. Therefore, we assume that the true accuracy of the classification is as high or higher than the assessed accuracies. With perfect validation data, it may be possible to increase accuracy.

2.4.3. Implications for Agricultural Management

This study's findings of fallowing and changes in plantings over the course of the drought, along with the assessed linkages to relevant drivers, serve as a case study to better understand the utility of crop classifications in drought-prone areas that rely on irrigation. Our results concerning the cropped area and possible drivers are consistent with other economic, policy, and scientific analyses of the 2012–2016 California drought (Cooley et al., 2015; Howitt et al., 2014; Melton et al., 2015; Medellin-Azuara et al., 2015; Tortajada et al., 2017). Table 2.9 shows that as the drought worsened, overall crop area decreased in the study area, which is a finding that echoes similar assessments of fallowed cropland over California during this drought (Melton et al., 2015), and is in line with expectations that times of drought will limit water and force declines in crop production. However, fallowing was not uniform across crop groups. Our finding that there were larger declines in annual field crops than

perennial crops is consistent with a study by Melton et al. (2015) that reviewed data from the County Agricultural Commissioner offices and found that perennial crops showed little change in area due to drought, while annual crops experienced significant increases in fallowing. The agreement between our findings and other similar analyses adds confidence to the accuracy of the results, and implies that our study, although only in a portion of the Central Valley, has results and implications that may be applicable to California agriculture as a whole.

When analyzing changes in plantings in conjunction with possible drivers of planting decisions, our results suggest that farmers' decisions regarding which crops to grow in times of drought were not proportional to their water requirements. The reason that crop water requirements were not a main driver of cropping patterns may have been, in part, due to the increases of groundwater pumping that partially offset the shortage of surface water availability during the drought (Howitt et al., 2014). Tortajada et al. (2017) noted that during the drought, farmers coped with less surface water by fallowing fields, buying water from other farmers, or pumping groundwater. Since some farmers were able to offset surface water losses by acquiring water through other means, fallowing fields was not as prevalent as might be seen in a rain-fed agricultural area where groundwater may not be accessible. This finding highlights the importance of case studies such as this one for irrigation-dependent areas that are prone to drought, such as California. The total cropped area in our study area did decline, suggesting that groundwater pumping and water trading partially offset surface water losses, but did not fully offset drought impacts. Further, fallowing fields appears to be favored over changing crops as a strategy employed to save water. However, although a switch to more water-efficient crops was not observed, farmers may have changed their irrigation system,

watered less frequently, watered less intensely, or any of a variety of other possible water-saving strategies. For a full picture of water use, crop mapping could be combined with measures of water stress, crop health, or soil moisture for a better understanding of the total crop water budget.

Crop values and the lifespan of a crop are potential drivers of planting decisions that did show promising correlations with changes in planted area. As perennial crops frequently have higher value than annual crops, the two factors are discussed in tandem. The results suggested that farmers shifted their planting choices in favor of more lucrative perennial crops. This idea is supported by many drought analyses, which found that farmers in California respond to water scarcity by fallowing lower value-per-unit-water crops (Hanak et al., 2011), and specifically during the 2012–2016 drought switched from lower-value field crops to higher-value nut and fruit crops (Cooley et al., 2015; Howitt et al., 2014; Medellin-Azuara et al., 2015).

Our results are consistent with those of Tortajada et al. (2017), who found that farmers will prioritize factors such as the price of goods, net income, and consumer preferences over water requirements if alternative water supplies, such as groundwater, exist during drought. These results have implications for the impact of future droughts on agricultural adaptation and management. With more extreme dry periods in the future, California may begin to see a shift toward fewer annual plantings and toward more stable, lucrative crops such as fruit and nut trees, as scarcity in water shifts economic value and farmers are faced with a need to optimize water and land. However, shifts driven by economic value or crop permanence will not necessarily lead to diminished water requirements. Although fallowing will reduce agricultural water demands, preference to plant fruit and nut trees instead of field crops could

increase relative agricultural water needs. This result exemplifies the idea of maladaptation to drought, which was posited in Christian-Smith et al. (2015), who stated that coping strategies to drought can often lead to the increased vulnerability of a system. In this case, farmers may be shifting to crops that may actually put more pressure on limited water resources.

2.5. Conclusions

This study used imagery of high spatial and spectral resolution to obtain highly accurate classifications of crops into groups of similar water use. The results showed classification accuracy of over 94%, and allowed for an analysis of crop area and cropping patterns in situations of droughts. The classification results show that an imaging spectrometer improved crop classification accuracy over multispectral sensors. Crop maps produced from the classifier showed annual patterns that were consistent with other economic and scientific analyses of the 2012–2016 drought, and showed that farmers are fallowing fields and switching to higher-value perennial crops as an adaptation strategy when water becomes scarcer. This study supports the idea that a spaceborne imaging spectrometer with high temporal resolution, such as the planned HyspIRI mission (Lee et al., 2015), could successfully be used for near real-time or within the growing season mapping of diverse agricultural crops and quantification of an area in cultivation. The demonstrated ability of an imaging spectrometer to produce high crop classification accuracies that are in general in agreement with other published cropping trends increases confidence in the validity of the results and shows that an imaging spectrometer with frequent temporal resolution could enable policymakers, scientists, and farmers to quickly and easily monitor changes in

planting with drought. These changes have broad impacts on food yields, pest and disease management, water resource accounting, soil health, and California's economy.

2.6 Supplementary Material

Table S1: Error matrix for reference fields (5,801 total) from the majority filter reclassification for all years combined. This error matrix only includes fields with 25% of more green vegetation. Abbreviations are used for crop groups: Alfalfa (AF), Almond/Pistachio (AP), Corn (CR), Cotton (CT), Other Deciduous Crops (OD), Other Truck Crops (OT), Subtropical (ST), Tomato (TO), and Vine (VI).

		Reference Data									
		AF	**AP**	**CR**	**CT**	**OD**	**OT**	**ST**	**TO**	**VI**	**Total**
Classified	**AF**	**372**	5	1	4	16	0	2	1	12	413
	AP	11	**553**	7	23	165	6	86	4	61	916
	CR	2	0	**92**	1	1	0	0	0	0	96
	CT	1	0	1	**32**	2	1	0	0	0	37
	OD	26	12	2	5	**2563**	9	89	0	87	2793
	OT	0	0	0	0	0	**23**	0	0	0	23
	ST	12	19	0	0	100	0	**947**	0	49	1127
	TO	0	0	0	0	0	0	0	**29**	0	29
	VI	1	0	0	0	10	1	2	0	**353**	367
	TO	425	589	103	65	2857	40	1126	34	562	
	User's Acc.	90.1%	60.4%	95.8%	86.5%	91.8%	100%	84.0%	100%	96.2%	
	Producer's Acc.	87.5%	93.9%	89.3%	49.2%	89.7%	59.0%	84.1%	85.3%	63.0%	

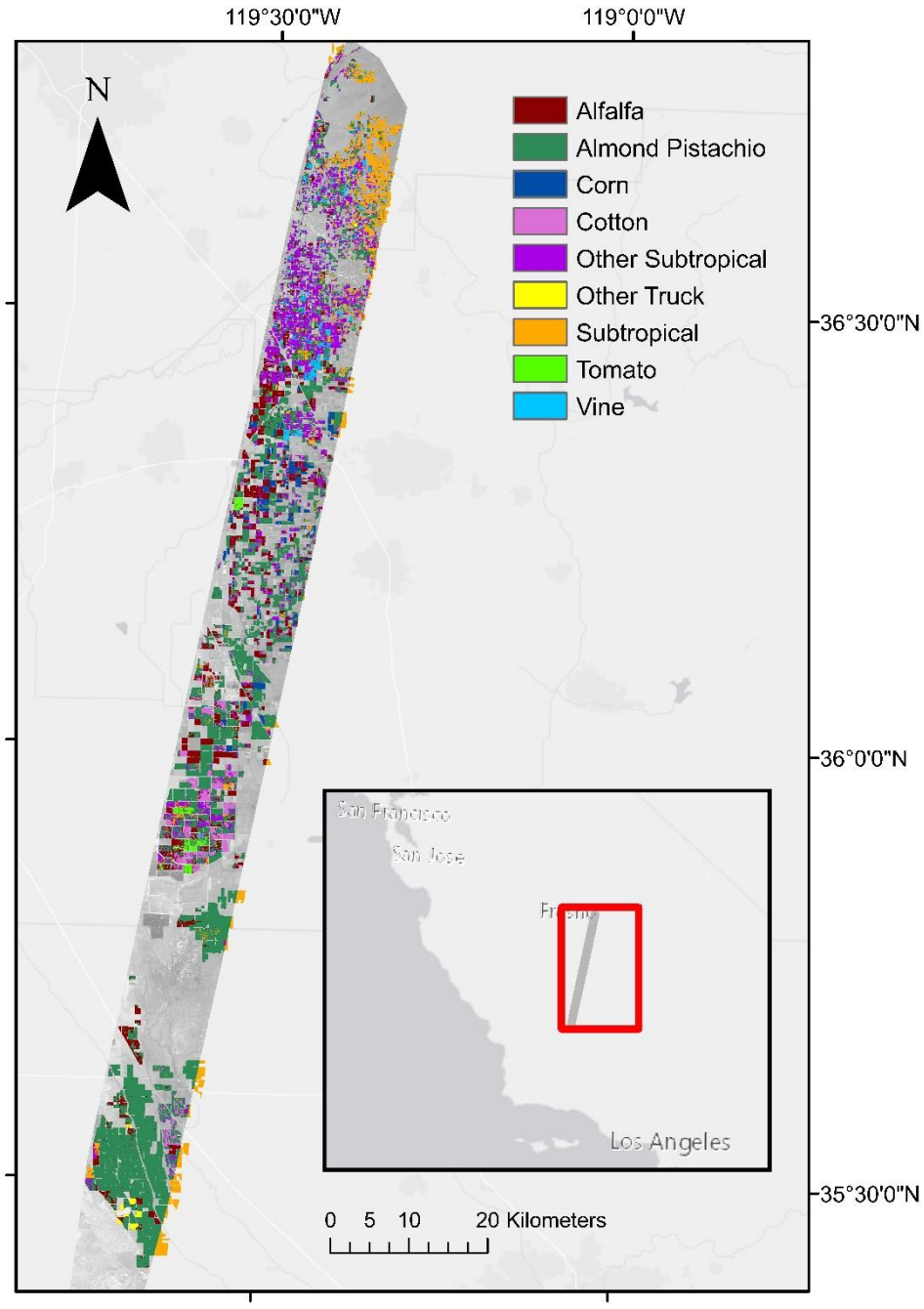

Figure S1: 2013 pixel-level classification map before using a majority filter and 50% GV field threshold

Chapter 3: Using paired thermal and hyperspectral aerial imagery to quantify land surface temperature variability and assess crop stress within California orchards

With Dar A. Roberts and Joseph P. McFadden

This chapter is based on a manuscript published in the journal of *Remote Sensing of Environment*:

Shivers, S.W., Roberts, D.A., & McFadden, J. (2019). Using paired thermal and hyperspectral aerial imagery to explore land surface temperature variability and assess stress within California orchards. *Remote Sensing of Environment*, Volume 222, 2019, Pages 215-231.

3.0. Abstract

Remote sensing can inform agricultural knowledge of crop water use through observation of land surface temperature, which can act as an indicator of plant function and health. This study uses remotely sensed data to quantify thermal variability within fruit and nut orchards during an intense drought period in California's Central Valley (2013-2015). First, fractions of green vegetation (GV), non-photosynthetic vegetation (NPV), and soil were derived for a variety of crop species using visible-shortwave infrared (VSWIR) spectra imaged by the Airborne Visible/Infrared Imaging Spectrometer (AVIRIS). Fractional estimates were then used to select thermal endmembers for each class using simultaneously collected MODIS/ASTER Airborne Simulator (MASTER) thermal imagery and a crop species map. Expected pixel temperatures of non-stressed crop fields were then modeled, and the per-pixel difference between measured and expected temperatures was calculated as a temperature residual. Crop residuals serve to capture variability in temperature that may be attributable to differences in crop health and/or management practices. We found multiple distinct thermal classes to exist across the study site. Furthermore, crop temperatures correlated to expected crop ET rates, and temperature residuals showed correlations to changes in crop yields during the study period. Further assessment of findings revealed an increase in temperature residuals during the study period that is consistent with increasing stress, likely linked to the progression of drought. The method presented here shows utility for regional agricultural analysis of crop water use and is particularly relevant for ECOSTRESS and the upcoming Surface Biology & Geology mission.

3.1. Introduction

Agricultural water stress can lead to diminished yields and decreased crop quality that have implications for food supplies, ecosystem health, and agricultural management (Alderfasi & Nielsen, 2001; Irmak, et al., 2000; Rosegrant et al., 2009; Schmidhuber & Tubiello, 2007). Thermal remote sensing can observe spatiotemporal patterns of crop functioning to identify and quantify water stress in order to optimize resource allocation and mitigate losses (Anderson et al., 2012; Jackson et al., 1981; Moran et al., 1994). However, the stress signal, in the form of elevated crop temperatures, is obscured by confounding factors, such as species-specific canopy temperatures (Idso et al., 1981), fractional cover (Idso et al., 1966; Nemani & Running, 1989), soil moisture (Idso et al., 1975), and surface structure (Jones et al., 2009; Leinonen & Jones, 2004), that add additional thermal variability and complicate stress comparisons between pixels. The goal of this work is to use medium-resolution thermal infrared imagery (TIR) to evaluate crop stress in California orchards by controlling for thermal variability not attributable to stress with spatially coincident hyperspectral imagery.

Land surface temperatures (LST) can be used to assess differences in plant stress levels associated with availability of water (Jackson et al., 1981; Quattrochi & Luvall, 1999; Tanner, 1963). When plants do not have sufficient water, stomatal closure results in elevated leaf and canopy temperatures due to decreased transpiration (Jackson et al., 1981). However, the spatial resolution typical of spaceborne thermal imagery (0.1-5 km) results in mixed pixels of varying types of crops, soil, and nonphotosynthetic vegetation (NPV) that make detailed knowledge of surface characteristics necessary for interpreting the thermal signal. LST and fractional vegetation cover have an inverse relationship leading pixels

containing more green vegetation (GV) to have lower temperatures in water-limited regions (Carlson et al., 1994; Karnieli et al., 2010). The dynamics of this relationship, however, are dependent upon the type of GV as not all vegetation shows the same thermal responses. Species have been found to have unique temperature signatures given differences in architecture, such as canopy shade, leaf size, canopy density, boundary layer resistance, and plant height, and differences in physiology such as stomatal behavior and evapotranspiration rates (Idso et al., 1981; Leuzinger & Korner, 2007; Scherrer et al, 2011). In addition, the moisture level of soil is highly correlated to its surface temperature, complicating thermal interpretation of mixed pixels of soil and vegetation (Idso et al., 1975).

Current remotely sensed estimates of stress face a tradeoff between incorporating this thermal complexity and allowing for scalability, inhibiting regional analyses of stress between different types of crops. While studies with limited spatial coverage and high-resolution imagery can account for much of the external thermal variability in the landscape through field-specific parameters, stress identification on a larger scale requires simplification of stress metrics that allow for pivotal drought monitoring but cannot capture much of the thermal complexity on the ground.

At a field-level scale, high-resolution TIR imagery from unmanned aerial vehicles (UAVs) or aircraft have been used to study crop water stress in grapevines (Bellvert et al., 2014; Möller et al., 2006), cotton (Alchanatis et al., 2010), wheat (Millard et al., 1978), olives (Ben-Gal et al., 2009; Berni et al., 2009; Sepulcre-Cantó et al., 2006), peaches (Gonzalez-Dugo et al., 2013; Sepulcre-Cantó et al., 2007), beans (Jones 1999), rice (Jones et al., 2009), citrus (Zarco-Tejada et al., 2012), almonds, apricots, lemons, and oranges

(Gonzalez-Dugo et al., 2013). These studies have shown a link between plant temperatures and canopy conductance, leaf water potential and irrigation regimes, and have shown that thermal imagery can detect even mild stress (Sepulcre-Cantó et al., 2006). However, while highly useful for refined understanding of stress within imaged trees, the methods are not scalable to larger areas due to their crop-specific ground inputs and need for imagery at a fine spatial resolution for tree crowns to be targeted and soil and shade effects minimized. Many of these studies use the Crop Water Stress Index (CWSI; Idso et al., 1981), which relates the difference between air and canopy temperatures to a baseline temperature difference for a non-water stressed crop as a function of the atmospheric pressure deficit. However, Idso et al. (1981) found that due to differences in crop physiology, well-watered crops have unique thermal relationships and baseline non-water stressed temperatures. For this reason, when the CWSI is applied to agricultural areas with a diversity of crop species (Gonzalez-Dugo et al., 2013), the model parameters used to identify stress need to be optimized for each crop type by using varying non-water stressed thermal baselines. Further, the CWSI does not account for fractional cover and therefore has a major limitation that it can only be applied to fully vegetated fields or isolated tree crowns. One way to overcome this limitation is to use Moran et al.'s (1994) Water Deficit Index (WDI), which alters the CWSI so that it can be applied to partially vegetated fields. It combines spectral vegetation indices with thermal data to evaluate water stress. However, required inputs of net radiation, vapor pressure deficit, wind speed, air temperature, maximum possible plant height, minimum soil roughness, minimum and maximum Soil-Adjusted Vegetation Index, maximum possible leaf area index (LAI), and minimum and maximum

possible stomatal resistances make the method difficult to implement over large areas (Moran, 2004).

On the other hand, satellite-based stress metrics based on TIR data, such as the Vegetation Health Index (VHI; Kogan, 1997) and the Evaporative Stress Index (ESI; Anderson et al., 2007a; 2007b; 2011), use coarse resolution imagery and a wide spatial scope to monitor vegetation health over large areas. The VHI uses a combination of LST and the Normalized Difference Vegetation Index (NDVI) to assess stress with the core assumption that NDVI and temperature are inversely correlated while the ESI calculates stress as an anomaly between actual evapotranspiration (ET) and potential ET, as calculated using the Atmosphere-Land Exchange Inverse (ALEXI; Anderson et al., 1997) surface energy balance model. While highly valuable for drought monitoring (Anderson et al., 2016; Anderson et al., 2011; Bhuiyan et al., 2006; Otkin et al., 2013; Rojas et al., 2011), the coverage and resolution of these indices inhibit consideration of physiologic differences between plant stomatal behaviors, field-scale variability in soil moisture, or ground covers in a pixel other than soil and vegetation, and are therefore unsuitable for crop stress interpretation at a finer scale. While recent work by Yang et al. (2018) has addressed some of these limitations by demonstrating the potential of using multi-sensor fusion to apply ESI at the field scale, this paper offers an alternate, potentially complementary approach for resolving thermal variability inherent in an agricultural landscape.

Here, we use Airborne Visible/Infrared Imaging Spectrometer (AVIRIS) and MODIS/ASTER Airborne Simulator (MASTER) imagery from the Hyperspectral Infrared Imager (HyspIRI) Airborne Campaign and Geographic Information Science (GIS) data of crop species to improve understanding of how medium-resolution remote sensing imagery

can provide a compromise between complexity and scalability that allows for regional assessments of crop health. We propose an approach for evaluating crop stress that controls for thermal variability within crop species, soil and NPV without the need for site-specific environmental inputs. We analyze thermal patterns in orchards in the Central Valley of California during the 2013-2015 drought as they vary by surface cover component (GV, soil, NPV), fractional cover, crop species, and time. We then model the expected unstressed temperature of each pixel, given its fractional composition and species, and compare the expected temperature to the measured temperature as a way of assessing relative stress between orchard species. The results will highlight the importance of accounting for thermal variability within surface covers when analyzing temperatures and are especially salient in light of the successfully deployed thermal ECOSTRESS instrument (Fisher et al., 2015) and the proposed Surface Biology & Geology (SBG) mission (Lee et al., 2015).

3.2. Methods

3.2.1. Study Area and Period

This work focused on a 3470 km^2 transect of the Southern Central Valley of California stretching 200 km from the Sierra Madre Mountain Range to the Sierra Nevada Mountain Range between Bakersfield and Fresno (Fig. 3.1). The study area has high agricultural production, encompassing portions of the three highest producing agricultural counties by value in the state: Kern County, Tulare County and Fresno County (CDFA, 2016). The transect is part of the Tulare Lake Hydrologic Region, which comprises the southern third of the Central Valley with about 1.2 million irrigated hectares out of its 4.4 million hectares total (CA DWR, 2009). The region has a Mediterranean climate with dry summers and moist winters with average precipitation accumulation of less than 25.4 cm a year (CA

DWR, 2009). The study area is mostly flat and low in elevation with 99.8% of the pixels used in the study lying between 40 and 162 meters in elevation and 94.9% having a slope of one degree or less.

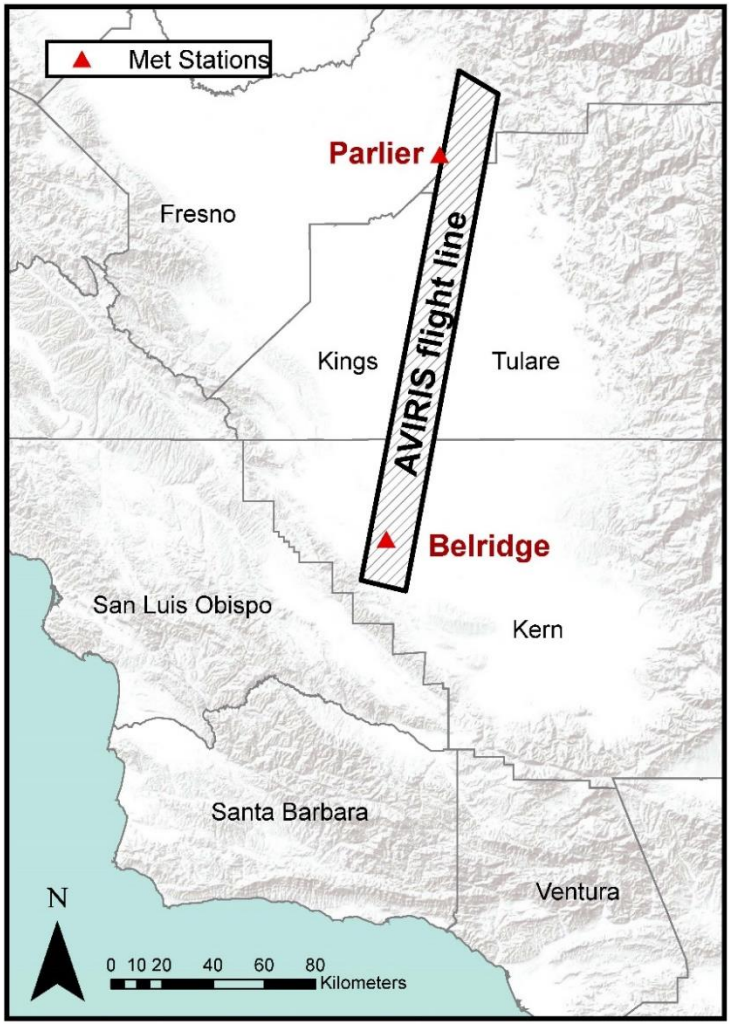

Figure 3.2: Study area located in the Central Valley of California

The study period from 2013 to 2015 coincides with an active and persistent drought in California. From 2011 through 2016, California experienced the most severe drought in 1,200 years, categorized by unusually high temperatures and low rainfall (Table 3.1), which

led to a state of drought emergency that was declared in January 2014 and lifted in April 2017 (Griffin & Anchukaitis, 2014; USGS, 2018).

While the irrigation practices of the specific fields in the study are unknown, the dry conditions and pervasiveness of irrigation use in the Central Valley suggest that most or all fields containing green vegetation are irrigated. California has the largest number of irrigated farmed hectares of any other state. An estimated 31% of the total irrigated area is orchards (Johnson & Cody, 2015), and 64% of these orchards use drip irrigation as opposed to 18% sprinkler, 17% surface and 2% subsurface. The percentage of orchards using drip irrigation has grown rapidly in the past couple decades, up from 36% in 1991. The increase in drip irrigation is attributable to its uniform distribution, schedule flexibility, protection against frost damage, improvement in fertilizer application, and ability to increase production (Tindula et al., 2013). We assume that our study area has irrigation management practices that are consistent with these statewide statistics.

Table 3.1: California climate data for rainfall, temperature, and drought during the three years of study as compared to a base period of 1901-2000 (NOAA, 2018). Data are presented with deviations from the mean in parenthesis.

Year	Annual Precipitation (cm)	Average Temperature (°C)	Maximum Temperature (°C)	Minimum Temperature (°C)	Palmer Drought Severity Index
Mean (1901-2000)	56.9	14.1	21.1	7.1	-0.15
2013	20.1 (-36.8)	15.2 (+1.1)	22.6 (+1.5)	7.8 (+0.7)	-4.22 (-4.07)
2014	50.5 (-6.4)	16.3 (+2.2)	23.4 (+2.3)	9.3 (+2.2)	-3.83 (-3.68)
2015	38.2 (-18.7)	16.0 (+1.9)	23.0 (+1.9)	8.9 (+1.8)	-3.42 (-3.27)

3.2.2. AVIRIS and MASTER Imagery

The imagery analyzed in this research was collected as part of the HyspIRI Airborne Campaign, a NASA mission that flew the AVIRIS and MASTER sensors simultaneously

throughout California between 2013 and 2017. The HyspIRI mission was recommended in the 2007 Decadal Survey as a means to enhance our ability to monitor ecosystems, natural hazards, and land use over time (Lee et al., 2015), and has since morphed into the SBG mission that was identified in the 2017 Decadal Survey as a designated program element prioritized for development (National Academies of Sciences, Engineering, and Medicine, 2018). This study used imagery collected on three dates of the HyspIRI campaign: June 6, 2013, June 3, 2014, and June 2, 2015. Early June was chosen for analysis to capture peak growth of summer Central Valley crops.

AVIRIS is an imaging spectrometer that captures 224 contiguous bands in the visible through shortwave infrared from 350 nm to 2500 nm (Green et al., 1998). MASTER (Hook et al, 2001) is a 50 band sensor with wavelengths ranging from 400 nm to 13 μm with 8 bands in the thermal (between 4-12 μm) being used to represent the proposed bands of the HyspIRI/SBG satellite. These two spatially corresponding products allow for unique observation of the link between surface processes and their corresponding thermal patterns and analysis of thermal patterns as they differ by land cover class and composition.

The AVIRIS and MASTER images were acquired on NASA's ER-2 aircraft at a height of 20 km. The imagery was pre-processed by NASA's Jet Propulsion Lab (JPL), which included orthorectified products of reflectance at a spatial resolution of 18 meters from AVIRIS (Thompson et al., 2015) and LST at a 36 meter resolution from MASTER. LST was calculated using JPL's Temperature Emissivity Separation algorithm (Hulley & Hook, 2011), with the overall accuracy of temperature retrievals reported at <= 0.33 degrees Celsius. AVIRIS imagery was aggregated to a spatial resolution of 36 meters for spatial consistency between the VSWIR and thermal data and then georectified a second time for

increased accuracy using Delaunay Triangulation (Lee & Schachter, 1980) and approximately 250 ground control points per flight line. Only the MASTER imagery that overlapped spatially with the AVIRIS imagery, which was within a 34 degree field of view, was used in the analysis. The AVIRIS and MASTER images were rotated and cropped to the study area and then the 2014 imagery received an additional co-registration of the two products using approximately 150 ground control points. The AVIRIS and MASTER imagery from 2013 and 2015 showed high spatial consistency so no additional co-registration was conducted.

The three pairs of AVIRIS/MASTER images used in this study were acquired at approximately 11:25 PDT in 2013, 14:41 PDT in 2014, and 11:59 PDT in 2015. Solar noon was at approximately 12:59 PDT at the time of the flights, so each of the flights is between one and two hours on either side of solar noon. Air temperatures from two meteorological stations, one near the southern edge of the study area and one near the northern edge, are shown in Table 3.2.

Table 3.2: Air temperature data from meteorological stations in or near the South (Belridge) and North (Parlier) ends of the study area. Temperature data were acquired from the California Irrigation Management Information System (CIMIS) at a height of 1.5 meters above the ground at the hour nearest to the flight times.

Date/Time	**Temperature in Belridge**	**Temperature in Parlier**
06/06/2013, 11:00 PDT	27.8°C	28.2°C
06/03/2014, 15:00 PDT	30.2°C	30.0°C
06/02/2015, 12:00 PDT	24.5°C	24.8°C

3.2.3. Spectral Mixture Analysis

A spectral mixture analysis (SMA) was run on each of the three AVIRIS images to obtain subpixel fractional cover of GV, NPV such as bark or dead leaves, and soil. While multi-source energy balance models traditionally characterize soil and GV, this method includes NPV as an additional important cover class that will affect the temperature and turbulent coupling of the land with the atmosphere (Kongoli et al., 2014). The SMA method employed was Multiple Endmember Spectral Mixture Analysis (MESMA; Roberts et. al, 1998). MESMA uses a linear mixture model to decompose pixels into their fractional components, and provides advantages over other SMA methodologies by allowing the number and types of endmembers to vary on a per pixel basis. In this way, MESMA is able to better account for variability within endmember classes. MESMA was chosen for this study for its ability to model the spectral properties of soils, NPV, and crops using multiple endmembers that can be used to group surface covers into thermal groups. A combined library of forty image endmembers was developed from the three images to capture the diversity of GV, NPV, and soil within the study site and across the dates. Image-selected endmembers were added manually to the spectral library until variation across time and space could be accounted for. This multiyear library was used to unmix each of the three images in order to increase consistency in fractions across the years. The forty endmember library was composed of 22 GV, 8 NPV, and 10 soil endmembers. MESMA unmixed each pixel as a mixture of GV, NPV, soil, and shade using between two and four endmembers to model each pixel. The shade fraction, used to account for differences between the brightness of the endmember and the spectrum being modeled, was restricted to between zero and 80 percent. Each endmember was restricted to between zero and 100 percent, and the residual mean squared error to a

maximum of 0.025 for each pixel. In order to obtain physically reasonable fractions, the unmixed results were then shade normalized by dividing each non-shade component, GV, NPV, and soil, by the sum total of all non-shade components in that pixel (Adams et al., 1993). The resultant products mapped soil, NPV, and GV at a subpixel level throughout the study scene with an accompanying map showing which endmembers were used to unmix which pixels.

3.2.4. Crop Map

Some spatial knowledge of what types of crops are being grown is necessary for accurate thermal estimation of each field. While this information can come from a variety of sources either derived from remote sensing data or as a separate ground data source, knowledge of the spatial distribution of crop species within this study area was obtained from county-level polygons provided by each of the four counties that intersect it: Fresno, Kern, Kings, and Tulare. These crop polygon maps were created by each county in accordance with a statewide pesticide permitting and use reporting program, which requires growers to register their field with information of crop type and the proposed pesticide application. These maps were used to match thermal data from MASTER with the corresponding crop on the ground.

For the purposes of this study, we evaluated the thermal signatures of eleven fruit and nut crops: almonds (AL), cherries (CH), grapes (GR), lemons (LE), nectarines (NE), oranges (OR), peaches (PE), pistachios (PI), plums (PL), tangerines (TA), and walnuts (WA). These crops were chosen due to their prevalence in the study area, high economic value, and long lifespan. Given these characteristics, the health of these crops is particularly important to monitor during drought for economic and cultural reasons. The number of

fields of each crop species contained in the GIS data layers for each year are listed in Table 3.3. The data layers are not comprehensive of all crop fields in the study area. Therefore, although the 2015 data layer contains roughly 500 more fields than 2013 or 2014, this increase is not necessarily representative of a larger number of perennial fields planted in the study area but is rather more indicative of the completeness of the 2015 layer.

Table 3.3: Number of fields of studied fruits and nut crops contained in each year's GIS data layer

Species	Number of fields in study area		
	2013	*2014*	*2015*
Almond	119	126	220
Cherry	42	40	39
Grape	205	189	271
Lemon	17	34	22
Nectarine	341	274	326
Orange	278	326	282
Peach	373	338	474
Pistachio	108	123	246
Plum	291	258	256
Tangerine	26	44	69
Walnut	29	31	59
Total	1829	1783	2264

3.2.5. Statistical Analyses of LST

We hypothesized that soil and NPV properties that lead to different VSWIR spectra, such as albedo, moisture, or structure, will create differences in temperature that will create distinct thermal classes that group by VSWIR endmember. Temperature distributions were evaluated by VSWIR endmember using a one-way analysis of variance (ANOVA). All pure NPV and soil pixels that had been classified using the same NPV or soil endmember, and therefore showed spectral similarity, were grouped together as a class for analysis. Post-hoc Tukey's tests were run for both NPV and soil for each date to test for significant thermal differences between classes.

To further test the hypothesis that MESMA endmembers model soil pixels into groups of similar soil moisture, we tested two hypotheses: 1) Pixels modeled with MESMA soil endmembers that have lower albedos will have lower temperatures and; 2) Pixels modeled

with MESMA soil endmembers that have lower SWIR reflectance will have lower temperatures. First, we plotted the albedo of each of the ten endmembers against the average temperature of the pure soil pixels unmixed with that endmember to assess correlation. Albedo is a measure of brightness defined as the ratio of reflected radiance from the surface to the incoming solar radiation to the surface (irradiance). As moisture lowers the albedo and cools the temperature of soils, we expected to find a positive correlation between albedo and temperature. Albedo was calculated using the same approach as in Roberts et al., (2004; 2012). Using this method, downwelling irradiance is modeled for the specific location, date and time of a dataset using MODTRAN (Berk et al., 2017), then multiplied by surface reflectance from AVIRIS and summed across all wavelengths to calculate total reflected irradiance between 350 and 2500 nm (Eq 1). This sum is divided by downwelling irradiance integrated across the same wavelength region.

$$albedo = \frac{\int_{350\text{nm}}^{2500\text{nm}} \text{Reflectance} * \text{Irradiance}}{\int_{350\text{nm}}^{2500\text{nm}} \text{Irradiance}} \quad (1)$$

Albedo was calculated using the reflectance and modeled irradiance as described in Eq 1, resulting in a unitless measure of brightness for each endmember. Second, we assessed correlation between SWIR reflectance of each of the ten endmembers and the average temperature of the pure soil pixels unmixed with that endmember. Musick and Pelletier (1986) found that moist soils have lower than expected reflectance at the longer wavelengths of the SWIR, as examined through the ratio of the Landsat TM 5 and 7 bands. We used a comparable AVIRIS ratio of the 1662 nm band to the 2028 nm band and evaluated whether the pixels modeled by endmembers with smaller ratios had lower average LST values.

For GV, we hypothesized that crop species would show multiple distinct thermal signatures that would persist through time. To test this, a one-way ANOVA and post-hoc

Tukey's tests were run to determine if significant differences exist between pure pixels of crop species. Further, to evaluate whether crops cluster by species within GV-LST space, we used the same method as Roberts et al. (2015). A Multivariate Analysis of Variance (MANOVA) was run as an initial test for clustering. After finding that significant differences existed by species, to further study one-on-one differences between pairs of crops, Bhattacharyya Distances (D_B) were computed for each crop pair in GV-LST space. D_B is a measure of the ability to separate two classes, calculated with the mean and covariance matrix of each class (Kailath, 1967). Smaller distances indicate greater similarity and larger numbers greater dissimilarity. Distances were computed for all species distribution pairs in each of the three images to better understand which species show the greatest dissimilarity in GV-LST space and to analyze whether these patterns hold over time.

3.2.6. Modeled Temperature

This paper proposes an approach for estimating expected, non-stressed LST at the pixel level using internalized calibration of temperatures with species and scene-specific thermal endmembers. By calculating an expected temperature for each pixel, we can assess whether the measured temperature from MASTER is higher or lower than the modeled expected temperature for an unstressed crop, given its species and fractional cover. Differences may indicate stress, in the case of a higher than expected measured LST, and shade effects or high crop ET in the case of a cooler than expected LST. As a pixel is made up of the sum of its fractional surface components, we assume that the temperature of a pixel can be modeled by a linear mixture of its thermal components, that is, the sum of the LST for each of those components multiplied by their fractional portion of the pixel. To capture thermal

variability within surface covers, each of the three components (GV, NPV, soil) is broken down into subclasses that are expected to share similar thermal properties, referred to as thermal classes going forward. These thermal classes resulted in each of the three surface covers having more than one thermal endmember, one for each thermal class. The endmembers that were used to model the expected temperature of each pixel were determined by the classes that were contained in that given pixel. Therefore, an expected LST for each pixel was calculated using known VSWIR pixel fractions from MESMA for GV (f_{GV}), NPV (f_{NPV}), and soil (f_{SOIL}) and the expected surface temperatures for pure pixels of GV, NPV, and soil (T_{GV}, T_{SOIL}, T_{NPV}) for each of the respective thermal classes (i,j,k) contained in that pixel, as defined in Eq.2:

$$LST_{expected} = f_{GV}T_{GVi} + f_{SOIL}T_{SOILj} + f_{NPV}T_{NPVk} \quad (2)$$

Green vegetation was separated into three agronomically important and botanically similar thermal classes: nut crops (almond, pistachio, walnut), perennial fruit crops (cherry, grape, nectarine, peach, plum) and citrus fruit crops (lemon, orange, tangerine). GV was grouped in a way that would account for inherent differences in thermal patterns while also capturing species-level stress. We originally modeled the expected temperature of GV using one common expected temperature for all crops. However, we found that citrus fruits had, on average, much higher temperatures than the other crops. This finding may be explained by the work of Gonzalez-Dugo et al. (2013) who found that citrus crops show significant stomatal closure at midday even if they are well-watered. We, therefore, hypothesized that within perennial crops there are many thermal classes that have inherently different temperatures, not associated with stress. To model all trees using the same temperature would not acknowledge these core thermal differences within vegetation. However, we

chose not to model GV using species-specific groups as this would obscure stress within species. For example, if oranges are modeled using the average temperature of pure orange pixels, and the oranges in the region are stressed, the modeled temperature will be too high and stress will be unidentifiable. Therefore, three classes of GV were chosen as a compromise with which relative stress can be identified yet inherent thermal differences are accounted for. A one-way ANOVA and Tukey's post-hoc test for each year confirmed that these three GV classes have significantly different temperature signatures ($F(2, 35206) = 1643$, $p < 0.001$, $\alpha = 0.05$) with citrus fruit showing the highest temperatures and nut crops the lowest temperatures, possibly attributable to their high irrigation demand (see results Fig 3.7).

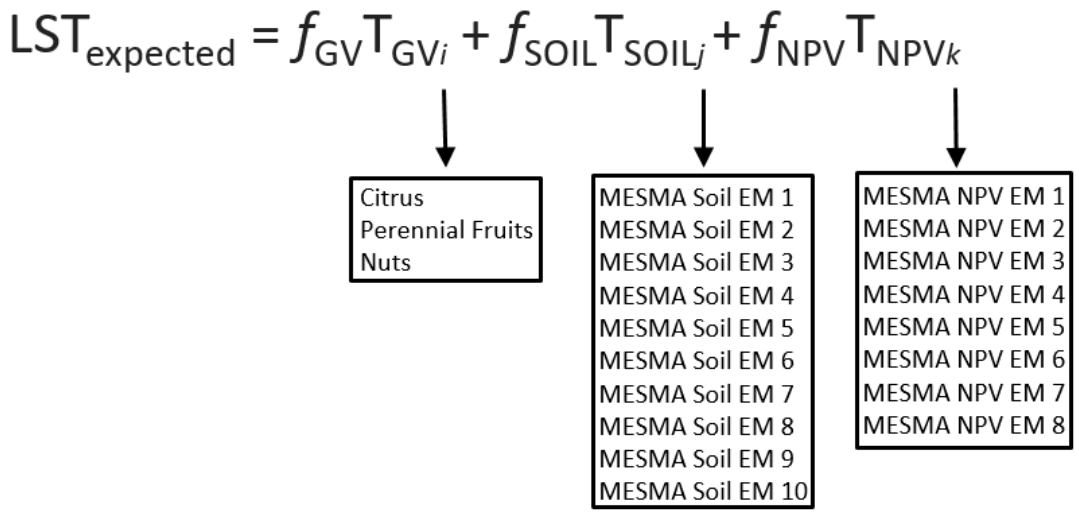

Figure 3.3: Multiple thermal classes are contained within each surface cover component, resulting in 240 different thermal endmember combinations for each modeled pixel

Soil and NPV were separated into 10 and 8 thermal classes, respectively, using the same endmembers that were used for MESMA VSWIR fraction analysis. All pixels of soil or NPV that were modeled in MESMA using the same endmember were grouped together into a thermal class and modeled using a common expected soil and/or NPV temperature. With 3 GV, 8 NPV, and 10 soil thermal endmembers, a pixel of GV, NPV, and soil could

therefore be modeled using one of 240 different combinations of temperature endmembers (Fig 3.2). Examination of the temperature distributions within each of the thermal classes showed that some of the distributions were skewed. Therefore, the average, expected temperature for each of the 21 classes was calculated using the median temperature for all pure pixels of that class within the fields analyzed in the study site. This process was conducted separately for each of the three images, resulting in 63 endmember temperatures over the three dates. The number of pure pixels per class varied widely depending on the prevalence of that model in the scene, and ranged from 15 pixels (Soil endmember #1 in 2013) to 43,377 pixels (Soil endmember #10 in 2015). Thermal endmembers were scene-specific to account for temporal variation in environmental variables such as air temperature, humidity and wind, and the timing of the flight that will affect the LST. This approach does not require meteorological parameters or crop-specific inputs.

3.2.7. Land Surface Temperature Residuals

For each year and each pixel, an LST residual was calculated as the difference between the modeled LST values and the LST values from the MASTER imagery (Eq 3).

$$\text{Residual} = LST_{MASTER} - LST_{expected} \quad (3)$$

LST residuals are proposed as a way of normalizing LST to account for known differences in pixel composition to make thermal signatures comparable across space. LST residuals are independent of fractional cover and soil, NPV, and crop-inherent thermal differences, stripping away features that are known to influence temperatures, and allowing for relative comparisons of stress between pixels, fields, or species. Pixels with positive residuals will have a higher measured temperature than expected, given the fractional cover, surface cover components, and thermal classes in the pixels, which are assumed indicative of higher-

stressed vegetation. Pixels with negative residuals are measured as cooler than expected, possibly due to illumination effects, high ET, or shadowing (Dubayah & Rich, 1995). Summary statistics were computed for each species to analyze species-level stress.

3.2.8. Crop LST by Yield and ET

To further evaluate crop-specific patterns of LST, we tested two hypotheses: 1) Crops with higher LST residuals, on average, will show declining yields over the study period, as would be indicative of stress; and 2) Crops with higher ET rates will shed more energy through latent heat flux and therefore have lower average LST values than crops with lower ET rates. To test the first hypothesis, yield data were obtained at the county level from the four counties that were part of the study area using annual agricultural statistics reports (Fresno County Agricultural Commissioner, 2018; Kern County Department of Agriculture and Measurement Standards, 2018; Kings County Department of Agriculture and Measurement Standards, 2018; Tulare County Agricultural Commissioner/Sealer, 2018). Productivity was reported in amount per area with most crops reporting tons per acre. The overall productivity for each crop type was calculated using an average of the county statistics, weighed by the relative area of that crop in each county. Because yield data are not available at the field-scale, county-level statistics were the closest proxy of productivity in the study area that could be obtained. Therefore, while the yield data and crop LST residuals are not directly relatable since the residuals only refer to a spatial subset of what is reported by the yield data, the yield data is expected to give a general sense of which crops were faring well and which were most stressed within the study area. To test the second hypothesis, we evaluated the correlation between average crop LST and the daily ET rate of each crop. ET rates were calculated as the product of the daily reference ET, as reported by

the Belridge CIMIS station for each of the three dates, and the crop coefficient for each of the studied species, as calculated for June in the Southern San Joaquin Valley of California in a dry year (Irrigation Training & Research Center, 2003).

3.3. Presentation and Interpretation of Results

3.3.1. LST by Date

LST distributions in the study area for the three study dates showed median pixel temperatures in 2013 and 2015 of 320.5K and a median pixel temperature in 2014 of 322.7K (Fig 3.3). The 2013 and 2015 distributions were slightly negatively skewed while the 2014 data were moderately negatively skewed. The two distributions from 2013 and 2015 showed the greatest similarity in distributions, likely due to their proximity of flight time. The 2014 flight captured the warmest distribution of temperatures, on average, hypothesized to be associated with the later flight time in 2014.

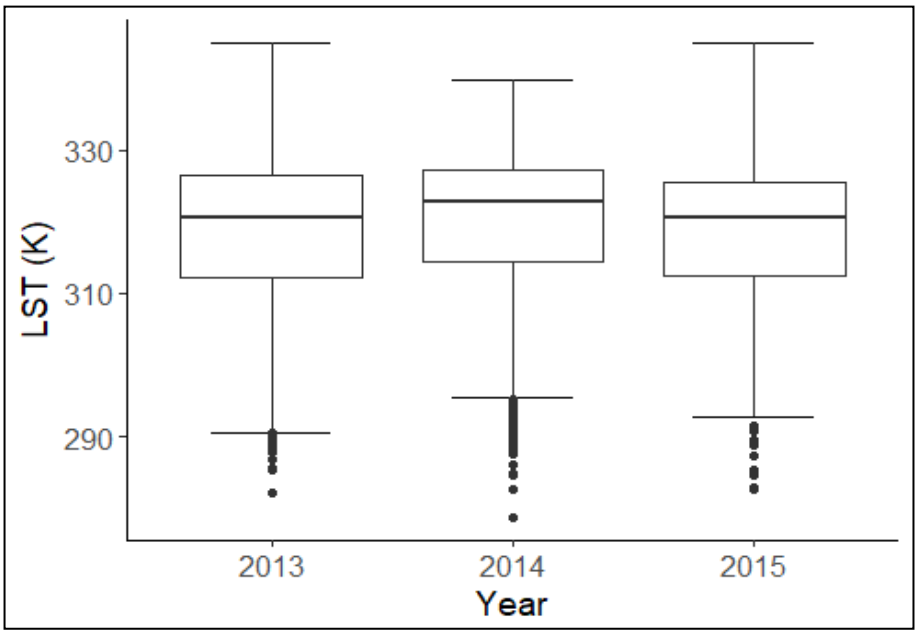

Figure 3.3: Distributions of Land Surface Temperatures in the study area for the three image dates. The centerline shows the median while the top and bottom lines of the box represent the third and first quartiles. The upper whisker is located at the smaller of the maximum LST value and the third quartile + 1.5 times the interquartile range. The lower whisker is located at the larger of the minimum LST value and first quartile - 1.5 times the interquartile range.

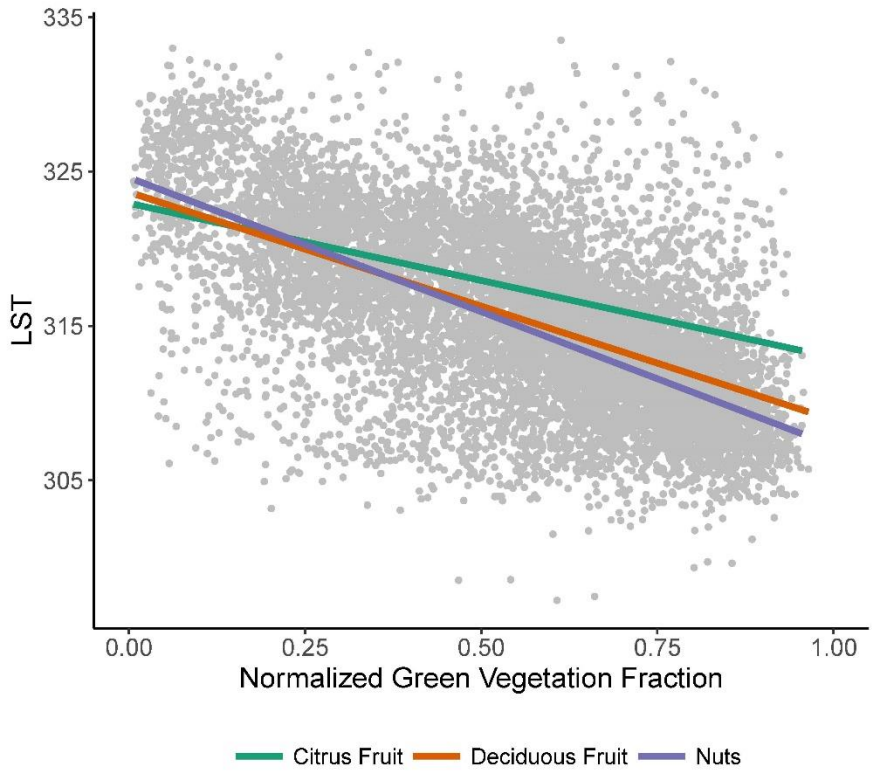

Figure 3.4: The inverse linear relationship between GV and LST is shown through 10,000 randomly selected pixels from 2013. The linear regressions for citrus (LST = -11.5*GV + 322, r^2=0.38, n=1682, p<0.001), deciduous fruits (LST = -16.4*GV + 322, r^2=0.43, n=3236, p<0.001), and nuts (LST = -18.0*GV + 324, r^2=0.47, n=5082, p<0.001) are shown.

3.3.2. GV Fractions and Temperature

To evaluate the relationship between GV fraction and LST, 10,000 random pixels with GV fraction between 0 and 1 were plotted against each other. GV and LST were observed to be inversely correlated (Fig 3.4). The more green vegetation that a pixel contained, the lower its expected temperature. This relationship held true for all three dates. However, there was considerable spread around the GV/LST line, suggesting that there are other sources of thermal variability within GV fractional classes that should be accounted for when estimating stress. An inset of the southern study area shows the fractional cover and its corresponding temperature profile for 2013, 2014, and 2015 (Fig 3.5). The fields with

high GV are contrasted against bare soil fields and areas with high NPV cover. The areas with high GV fraction showed the lowest temperatures while the bare soil showed temperatures that were 25-40°C higher than those of pure GV. The two vertically-oriented lines in the image are aqueducts that were cooler than the soils surrounding them but warmer than the vegetated fields. The large fields of NPV in the northeast corner of the image are registered as pomegranate trees, and we hypothesize that the high NPV fraction is due to the trees not being completely leafed out, newly planted, or unirrigated. NPV occurring within green fields may be attributable to dead grass between rows, brown leaves, or branches.

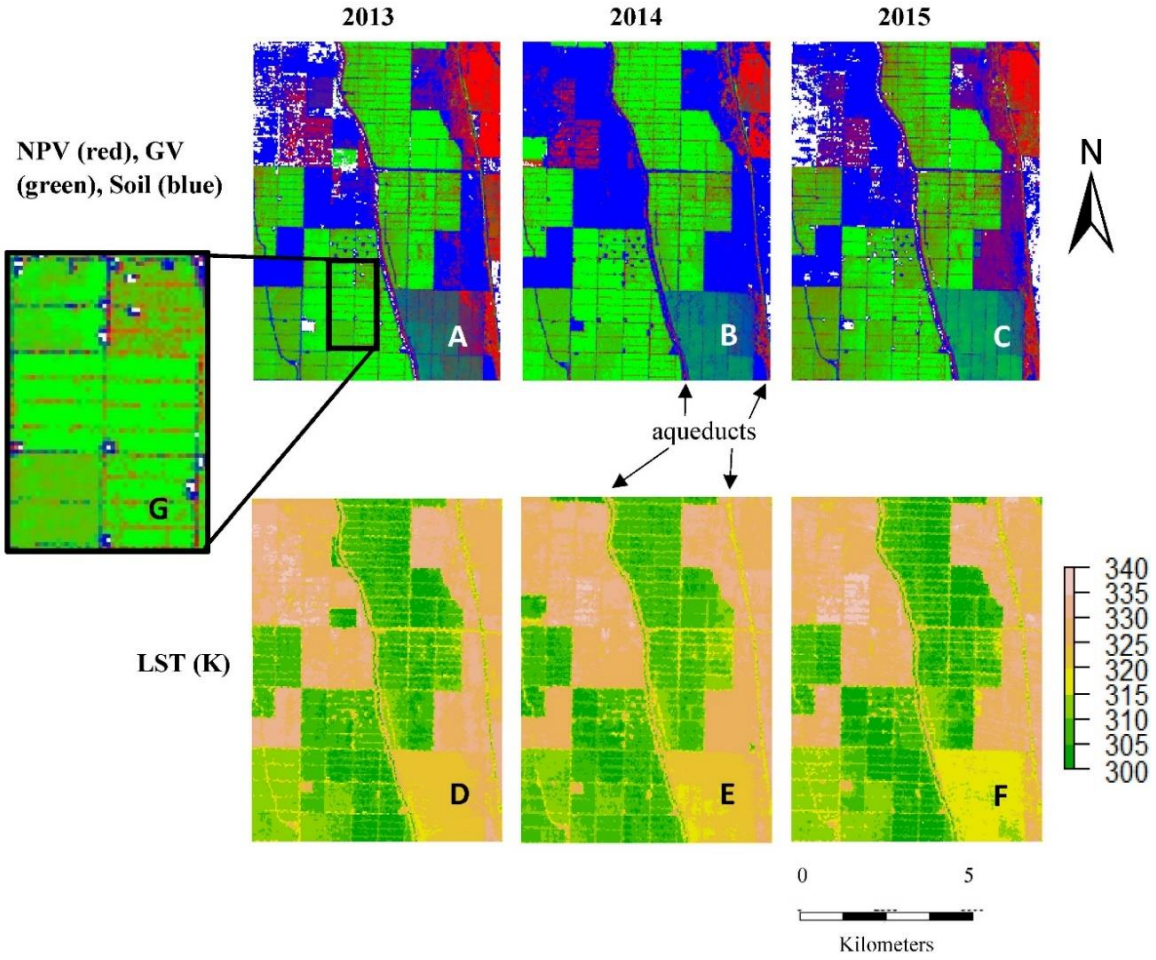

Figure 3.5: MESMA results (A, B, C) and LST (D, E, F) of a south inset of the study area (35°32'45.90"N, 119°39'56.21"W) for each of the three dates. G shows a zoomed in view of almond and pistachio fields in order to illustrate how NPV is occurring within growing fields. White areas of A, B, and C are pixels that were not modeled as any of the three cover classes by MESMA.

3.3.3. *VSWIR Endmembers and Temperature*

All pixels of soil and NPV that were classified by MESMA with the same VSWIR endmember were analyzed and modeled as a thermal class. Of the eight NPV endmember classes, seven showed significantly different temperature distributions in 2013, five in 2014, and six in 2015, as analyzed by a one-way ANOVA with Tukey's Post-Hoc (2013: $F(7, 13597) = 4023$, $p < 0.001$, $\alpha = 0.05$, 2014: $F(7, 11344) = 893.4$, $p < 0.001$, $\alpha = 0.05$, 2015: $F(7, 19914) = 2828$, $p < 0.001$). Of the ten soil endmembers, five of the endmembers

showed significant differences in temperature in 2013 and 2015 and seven showed significant differences in 2014 (2013: $F(8, 41892) = 1564.0$, $p < 0.001$, $\alpha = 0.05$, 2014: $F(9, 46828) = 491.0$, $p < 0.001$, $\alpha = 0.05$, 2015: $F(9, 62036) = 652.3$, $p < 0.001$). We hypothesize that the structure of the NPV and the moisture content of the soil were the dominant common features that made the endmembers separable in both the VSWIR and thermal.

As a further examination of the potential influence of soil moisture on VSWIR and thermal spectra, we found that darker soil endmembers were used to model pixels that, on average, had lower temperatures than pixels that were modeled with brighter soil endmembers, suggesting cooling by evaporation from moist surfaces (Fig 3.6). The relationship was shown to be significant in 2013 and 2015 (2013: $r^2=0.40$, $n=10$, $p<0.05$; 2015: $r^2=0.52$, $n=10$, $p<0.05$). The non-significance of the 2014 relationship was attributable to the high mean LST of soil EM 1. If soil EM 1 were not included in the regression, the 2014 relationship would be significant with an r^2 of 0.67. After examining the pixels that were modeled in 2014 by soil EM 1, we are unable to conclude why these pixels are warmer than expected but we hypothesize that the albedo of the soil is being lowered by some sort of management practice other than irrigation, such as a row cover or fertilizer. Although a positive relationship was found for soil albedo and LST in two of the years, a plot of albedo and average LST for the NPV endmembers showed no relationship (2013: $n=8$, $r^2=0.09$, $p>0.05$; 2014: $n=8$, $r^2=0.02$, $p>0.05$; 2015: $n=8$, $r^2=0.03$, $p>0.05$) . This finding supports the assumption that MESMA soil endmembers are sensitive to soil moisture. This finding is also consistent with analyses of soil endmember SWIR reflectance and modeled pixel temperatures. The wavelength ratio and average temperature showed a negative linear relationship, as hypothesized, and this relationship was significant in 2013

(r^2=0.49, n=10, p<0.05) and 2014 (r^2=0.67, n=10, p<0.05), but not in 2015. Both of these analyses suggest that soil groups formed by VSWIR unmixing can capture ranges of moisture and are suitable for use as thermal classes.

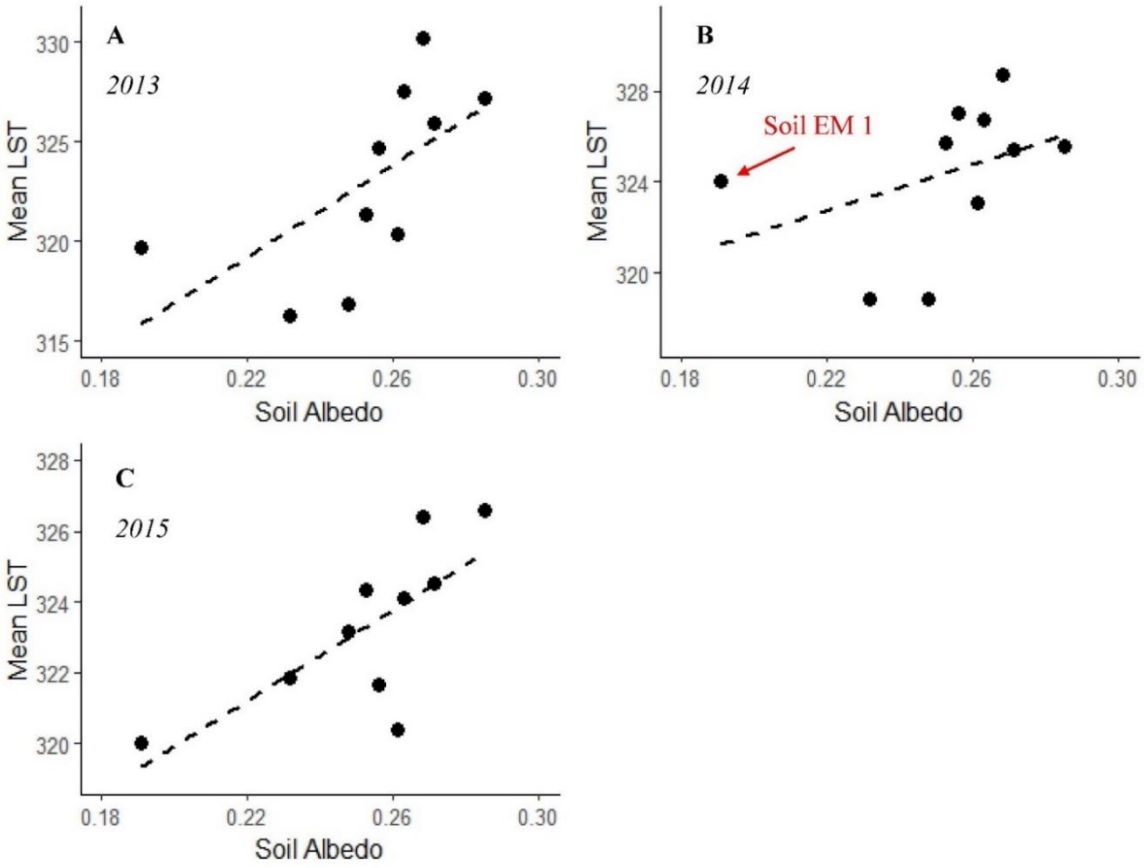

Figure 3.6: Endmember albedo plotted against mean LST of the pure soil pixels modeled by that endmember. Plots are separated by year. For each plot, the ten points represent the 10 MESMA soil classes. Dashed lines denote the linear regressions for 2013 (LST = 116*Albedo + 294, r^2=0.40, n=10, p<0.05), 2014 (LST = 51*Albedo + 311, r^2=0.16, n=10, p>0.05), and 2015 (LST = 64*Albedo + 307, r^2=0.52, n=10, p<0.05).

3.3.4. Crop Species by GV Fraction and Temperature

Perennial crop species were analyzed by GV fraction and temperature to understand whether species in agricultural orchards cluster in GV-LST space. As well as showing significant LST differences between thermal groups (Fig. 7), results from a MANOVA

indicated that significant differences exist at the species level within GV-LST space in each year (2013: $F(10, 162682) = 2883$, $p < 0.001$, $\alpha = 0.05$, 2014: $F(10, 168766) = 2140$, $p < 0.001$, $\alpha = 0.05$, 2015: $F(10, 222474) = 2498$, $p < 0.001$). Computing D_B allowed for further analysis of dissimilarity between pairs of species (Tables 4 to 6). Results showed that general patterns of D_B held temporally as pairs with high or low relative dissimilarity tended to stay the same for 2013, 2014, and 2015. For each of the three image dates, almonds showed the greatest overall dissimilarity and highest separability from other crop species, shown by the higher D_B. Over all three dates, almond-pistachio and almond-tangerine showed two of the top five largest D_B, indicating high dissimilarities. Peach-plum, orange-lemon, and peach-nectarine all consistently appeared as three of the top five smallest D_B, indicating relative similarity. Results from 2013 had the highest D_B of any of the years (between oranges and almonds; d=0.342) while 2015 did not have any distances greater than 0.20.

When evaluating temperature patterns of pure pixels of crop species, independent of GV fraction, ANOVA results for each year showed that one or more crop species had significantly different temperature distributions (2013: $F(10, 33135) = 735$, $p < 0.001$, $\alpha = 0.05$, 2014: $F(10, 35198) = 413$, $p < 0.001$, $\alpha = 0.05$, 2015: $F(10, 28749) = 369$, $p < 0.001$). A post-hoc Tukey's test showed that of the 11 crops, six distinct thermal patterns were found in 2013 and 2015, and seven in 2014. The two pairs of crops that showed indistinct thermal signatures from each other over all three dates were orange-tangerine and cherry-tangerine.

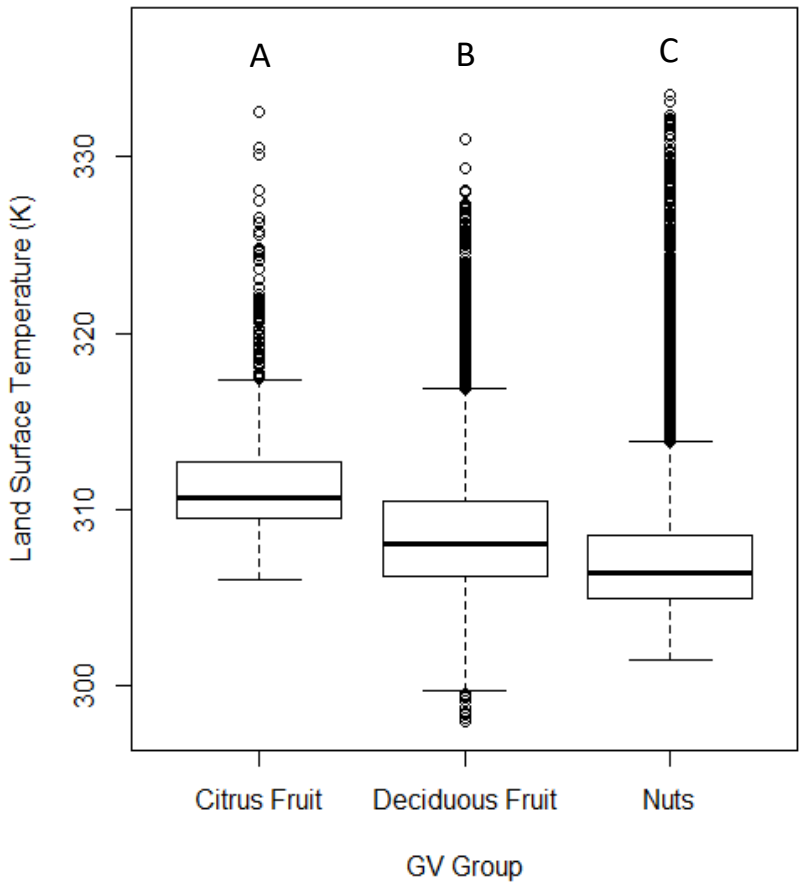

Figure 3.7: Temperature distributions for all pure GV pixels of citrus fruit, deciduous fruit, and nuts. The boxplots visualize the results of a Tukey's post-hoc test run after a one-way ANOVA with data from 2014. Different letters above each boxplot signify that the class was significantly different from the others. Boxplot lines defined as in Figure 3.3.

Table 3.4: D_B calculated for species pairs in GV-LST space in 2013. Larger distances (greater dissimilarity) are shown in darker colors. Color categories are white (D_B <0.05), light blue (0.05≤ D_B <0.1), medium blue (0.1≤ D_B <0.2) and dark blue (D_B >0.2).

	AL	CH	GR	LE	NE	OR	PE	PI	PL	TA	WA
AL		0.152	0.152	0.295	0.057	0.342	0.089	0.284	0.125	0.295	0.039
CH	-		0.041	0.030	0.043	0.045	0.043	0.079	0.013	0.051	0.136
GR	-	-		0.070	0.035	0.054	0.032	0.035	0.017	0.033	0.120
LE	-	-	-		0.107	0.017	0.099	0.089	0.050	0.034	0.224
NE	-	-	-	-		0.129	0.005	0.130	0.017	0.087	0.031
OR	-	-	-	-	-		0.113	0.043	0.058	0.023	0.279
PE	-	-	-	-	-	-		0.125	0.015	0.069	0.045
PI	-	-	-	-	-	-	-		0.078	0.066	0.278
PL	-	-	-	-	-	-	-	-		0.034	0.092
TA	-	-	-	-	-	-	-	-	-		0.203
WA	-	-	-	-	-	-	-	-	-	-	

Table 3.5: Same as Table 3.4 but for 2014.

	AL	CH	GR	LE	NE	OR	PE	PI	PL	TA	WA
AL		0.214	0.143	0.286	0.028	0.275	0.056	0.337	0.099	0.288	0.133
CH	-		0.023	0.032	0.087	0.010	0.062	0.065	0.044	0.038	0.079
GR	-	-		0.048	0.056	0.034	0.034	0.059	0.028	0.052	0.058
LE	-	-	-		0.136	0.011	0.081	0.120	0.051	0.007	0.073
NE	-	-	-			0.122	0.009	0.202	0.025	0.141	0.076
OR	-	-	-				0.081	0.080	0.050	0.015	0.096
PE	-	-	-					0.168	0.007	0.084	0.043
PI	-	-	-						0.151	0.112	0.163
PL	-	-	-							0.053	0.058
TA	-	-	-								0.084
WA	-	-	-	-	-	-	-	-	-	-	

Table 3.6: Same as Table 3.4 but for 2015.

	AL	CH	GR	LE	NE	OR	PE	PI	PL	TA	WA
AL		0.171	0.095	0.146	0.024	0.145	0.048	0.184	0.066	0.185	0.029
CH	-		0.026	0.043	0.088	0.027	0.057	0.014	0.056	0.064	0.198
GR	-	-		0.068	0.035	0.045	0.028	0.020	0.040	0.086	0.132
LE	-	-	-		0.075	0.016	0.038	0.076	0.026	0.036	0.185
NE	-	-	-	-		0.077	0.014	0.101	0.029	0.122	0.077
OR	-	-	-	-	-		0.028	0.036	0.017	0.010	0.159
PE	-	-	-	-	-	-		0.063	0.003	0.051	0.081
PI	-	-	-	-	-	-	-		0.064	0.063	0.195
PL	-	-	-	-	-	-	-	-		0.032	0.090
TA	-	-	-	-	-	-	-	-	-		0.177
WA	-	-	-	-	-	-	-	-	-	-	

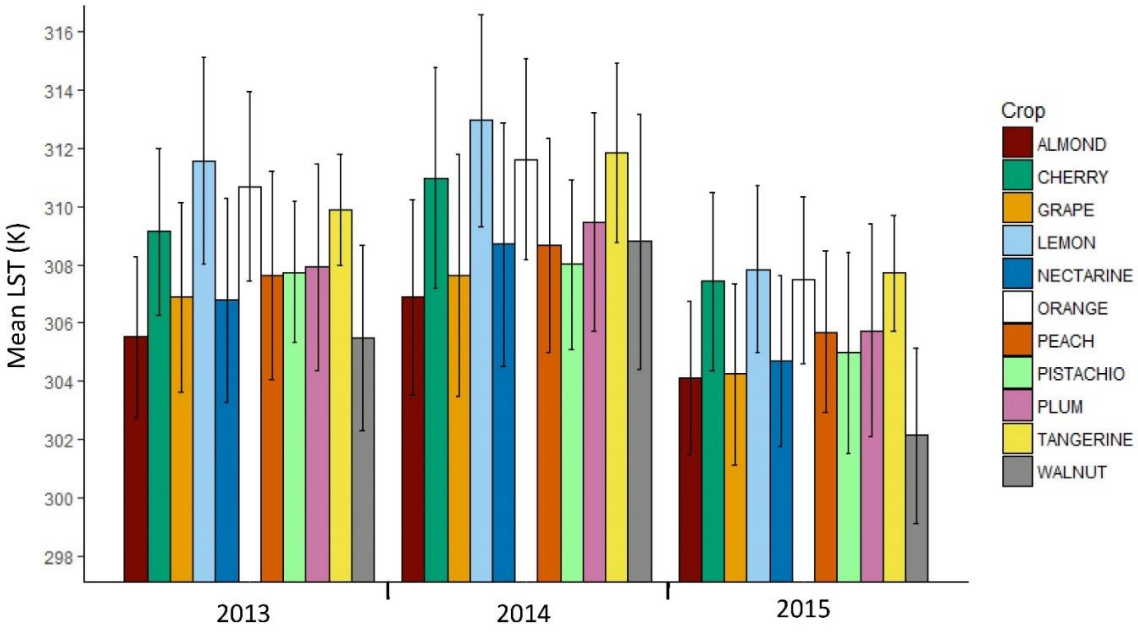

Figure 3.8: Bar plot shows the mean temperature and standard deviation for pure pixels of each crop for each of the image dates.

An evaluation of mean crop temperatures of pure pixels of each species by year showed that the temperature of each species relative to one another did not deviate greatly from year to year (Fig 3.8). The almonds had one of the top two coolest mean temperatures in each of the three years. The three citrus species, orange, lemons and tangerines, consistently had the three highest temperatures in each year. Cherries always had the highest average

temperature of any crop except citrus. Every crop showed its highest mean temperature in 2014, likely attributable to the later flight time. The consistency suggests that thermal patterns are indicative of core biophysical properties, physiological properties, or irrigation practices that stay constant and allow for detailed analysis between species across time.

3.3.5. Temperature Residual

Crops with higher residuals showed warmer measured temperatures than would be expected while crops with low residuals showed cooler temperatures than expected. High residuals are assumed indicative of stress. On average, crop residuals increased from 2013 to 2015 with average residuals of 0.14, 0.97, and 1.1 °C respectively. This positive year-to-year trend of residuals indicates an increase in relative stress from the 2013 scene to the 2015 scene. This trend may be indicative of larger environmental and political consequences of the progressing drought with increased stress due to reduced irrigation and increased water restrictions. Alternately, the increase in relative stress could be resultant from more local scene and date-specific factors such as irrigation timing, differences in radiation load, or vapor pressure deficit.

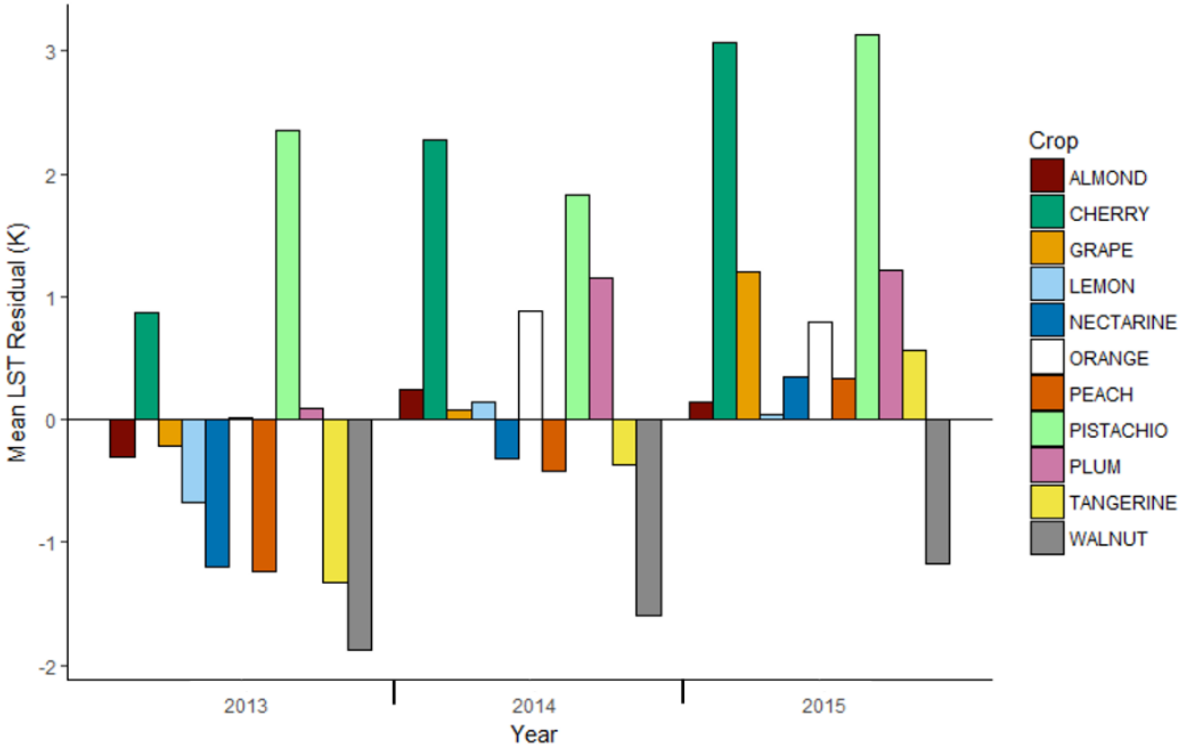

Figure 3.9: Average crop residuals calculated using every pixel of each crop (GV>0) in each year shows increasing residuals over the period of study and highlights differences in crop stress.

Yearly average residuals ranged from -1.9 °C (walnuts in 2013) to 3.1 °C (pistachios in 2015; Fig 3.9). Every crop except pistachios had its lowest average residual in 2013 (Fig 3.9). Almonds, lemons, and oranges had their highest residuals in 2014 while the other eight crops had highest residuals in 2015. Between-crop comparisons show that cherries and pistachios had the highest temperature residuals in each year. One-way ANOVAs confirm that there were significant differences of residual distributions among species in each year (2013: $F(10, 162682) = 1861$, $p < 0.001$, $\alpha = 0.05$, 2014: $F(10, 168766) = 1162$, $p < 0.001$, $\alpha = 0.05$, 2015: $F(10, 222474) = 2876$, $p < 0.001$). A post-hoc Tukey's test shows that of the 11 species, seven unique residual distributions were identified in 2013 and 2015

while six unique distributions were present in 2014. Figure 3.10 shows the distributions from 2015, as an example year.

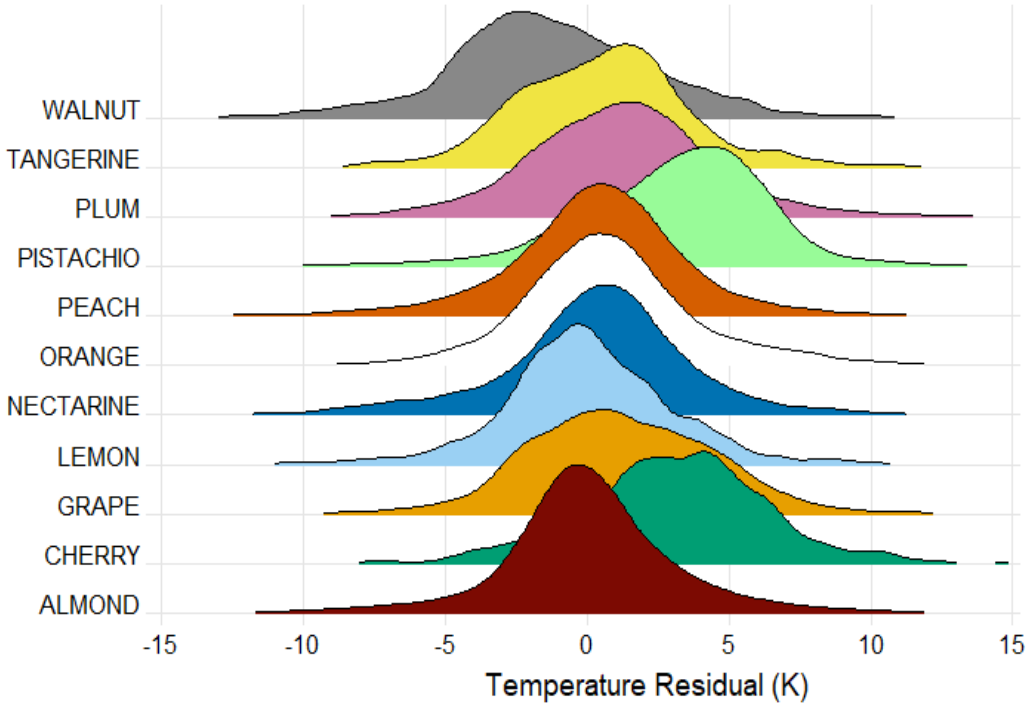

Figure 3.10: LST residual distributions from 2015

3.3.6. LST Patterns with Yields and ET Rates

Fig 3.11 illustrates that the species-level trends in crop productivity from 2013-2015, as measured by yield per unit area, were captured well by the LST residual data. The percentage change in yield per unit area from 2013 to 2015 was compared with the average residual for each crop over all three years. We expected crops with higher LST residuals to have greater declines in yields, as would be the result of stressed vegetation. Cherries and pistachios both showed the highest residuals and the largest declines in yields, a result that supported our hypothesis that high temperature residuals indicate unhealthy crops. Crops with the lowest residuals were hypothesized to be the least-stressed and therefore expected to have a relatively stable yield or an increase in yield. The crops with the lowest residuals

did not have the largest increases in yield, however there was general agreement between the two trends overall with an inverse relationship apparent. While between-crop residual and yield data from 2013-2015 showed agreement, within-crop changes in residuals from year to year did not correlate with within-crop changes in yields. For example, both the average residual and the average yield of pistachio trees declined from 2013 to 2014, changes in stress that are opposite in implication. This suggests that this method is more suitable for comparing relative stress between crops (i.e., pistachios vs almonds) than comparing stress of one crop over time (i.e., pistachios in 2013 vs pistachios in 2014).

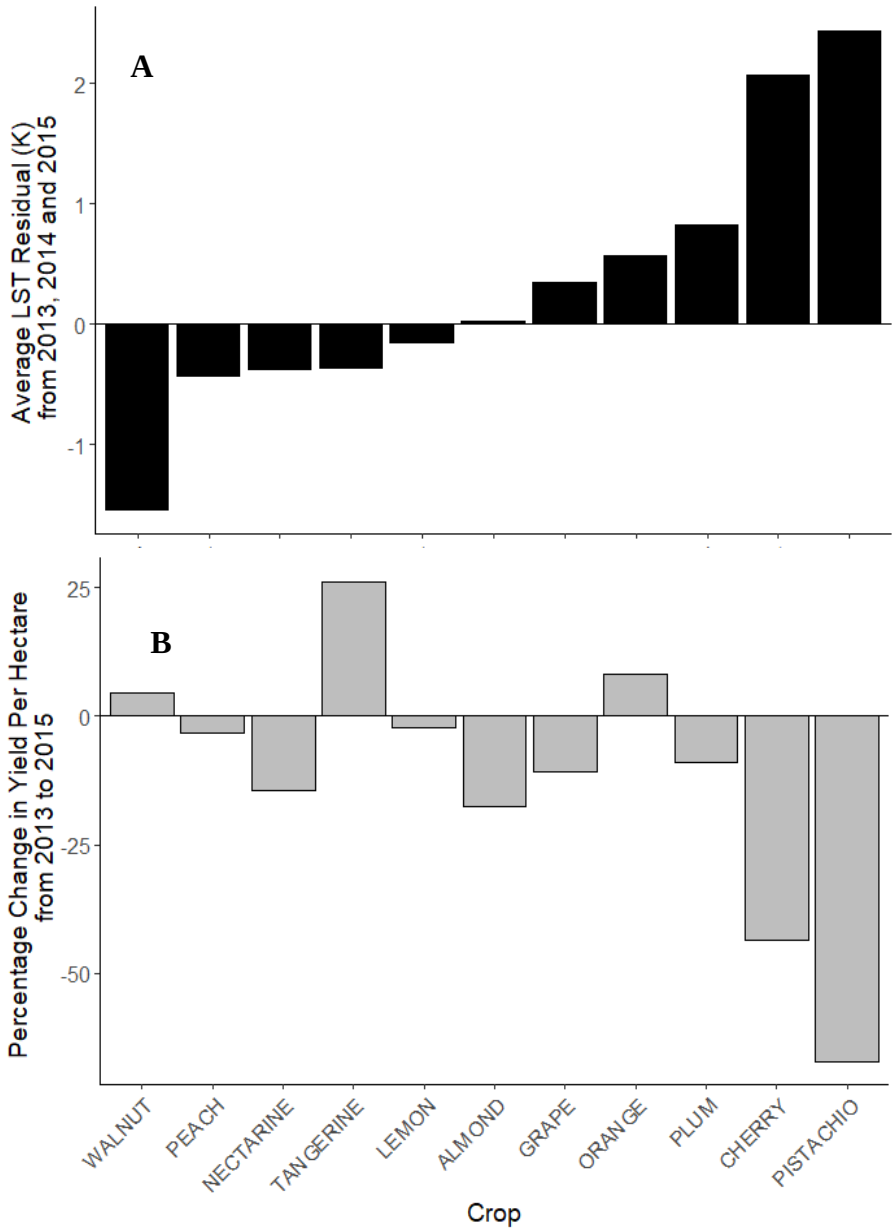

Figure 3.11: Bar plot of average temperature residual within the study area (A) and bar plot of county-level yield per hectare data for each of the studied crops calculated as (yield in 2015 – yield in 2013) / yield in 2013 * 100 (B). Crops are listed in the same order on the x-axis for both plots. The average LST residual is used as an indicator of the chronic effect of the drought plotted against its cumulative total effect on yield.

Furthermore, in Figure 3.12 average LST of each crop is plotted against its expected ET rate. We found a negative linear relationship between average LST and ET for all three years, with the relationship being significant in 2013 and 2015. This result is in line with

the hypothesis that crops with higher ET rates will be cooler. As crops are usually watered in the morning and air temperatures are cooler in the morning than afternoon, plants are more likely to show stress in the afternoon if they have insufficient water. We hypothesize that the relationship between ET and LST breaks down in the 2014 flight because of its afternoon timing, which would cause stressed plants to deviate from their expected ET rates.

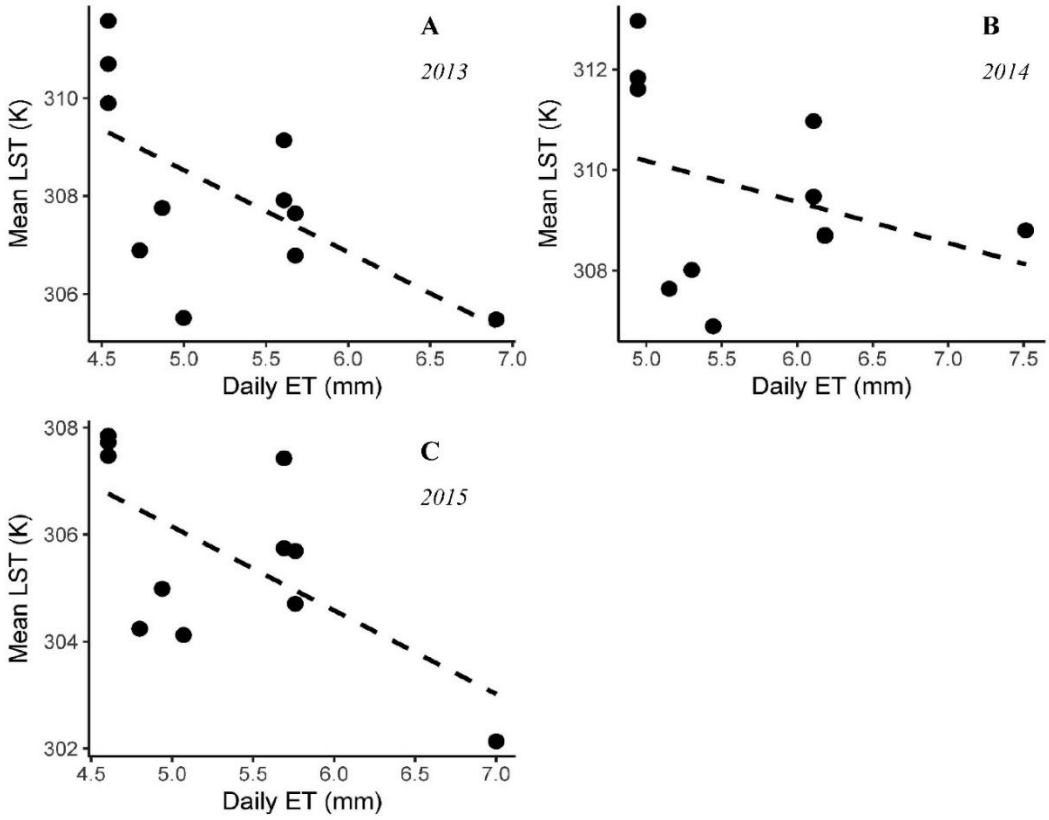

Figure 3.12: Expected daily ET rate plotted against average LST for each of the 11 crops studied. Plots are separated by year. Dashed lines denote the linear regressions for 2013 (LST = -1.67*ET + 317, r^2=0.37, n=11, p<0.05), 2014 (LST = -0.82*ET + 314, r^2=0.11, n=11, p>0.05), and 2015 (LST = -1.56*ET+ 314, r^2=0.40, n=11, p<0.05).

3.4. Discussion

In this study, we quantified thermal variability in Central Valley orchards and modeled expected temperatures using VSWIR-derived fractional cover and spatially-corresponding LST imagery. This allowed us to assess thermal variability between the expected and measured temperature of crops as a function of crop health. The findings showed that the combination of thermal and VSWIR imagery allows unique thermal groups within soil, GV, and NPV to be captured, expected LST to be calculated without environmental inputs, and relative temperatures to be compared. Here, the advantages and disadvantages of this approach will be discussed.

3.4.1 Challenges of modeling LST and interpreting LST residuals

We calculated an expected LST for each pixel as a function of its fractional cover of soil, NPV, and GV and the expected temperature for the thermal classes contained within it. Although deviations from this relationship were presumed to indicate relative levels of plant stress, there may have been other factors that contributed to the deviations from the expected GV/LST pattern. For full interpretation of the residual results, the effect of various factors on the modeled, expected LST will be discussed: a) nonlinearity of GV fraction estimation, b) shade effects, c) plant stress, d) error in fractional cover estimates, e) timing of flights, f) spatial variability in environmental variables and g) choice of thermal groups.

First, expected LST is estimated using pixel fractions derived from MESMA, a linear spectral mixture model. However, in actuality spectral mixing is nonlinear due to multiple scattering of photons (Borel & Gerstl, 1994; Roberts, 1991; Roberts et al., 1993). This effect is expected to be prominent in agricultural orchards due to the vertical structure of the canopy, density of trees, and transmittance of radiation through the leaves (Somers, et

al. 2009). As shown in Somers et al., (2009), tree-soil mixtures within a citrus orchard canopy as modeled by a linear mixture analysis will lead to an underestimation of GV for < 50% GV cover and an overestimation of green vegetation when GV cover is >50%. These errors will likely be smaller with dark soils than bright soils because there are fewer photons reflected by darker objects (Roberts, 1991). Nonlinearity can result in RMSE values of between 4 and 10% in citrus orchards for cover fractions (Somers, et al. 2009). This error in GV fraction will lead the LST model to overestimate temperatures when pixels contain less than 50% GV and underestimate temperatures when the GV fraction exceeds 50% (Fig 3.13A). Subsequently, pixels with low GV fraction will overestimate temperature, reducing the residual, while pixels with a high GV fraction will underestimate temperature, increasing the negative residual. However, the errors due to multiple scattering in this study are expected to be low because canopy endmembers were used in the linear unmixing and these endmember already capture multiple scattering.

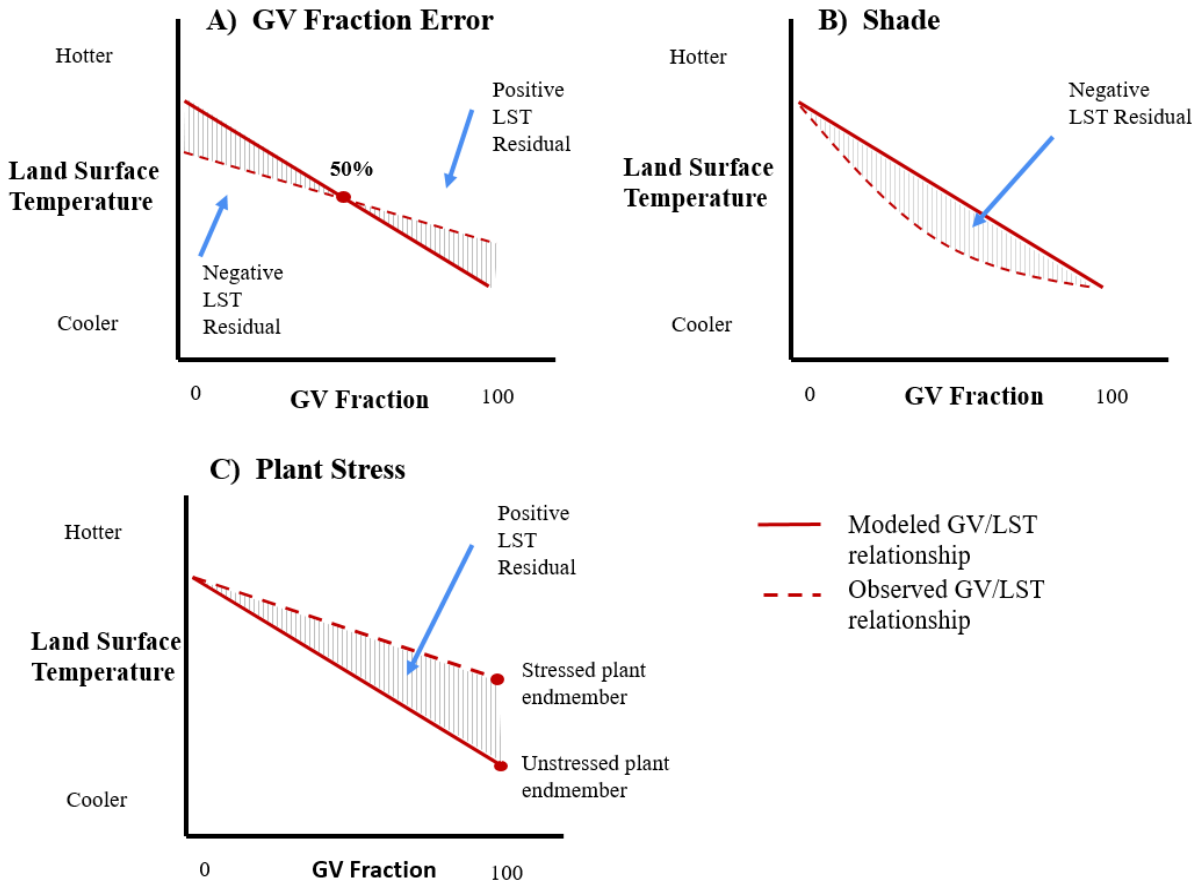

Figure 3.13: Conceptual schematics of the effect of A) GV fraction error, B) shade, and C) stress on LST residuals by GV fraction

Second, just as the linear spectral mixture does not account for photon interactions when estimating fractional cover, the linear thermal model used to model LST is also subject to nonlinear effects. Shade will cause error in soil temperature estimation that can lead to an overestimation of soil temperatures in mixed pixels. Thermal soil endmembers for the model were calculated based on the average temperature for pure soil pixels. A pure soil pixel is unlikely to be influenced by shadows, and its temperature will be a function of full solar radiation. However, as vegetation cover increases in a pixel, a larger percentage of the present soil will be shaded, up until the vegetation fraction reaches 100% and the effect cancels out (Fig 3.13B). Shaded soil would be expected to be cooler than non-shaded soil,

therefore the soil endmembers that are being used to model the soil temperature will be warmer than the actual shaded soil in mixed pixels. This will lead the temperatures of mixed pixels to be modeled as too warm, and the corresponding residuals to be too low.

Similarly, vegetation is subject to shading effects as well as differences in structure and orientation that influence LST. Jones et al. (2009) found that leaf temperatures vary by as much as 15°C between full sun and deep shade. Therefore, factors such as the orientation of the leaves, canopy structure, and row spacing are all important controls on plant temperatures as they influence the amount of vegetation in a field that is shaded. These factors also affect the surface aerodynamic roughness, which governs how readily vegetation can transfer heat and moisture to the atmosphere. The height and structure of a crop canopy determines its aerodynamic roughness, with rougher vegetation being more tightly coupled to the atmospheric moisture deficit, which increases plant ET and decreases canopy temperature (Bonan, 2008). In an aerodynamically rougher crop canopy, heat is also more readily transferred to the atmosphere by sensible heat flux. For these reasons, the remotely sensed surface temperature depends not only on the fractional cover of a pixel, but also on the composition of vegetation within a pixel. Two pixels with the same fractional cover of vegetation can have different thermal behaviors due to differences in the distribution of that vegetation, its height, and structure (Kerr et al., 2004). The model aims to account for these influences by using canopy-level image endmembers and creating multiple thermal classes for different groups of perennial crops, so the overall error attributable to canopy shading is assumed to be small.

Third, plant stress will alter the GV/LST relationship in a way that, while not introducing error, will lead LST residuals to vary by GV fraction. If a plant is stressed, its

actual temperature will be warmer than expected, leading to a positive residual. While the model is designed for such a result, the side effect is that pixels with larger fractions of stressed vegetation will have higher residuals than pixels that have small fractions of stressed vegetation, as indicated by the increasing LST residuals with GV fractions in Fig 3.13C. Therefore, if plants are stressed, we expect that GV fraction and LST residual will have a positive correlation. We examined the relationship between LST residual and GV fraction for each of the studied crops in Figure 3.13 and found a trend of increasing residuals with increasing fractional cover, a result that we believe is indicative of crop stress. The relationship between residuals and GV fraction is shown by the positive linear trend lines in Figure 3.14 and the growing shaded area with fractional cover between the modeled and observed lines in Figure 3.13C.

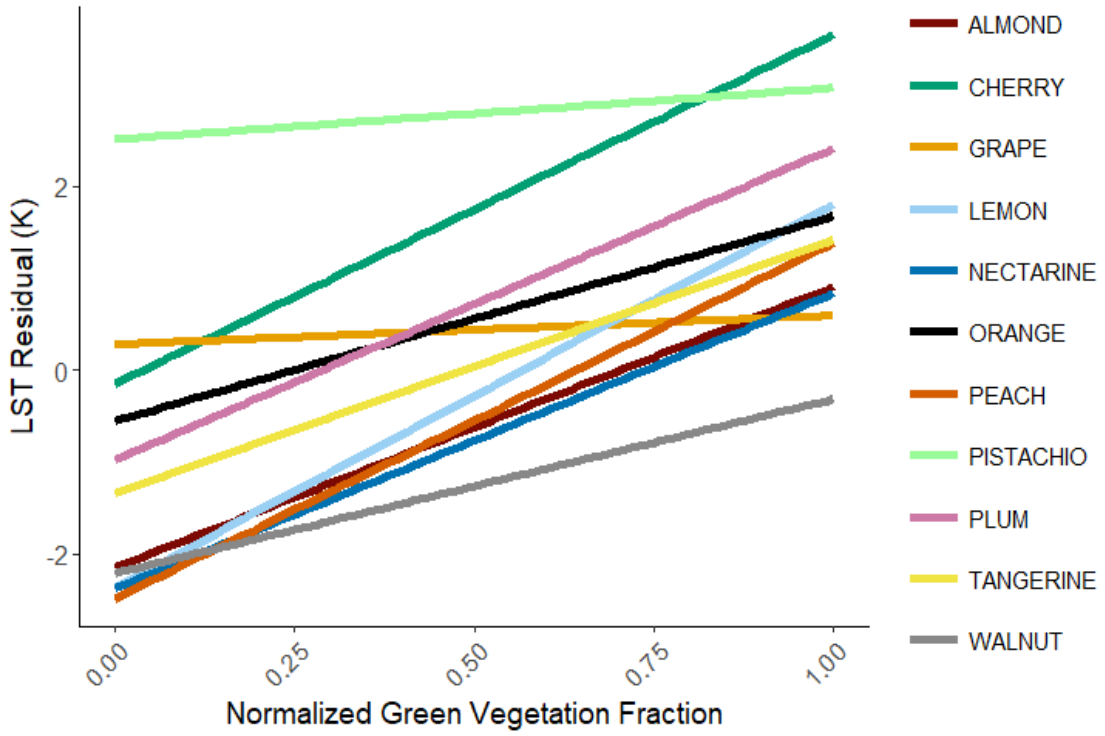

Figure 3.14: LST residual as a linear function of green vegetation fraction shows a positive correlation for most crops. Linear trend lines are plotted for each crop species over all three dates.

Fourth, an under or over estimation of fractional cover will propagate into LST residual errors; however, we do not believe that the distribution of errors will change the robustness of the results. Given mean LST values of 306.3 K, 321.3 K and 326.6 K for GV, NPV and soil respectively over all years and within the fields studied, the largest LST residual errors would result from a fraction error between soil and GV. MESMA has proven high fractional estimation accuracy for green vegetation. When looking at spectral separability between turfgrass, tree, paved, roof, soil, and NPV, Wetherley et al. (2017) found that mixtures of tree/soil were the second most separable pair after turfgrass/soil. Using synthetic mixtures, this study observed that soil, when mixed with tree, had a fractional accuracy of 0.976 while tree, when mixed with soil, had a fractional accuracy of 0.896.

Therefore, we believe that fraction errors between GV and soil will be less than 10%. Furthermore, partitioning the landscape into soil and green vegetation is a necessary step in estimating crop stress and water use, and is therefore included in comparable models such as the VHI and WDI. While any fractional cover estimate will be subject to error, we believe MESMA is an improvement over these other models for reasons that will be discussed in Section 4.2. Finally, we do not believe that the errors in temperature estimation that result from errors in fractional estimation will preferentially affect any specific crop species. Therefore, while there will be pixel-level error due to fractional cover estimations, these errors should balance out and allow for relative stress comparisons when analysis of crop temperatures is aggregated to the field and/or species levels.

Fifth, differences in flight timing will contribute to noise in the interpretation of results. Crop stress fluctuates with time of day, and plant transpiration has been found to plateau midday and then decrease in the afternoon as soil water content and soil water potential decrease (Lynn and Carlson, 1990; Olioso et al., 1996). Therefore, temperature residuals are not only a function of the overall health of the crop during the year and season the imagery was collected but also the water availability on the day and time it was captured. While flight timing should be considered when interpreting findings, we do not believe that the effect is significant enough to overwhelm the yearly signal of increasing stress that is likely due to drought. Temperature residuals were shown to increase from 2013 to 2015. If this trend were due to the timing that the data were collected, we would expect the timing to have a similar trend as the residuals. However, the flight in 2014 was flown latest in the day yet did not have the highest residuals. Additionally, 2013 and 2015, which were flown at similar times of day, had the greatest differences in average LST residual, which is the

opposite result as would be expected if flight timing were the main driver of residuals. Therefore, flight timing is an important factor to consider when interpreting LST patterns, but its effect on this study is assumed to be small. If designing a study to compare water stress between months or years, consistency in timing of acquisition would enhance interpretability of results.

Sixth, this study assumed that environmental variables such as air temperature, radiation, and wind did not deviate significantly across the study scene. In our study area, which has little variability in elevation and has similar vegetation types throughout, we assume the climate is relatively stable. However, some variability will exist across space that will cause error. If this model were applied to a study area that encompassed multiple climate zones, thermal endmembers would need to be calculated separately for each zone to account for known differences in environmental conditions. For this reason, we suggest that this method be implemented over relatively homogeneous areas, with respect to topography and climate.

Finally, this model requires a priori information about the landscape and informed knowledge to select appropriate thermal groups. In this study, a crop map that was compiled on-the-ground at the county level was used to inform thermal classes. In lieu of a similar map, crop information could also be gathered from a classification of VSWIR imagery (Shivers et al., 2018; Wardlow et al., 2007; Zhong et al., 2011) or from a national crop map such as the Cropland Data Layer (USDA, 2018). With that information, crops could be separated into groups that are similar physiologically and biophysically such that they are expected to have similar thermal behavior. One of the limitations of the model is its sensitivity to choice of thermal groups. While we expect this method to be transferable

to other regions, types of landscapes, and thermal groupings, further work would be necessary to test this hypothesis.

3.4.2. Benefits of proposed LST model for interpreting stress

This study found a significant inverse relationship between green vegetation and LST. Other studies have observed similar trends between temperature and vegetation (Lambin & Ehrlich, 1996; Nemani & Running, 1989; Roberts et al., 2015). However, unlike other models that use vegetation indices to account for this relationship, such as the VHI or WDI, our model uses a mixing model. The mixing model is an improvement upon the vegetation indices as it leads to a more accurate estimate of fractional cover in a diverse landscape such as our study area. NDVI is sufficient for estimating fractional cover in simple landscapes with little spectral variability, but a mixture model is better suited for estimating fractions in spectrally and spatially diverse landscapes (Xiao & Moody, 2005). NDVI is also sensitive to variability in soil background reflectance, which is accounted for with a mixing model. MESMA, in particular, has the added benefit of using multiple endmembers per surface cover component, which allows these components to be grouped by spectral similarity.

We found that there is significant thermal variability within the broad surface covers of GV, soil, and NPV. These findings imply that a detailed knowledge of the landscape, beyond basic surface cover fractions, should be considered for interpretation of LST in agricultural areas. We explored thermal patterns in agricultural orchards and found that core thermal differences exist between crop groups of citrus, perennial fruits, and nuts that may not be attributable to stress. These findings indicate that physiological differences between crops result in different thermal behaviors that will impact interpretability of stress. Results

are also in agreement with the observation of Roberts et al. (2015), who found that LST and GV cluster by dominant plant species in LST/GV space.

Moreover, we found that there is thermal variability in soil that is correlated to soil albedo and in NPV that is hypothesized to vary by structure. This result is consistent with studies of soil moisture, which have observed that moisture will lower the albedo and temperature of a dry soil (Liu et al. 2008; Lobell & Asner, 2002; Sandholt et al., 2002). The method detailed in this paper acknowledges the variability within soil, NPV, and GV and uses a crop map and MESMA endmembers to account for some of this thermal variability.

Current remote sensing methods that estimate agricultural stress either require field-specific inputs that limit the scale of applicability or are wide-reaching but too simplistic in their assumptions such that all GV, soil, and NPV are treated similarly regardless of structural complexity, albedo, or functional group. Field-level models such as the WDI and CWSI account for differences in species by requiring crop-specific data, but these intensive inputs limit broad spatial analysis. Other models that have been developed for analysis across large areas, such as satellite-based ESI and VHI, do not account for the degree of thermal variability that was found in this study to be present in an agricultural landscape. While ESI and VHI do use NDVI and, in the case of ESI, also LAI to account for thermal differences within green vegetation, these parameters will not account for thermal variability from soil type or moisture, NPV, or even species-level thermal variability. An advantage of this method is that it segments GV, soil and NPV into groups that should have similar thermal behaviors while requiring no site-specific inputs other than a crop map. Its internalized calibration makes this method scalable across time and space. In lieu of a crop map, MESMA endmember groups, such as were used for NPV and soil, may be a suitable

substitute for grouping GV into thermal classes. However, further study would be necessary to test this hypothesis.

3.4.3. Opportunities for agricultural applications

Monitoring crop stress is important in anticipating the future of the agricultural landscape and can provide insight into plant water status and plant stress that could help to identify unhealthy crops to mitigate impacts that could lead to decreased yields and economic losses. We found that thermal imagery collected at only one date per year over three years of drought was able to identify the species that were facing the highest degrees of stress, in agreement with county-level yield data. Previous studies have also observed correlation between thermal stress and agricultural yields. Thermal remote sensing has been observed to correlate with fruit quality in orchards with open canopies (Sepulcre-Cantó et al., 2007) and has been used as an indicator of regional agricultural drought as measured by crop yields (Anderson et al., 2016). Subsequent analysis of our model would be necessary to determine if the results are robust at the field level, but even the regional correlation with measured crop yields has important implications for farmers, policymakers, and scientists analyzing food and water resources.

Moreover, temperature patterns were correlated with expected ET rates for crops in California in a dry year, further bolstering the hypothesis that LST patterns can be used to infer information about crop water use and stress. We hypothesize that deviations in the expected linear relationship between ET and LST are the result of irrigation management decisions such as irrigation method, timing, or applied amount that will affect the health and productivity of the crops. ET rates were calculated under the assumption that crops were watered with surface irrigation systems, suggesting that expected ET rates would

increase by 3-6% if drip or micro irrigation were applied (Irrigation Training and Research Center, 2003). As the frequency of drip irrigation for orchards has increased dramatically in the past couple decades, this change in method may be a factor in deviations from the ET/LST relationship. We also hypothesize that deviations in the ET/LST relationship are a factor of drought management techniques such as reduced watering. In line with this assumption, walnuts consistently had the lowest temperatures and residuals of the three nut crops in the study. This finding is consistent with suggested drought irrigation management techniques that recommend against deficit irrigation for walnuts as they are highly susceptible to damage if faced with water stress and are not as tolerant to these practices as either almonds or pistachios (University of California Division of Agriculture and Natural Resources, 2018). The lower walnut temperature may, therefore, be the result of continued, consistent irrigation in comparison to almonds and pistachios, which receive deficit irrigation. The temperature residuals capture the difference between expected and measured temperature and therefore act to as an important source of information about ET rates, the irrigation management practice, and stress. These thermal analyses are important for prioritizing water resources, especially in times of drought when water is limited.

Additionally, maps of thermal stress could be valuable to assess the representativeness of in situ measurements of carbon dioxide, water vapor, sensible heat, or other fluxes over a heterogeneous landscape (e.g., Barcza et al. 2009). This method of quantifying stress could also be complementary to surface energy balance models such as Disaggregated ALEXI (DisALEXI; Anderson et al., 2007a, 2007b) and Mapping Evapotranspiration with Internalized Calibration (METRIC; Allen et al. 2007). As our approach provides a relative measure of stress and DisALEXI and METRIC estimate actual ET, the surface energy

balance models could be used to test the sensitivity of our approach to changes in ET. Alternately, the segmentation of soil and NPV into thermal classes in our method may be of use for refining the evaporation component of DisALEXI or METRIC for increased accuracy in crop ET estimation.

Our approach has the added benefit of requiring only VSWIR imagery, thermal imagery, and a crop map that provides a level of detail of, at minimum, plant functional groups, and these minimal inputs allow for ease of implementation. Given these inputs, the approach suggested in this paper is probably best suited for agricultural applications at a spatial scale where environmental variables do not vary highly, such as the study scene in this paper. Within a relatively homogenous area, this method could be applied routinely using consistent thermal groups in order to identify which fields are most stressed and/or to gain information about irrigation management practices, particularly during drought as studied in this paper. In order to improve the ability of this method to capture within crop change in drought stress through time, further analysis would need to be conducted with a dataset that collects at approximately the same time for every capture. With our dataset that contained large differences in time of capture, these timing differences made such analyses beyond the scope of this paper.

3.4.4 Relevance to the SBG and ECOSTRESS Missions

This study showed that thermal signatures of agricultural crops are correlated with crop species and fractional cover. Therefore, LST data on its own without information about surface structure and composition is challenging to interpret in the context of crop stress. The SBG mission would provide spatially and temporally paired thermal and VSWIR imagery globally which would allow for detailed analysis of LST patterns that take into

account fractional cover and surface type. The ability of SBG to monitor crop stress would be enhanced by a crop classification that could group crop fields into relevant thermal classes, removing the need for accurate GIS data layers. Future studies are needed to assess the accuracy of SBG for such a classification and further evaluate its suitability to detect crop stress independent of a crop species map. The SBG mission will allow for further exploration of crop temperatures as they change temporally and as they differ across different climates and landscapes.

In addition to SBG, with the ability to track diurnal changes in plant water globally, ECOSTRESS is well positioned to lead scientific understanding of crop water stress as it changes spatially and temporally (Fisher et al., 2015). This study provides rationale for accounting for species and soil type when analyzing thermal data and enhances the importance of pairing the thermal data with ground data or VSWIR imagery from Landsat or MODIS that can enhance understanding of surface characteristics. Further, with paired VSWIR imagery, it suggests the potential for extrapolating the methodology in this paper for global study of crop tree stress.

3.5. Conclusions

This paper used hyperspectral VSWIR data, TIR imagery, and a GIS data layer of crop species from 2013, 2014, and 2015 to evaluate LST patterns across an agricultural landscape of perennial crops in Central Valley of California during a severe drought. The findings provided enhanced understanding of the thermal complexity that exists within orchards, and it proposed an approach to capturing this variability by using LST to derive a quantitative estimate of thermal stress. Hyperspectral and thermal imagery can together provide information about the surface characteristics and composition of the landscape and

water stress as a function of the temperature of that surface. We found that multiple thermal classes exist within GV, NPV, and soil groups, and that fractional cover information was necessary to understand thermal patterns in agricultural areas. Through estimating LST and calculating temperature residuals, our method accounted for the structural complexity within the agricultural orchards and provided an indicator of stress that made thermal patterns comparable between species and that was closely related with regional crop yield data. With the future launch of the SBG satellite and the successful deployment of the ECOSTRESS instrument, this method shows promise for broad agricultural analysis with results that would be of value for agricultural management, food systems monitoring and water resource accounting.

Chapter 4: An analysis of atmospheric water vapor variations over a complex agricultural region using airborne imaging spectrometry

With Dar A. Roberts, Joseph P. McFadden, and Christina Tague

4.0. Abstract

Understanding atmospheric water vapor patterns can inform regional understanding of water use, climate patterns and hydrologic processes. This research uses Airborne Visible Infrared Imaging Spectrometer (AVIRIS) reflectance and water vapor imagery to evaluate spatial patterns of water vapor in California's Central Valley on a June date in each of 2013, 2014, and 2015, and relates these patterns to surface characteristics and atmospheric properties. We analyze water vapor imagery at three scales: pixel, regional and agricultural field, and test a series of hypotheses for how the slope, intercept, and trajectory of water vapor trends will interact with the landscape in a highly diverse and complex agricultural setting. In agreement with our hypotheses, at the field scale, we find significant quadratic relationships between water vapor slope and wind magnitude in each of the three years ($p<0.001$). Results showed a strong positive correlation between crop water use and the frequency with which crops showed directional alignment between wind and water vapor ($r=0.67$). At the regional scale, we found patterns of water vapor that support advection of moisture across the scene. However, in contrast to some of our hypotheses, the results showed inverse correlations of -0.35, -0.34, and -0.25 between water vapor slope and field size in 2013, 2014, and 2015. We also found no correlation in any year between green vegetation fraction and vapor slope ($r =0.001$ in 2013, $r=-0.02$ in 2014, $r=0.02$ in 2015). These results lead us to conclude that accumulation of water vapor above fields in these scenes is observable with AVIRIS-derived water vapor imagery whereas advection at the field level is obscured by variable winds, differences in field structure and composition, and smaller-scale patterns of vapor. Based on these results, we identify new opportunities to use

and apply water vapor imagery to advance our understanding of hydro-climatic patterns and applied agricultural water use.

4.1. Introduction

Atmospheric water vapor is a critical element of climate, an indicator of land surface hydrologic processes, and a potent greenhouse gas (Ross & Elliott, 2001; Trenberth et al., 2005). As such, analysis of vapor patterns at a fine spatial scale can inform climate and plant water use studies (Gaffen et al., 1992; Ogunjemiyo et al., 2002). Imaging spectrometers such as NASA's Airborne Visible Infrared Imaging Spectrometer (AVIRIS) measure reflected radiance at fine spatial and spectral resolution, and in so doing provide measurements of column water vapor as well as a highly detailed reflected signal from the land surface below (Gao and Goetz, 1990; Green et al., 1998; Thompson et al., 2015). These two spatially corresponding products allow us to uniquely observe surface processes and characteristics as they relate to the atmospheric patterns above them in ways not previously possible. As such, this research proposes to leverage water vapor and reflectance imagery to observe and assess spatial patterns of water vapor in the Central Valley of California to evaluate the assets and limitations of this dataset for evaluation of agricultural water use.

Observation and evaluation of water vapor over agricultural fields in California's Central Valley have substantial value for water resource management, irrigation assessments, and regional climate patterns. The Central Valley contains one of the world's largest contiguous areas of high irrigation density (Siebert et al., 2007) with more than 3.6 million irrigated hectares of farmland (Mount et al., 2014) that use over 80% of the state's managed water supply (CA DWR, 2014). Worldwide, arid and semi-arid regions such as

the Central Valley see upwards of ninety percent of precipitated water returned back to the atmosphere via evapotranspiration (ET) (Glenn et al., 2007). In the Central Valley, where precipitation is low and managed water inputs are extreme, annual ET exceeds precipitation by about 60% (Faunt, 2009; Lo & Famiglietti, 2013). These extreme irrigation inputs, therefore, significantly modify the spatial and temporal distribution of hydrologic flows across the region by transforming liquid water resources (from the surface or ground) into transpired atmospheric water vapor (Gordon et al., 2005) that can be transported and distributed as rainfall elsewhere (Lo & Famiglietti, 2013). Further, as local atmospheric water vapor is intensified by ET, it is indicative of agricultural water inputs and crop functioning throughout the region.

Imaging spectrometers such as AVIRIS quantify column water vapor using several water absorption features across the infrared portion of the electromagnetic spectrum (Carrere & Conel, 1993; Gao & Goetz, 1990; Roberts et. al, 1997). Atmospheric water vapor absorption features occur at 0.94, 1.14, 1.38 and 1.88 μm, and the relative depth of these features can be used to derive atmospheric water content (Gao & Goetz, 1995). Hyperspectral imagery is uniquely suited to estimate water vapor because its high spectral resolution captures water absorption features that multi-spectral sensors, such as Landsat, are designed to avoid. In addition, the fine spatial resolution of the retrievals (~18 m) enable observation of water vapor patterns that are obscured in spatially coarser imagery, such as MODIS (1 km) and GPS.

While water vapor imagery is produced as a byproduct of most visible to shortwave infrared (VSWIR) reflectance retrievals, few analyses have been conducted with this rich dataset, leaving many questions as to the utility of this data unanswered. A notable

exception is the work of Ogunjemiyo et al. (2002) who studied water vapor over poplar plantations in Washington State to assess the feasibility of using AVIRIS-retrieved column water vapor as a tool to study plant ET. That study proposed a conceptual model of water vapor and its relationship to the surface (Fig 4.1), hypothesizing that plants with higher rates of transpiration will produce more water vapor, which will advect downwind and accumulate to a level detectable in the imagery, and that crops with higher water use rates will have steeper water vapor slopes, modified by wind speeds. Ogunjemiyo et al. (2002) found that the patterns and magnitude of retrieved water vapor in their study areas were consistent with wind direction and reasonable transpiration rates for poplars with unlimited access to water, concluding that AVIRIS water vapor is sensitive to ET under certain boundary layer conditions. However, while transpiration is the dominant source of water vapor in the atmospheric boundary layer (Harwood et al., 1998; Moreira et al., 1997; Yepez et al., 2003), directly relating water vapor to the agricultural field that produced it will depend on multiple factors including atmospheric turbulence, time of day, wind magnitude and direction, and atmospheric stability.

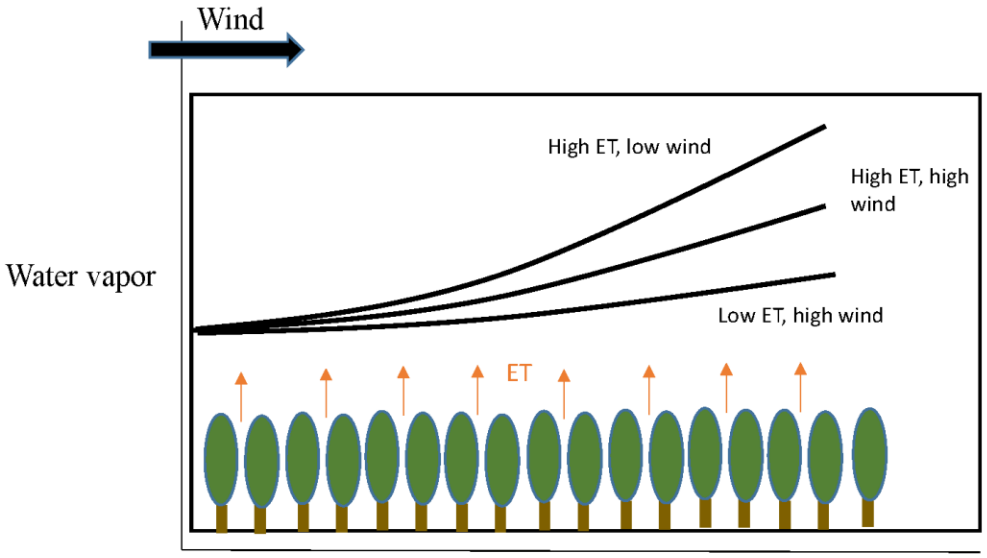

Figure 4.1: Conceptual schematic of columnar water vapor as it is affected by ET rates and wind, modified from Ogunjemiyo et al. (2002)

Here, we build upon the work of Ogunjemiyo et al. (2002) to further evaluate if AVIRIS is sensitive to field scale ET by testing a series of specific hypotheses to investigate how AVIRIS estimates of water vapor vary with the surface properties and atmospheric conditions that might be expected to influence water vapor in a complex agricultural environment (Table 4.1). Relating water vapor patterns to crop water use will be more challenging to isolate in the Central Valley of California, which includes a complex arrangement of agricultural fields that vary in crop types, land management, irrigation practices, field sizes, and vegetated cover fractions. Relative to the large, single-crop, well-watered field studied in Ogunjemiyo et al. (2002), the heterogeneity in crop type and water availability, smaller field sizes, and the semi-arid climate in our study area add complexity to the interaction between the atmosphere and underlying physical and plant physiological characteristics. Table 4.2 summarizes additional mechanisms that might influence the interactions summarized in the simple conceptual model (Figure 4.1). This

study will also conduct analyses of water vapor at three scales – pixel, field, and scene – using three AVIRIS-derived water vapor images collected in early June of three different years. Our hypothesis (Table 4.1) are designed to refine understanding of whether consistent (in time and space) relationships between imagery, atmospheric conditions, and surface properties are derivable from hyperspectral imagery in a complex agricultural landscape and at which scales. Results will identify opportunities and limitations of using water vapor imagery to study ET at the ground surface in this important agricultural region.

Table 4.1. Hypotheses to be tested in this study

	Hypotheses
	Pixel Level
A	Healthy, transpiring vegetation will have more water vapor above it, as shown through a positive correlation between green vegetation fraction and water vapor concentration and a negative correlation between land surface temperature and water vapor concentration.
	Scene Level
B	Water vapor imagery will show advected moisture in the downwind direction.
	Field Level
C	If there are stable and moderate winds, horizontal gradients of water vapor will form above evapotranspiring fields.
D	If winds are light or inconsistent, gradients will not be observed, but water vapor will build up over evapotranspiring fields.
E	High winds will lead to shallower slopes of water vapor gradients above fields
F	In evapotranspiring fields, wind direction and water vapor trajectory will closely align.
G	Larger fields will show larger water vapor gradients.
H	The slope of water vapor gradient will positively correlate with green vegetation fraction within vegetated fields.

I	Bare fields or sparsely vegetated fields will not show water vapor gradients.
J	Fields that are not evapotranspiring will show no gradients.
K	Crops that have higher ET rates will have more pronounced (steeper) water vapor gradients above them.

Table 4.2. Canopy-level and field level factors affecting plant/atmosphere interactions (Jarvis & McNaughton, 1986)

Factor	Effect
Crop Type	
Aerodynamic roughness	Aerodynamically rough vegetation is more coupled to the atmosphere because it creates turbulence which transfers heat more readily from the surface to the atmosphere. Short, smooth surfaces are less coupled than taller, rougher surfaces.
Vapor pressure deficit (VPD)	Transpiration increases with increasing VPD up to a certain point at which stomata close and transpiration declines. The tipping point differs among species (Asbjornsen et al., 2011).
Canopy conductance	The rate at which water vapor exits plant stomata will moderate the concentration of vapor above the canopy, and this varies by plant species.
Field Size	
Edge effects	The size of the field affects the proportion of land that exists at the boundary with another field. Smaller fields are more susceptible to edge effects of neighboring fields than larger fields.
Climatic	

Variability	A larger and more dynamic study scene will experience greater ranges in wind speed and direction and vapor pressure deficit than a more localized study area.

4.2. Methods

4.2.1. Study area

This research focuses on a long transect of the California Central Valley that is also known as the "Soda Straw" in the Hyperspectral Thermal Imager (HyspIRI) Airborne Preparatory Campaign flight plan (Fig. 4.2). The study area includes portions of Fresno, Tulare, Kern, and Kings Counties, three of the top four leading agricultural counties in California (CDFA, 2016). The study area is part of the Tulare Lake Hydrologic Region, which comprises the southern third of the Central Valley and is the largest agricultural region in California with about 1.2 million irrigated hectares out of its 4.4 million hectares total (CA DWR, 2009). The region is prosperous for agriculture partially because of its long growing season, with moist winters often blanketed by fog and dry summers (CA DWR, 2009). Tulare Lake is the driest region of the Central Valley, receiving an average of less than 25.4 cm of precipitation a year (CA DWR, 2009; Carle, 2004).

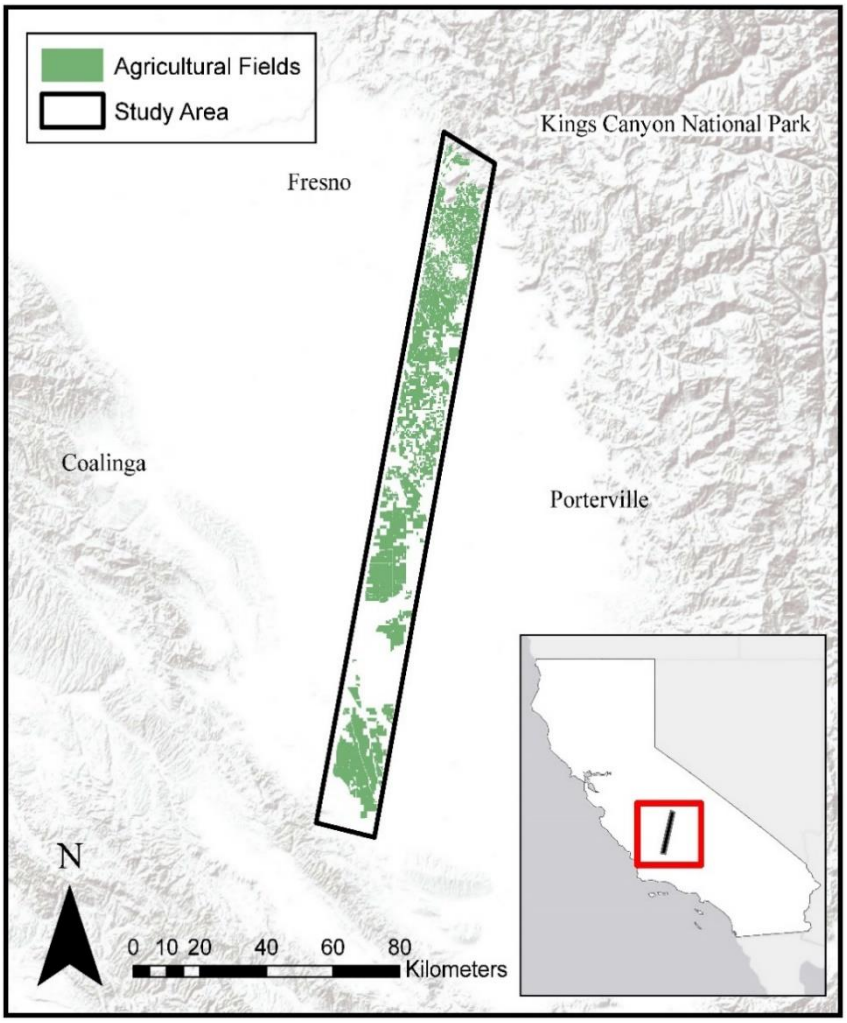

Figure 4.2: Study area within California's Central Valley

4.2.2. Data

4.2.2.1. Radiance and reflectance imagery

The Surface Biology and Geology (SBG) mission has been identified in the 2017 Decadal Survey as a designated program element prioritized for development as a means to enhance our ability to monitor ecosystems, natural hazards, and land use over time (National Academies of Sciences, Engineering, and Medicine, 2018). The proposed sensor will capture a large number of spectral bands in the visible and shortwave infrared at a 30 m resolution, as well as multiple bands in the thermal infrared (TIR) at a 60 m resolution. In

order to simulate the capabilities of SBG, the HyspIRI Airborne Campaign (HAC) flew the AVIRIS and MODIS-ASTER Simulator (MASTER) instruments throughout California seasonally from 2013 to 2017 at an altitude of 20 km. AVIRIS is a 224 band imaging spectrometer that captures wavelengths from 350 nm - 2500 nm at approximately 10 nm increments (Green et al., 1998). MASTER captures 8 bands in the TIR region from 4-12 μm (Hook et al., 2001). NASA's Jet Propulsion Lab (JPL) preprocessed the imagery and produced orthorectified, high spectral resolution radiance and atmospherically-corrected reflectance imagery from AVIRIS at an 18 m spatial resolution and a land surface temperature (LST) product from MASTER at a 36 m spatial resolution. AVIRIS imagery was resampled to 36 m by pixel aggregation for consistency with LST imagery. Three dates of imagery from HAC were analyzed: June 6, 2013, June 3, 2014 and June 2, 2015 collected at 18:25, 21:41, and 18:59 UTC respectively.

4.2.2.2. Water vapor imagery

Pixel-level water vapor estimates were calculated from the radiance imagery using Atmospheric CORrection Now (ACORN) 6.0 atmospheric correction software (ImSpec, 2002). ACORN 6 models atmospheric gas absorptions and scattering effects using nonlinear least-squares spectral fitting with look-up tables of water column densities generated from MODTRAN 4 radiative transfer runs (Berk et al, 2017; Kruse, 2004). The result is pixel-level water vapor and liquid water estimates over the entire study scene. ACORN 6 was run in mode 1.5 for atmospheric correction of hyperspectral data. Chosen parameters include the use of both 940 nm and 1140 nm to derive water vapor, a mid-latitude summer model, an average surface elevation of 100 meters, automated estimate of visibility and artifact suppression.

4.2.2.3. Surface and field properties

The studied agricultural landscape was characterized using both the reflectance imagery and a geographic information system (GIS) layer of field data. Multiple Endmember Spectra Mixture Analysis (MESMA; Roberts et al., 1998) was run on the AVIRIS reflectance imagery to estimate pixel-level fractions of green vegetation (GV), soil, and non-photosynthetic vegetation (NPV). MESMA is a spectral mixture technique that models the spectral signature of each pixel using a linear combination of spectra from the classes within the scene. The chosen endmembers for each class are allowed to vary on a per-pixel basis to capture the diversity of spectra contained within GV, NPV, and soil. The resultant product is a sub-pixel map of vegetation fraction, both senesced and green, and soil throughout the study area. MESMA was run on each of the three image dates using one spectral library of 40 image-selected endmembers (22 GV, 8 NPV, 10 Soil) that were collected from all three dates.

In addition to cover fractions, we obtained field size and crop species data. This information was obtained from GIS crop data layers provided by Tulare, Kings, Kern, and Fresno Counties. Field boundaries and crop information is gathered as part of a California's required registration and permitting of agricultural fields that use pesticides. Field sizes ranged from <100 m^2 to 2.7 km^2. Using the MESMA results and the crop map, which delineates field boundaries, a mean estimate of GV, Soil, and NPV was calculated for each field.

4.2.2.4. Wind patterns

An expected driving factor of water vapor patterns is wind, both its directionality and its magnitude. Therefore, we interpolated a map of wind over the study area during the study

times and dates in order to create an estimate of wind activity against which to compare water vapor patterns. To calculate wind speed and wind direction, we relied on weather station data from 18 meteorological stations in or within close proximity to the study area (Fig 4.3). Weather stations used in the analysis are managed by various sources including government agencies, private firms, and educational institutions. Meteorological data were downloaded from the MesoWest and California Irrigation Management Information System (CIMIS) networks. For each station, the wind speed and direction that most closely matched the flight time for each of the three dates were recorded. All observations were within 30 minutes of the flight time. Using the 18 data points for wind magnitude and direction, data were spatially interpolated across the study area using an inverse weighted distance (IDW) formula. IDW relies on the idea that each estimated data point will be influenced by the known data surrounding it, and this influence will diminish with distance. IDW has been widely used in climatic studies for interpolating data such as temperature, rainfall, and wind (Legates & Willmott, 1990) and is computationally efficient (Dirks et al., 1998), but has been found to have low accuracy when data is sparse or unevenly distributed (Luo et al., 2008). As our study area is relatively flat and stations are somewhat evenly disbursed, we felt IDW would be an appropriate and efficient method for wind interpolation. The result is a pixel-level estimation of wind speed and wind direction across the study area for each of the three study dates.

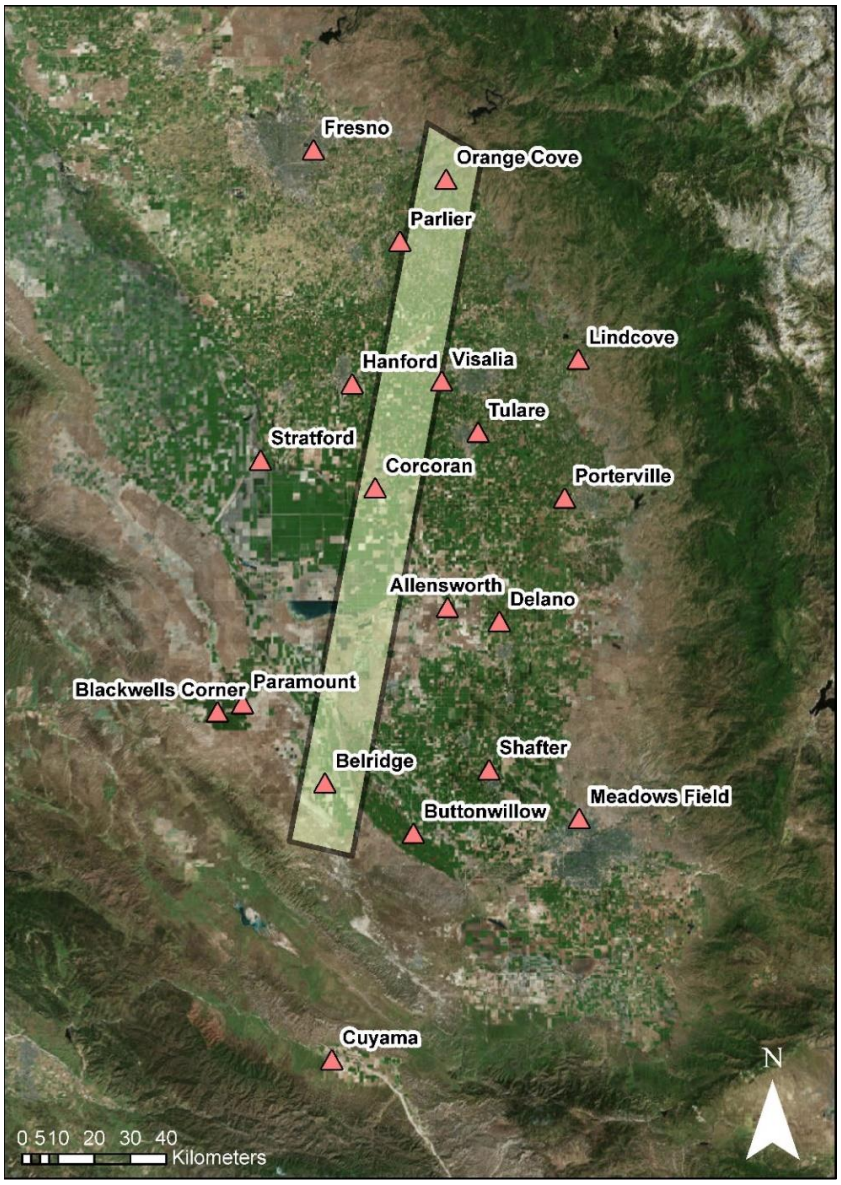

Figure 4.3: The 18 meteorological stations used to interpolate wind data are shown in juxtaposition with the study site shown in light green.

4.2.2.5. Field-level water vapor trends

Because small-scale trends of water vapor are observed in the scene and crops are not uniformly distributed throughout the area, direct comparisons of water vapor concentrations between fields or crop types would not be suitable for ET evaluation. Therefore, most of the analyses in this study area are conducted using field-scale, normalized water vapor values.

In order to normalize comparisons, intra-field slope, trajectory, and intercept were proposed. To quantify the concentrations and gradients of water vapor as they vary over field of crops, a 3D linear trend surface was fit to the water vapor data over every field in the crop map for each year (n=2599 for 2013; n=2395 for 2014; n=3197 for 2015). Using the fitted surface, an intercept, slope, and trajectory were calculated for each field to explore the magnitude, rate of change, and directionality of the water vapor above it. The slope acts as a measure of moisture advection as a factor of wind at the field-level. The intercept is an important measure of water vapor at both the field and scene levels. At the scale of an individual field, the intercept quantifies the build-up of moisture over a field, while at the scale of the entire study site, the spatial pattern of intercepts highlight advection of moisture across the scene. The trajectory is equivalent to the azimuth of the water vapor trend at the field-level. To assess the strength of the modeled, fitted surface, r-squared and p-values were also calculated. Only fields that had statistically significant linear trends ($p<0.05$) were analyzed. The water vapor occurring above an example field and its corresponding fitted plane are shown in Figure 4.4.

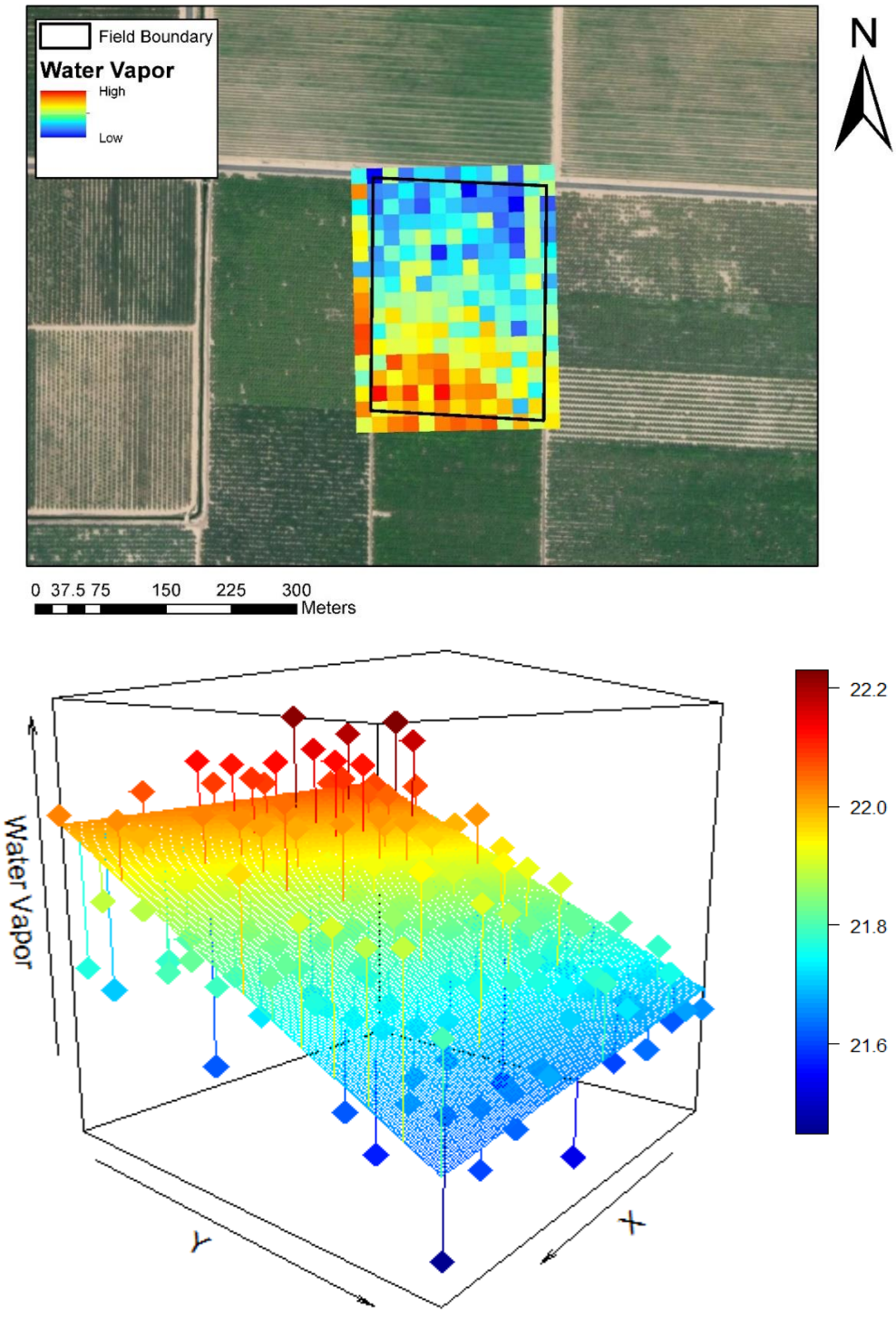

Figure 4.4: Water vapor trend occurring over an example field**.** The top graphic shows pixel-level water vapor measurements from 2013 from AVIRIS above polygon "152351", a field of nectarines. The bottom plot illustrates the same water vapor measurements, fitted by a linear trend surface. Column water vapor values reported in millimeters. Slope = 0.99 and r^2 =0.61.

4.2.3. Analysis

4.2.3.1. Water vapor pixel-level analysis

Water vapor concentrations were explored as their distributions vary by day and within the scene. Within each scene 1,000 random pixels were selected and a Pearson's R was calculated to analyze the correlation between GV fraction and LST with water vapor concentrations in order to test Hypothesis A. GV fraction was obtained from MESMA and LST from the corresponding MASTER imagery. If expected correlations are found, these correlations would be indicative of water vapor relating to the surface beneath it. Green vegetation transpires and produces water vapor, which will lead pixels with more vegetation to have higher water vapor. These surfaces should also have lower temperatures as evapotranspiring plants shed energy through latent heat.

4.2.3.2. Water vapor across-scene analysis

We tested Hypothesis B by examining patterns of water vapor intercepts against prevailing wind direction. Over the study area, we expected the water vapor concentration, as quantified through the intercept of the fitted water vapor plane, to increase downwind due to moisture advection. For example, if the wind is blowing from the North, we would expect fields in the southern part of the study area to show higher intercepts than fields in the northern part of the study area. We evaluated this hypothesis in each of the three years by mapping out intercepts in the study area and qualitatively assessing their relationship to the calculated wind direction.

4.2.3.3. Water vapor field-level analysis

At the field level, we analyzed gradients of water vapor as they vary over agricultural fields in line with expectations of vapor as conceptualized in Figure 4.1 and as explained

through Hypotheses C through K in Section 1. As such, we tested Hypotheses C, D, E, and F by evaluating the relationship between wind speed and direction with the slope of water vapor. Even if pixel or scene-level trends were not identified in an image, we included all dates of imagery in the field-level analysis as we hypothesize that trends may be happening at variable scales so null results at one level does not preclude significant results at another. The trends of water vapor above fields will be a factor of both wind speed and direction. We expected to find that, within fields predominately covered in green vegetation (GV>0.5), the relationship between water vapor slope and wind would show a quadratic relationship with relatively high or low winds creating water vapor gradients less steep than winds that are of an "intermediate" magnitude. Higher winds will move water vapor at a faster rate, which will lead to shallower gradients. However, this concept should only hold once the winds reach a certain threshold magnitude and a stable directionality as light and/or inconsistent winds will not produce any gradients. To test this hypothesis we plotted wind magnitude against water vapor slope in each of the three years. We also expected to find water vapor surfaces that aligned in directionality with the wind. We calculated the difference between the estimated wind direction and the trajectory of the water vapor above each field as the directional difference. For those fields that had directional differences of less than 30° and a statistically significant slope of vapor, we analyzed their characteristics such as crop type and GV fraction to understand what types of fields our set of hypotheses holds for.

Second, we tested the impact of field size on water vapor slope in fields of >50% GV to examine Hypothesis G. We plotted field size against water vapor gradient while hypothesizing that we would find a positive relationship. Steeper gradients would be

expected above large fields as they have a larger surface area over which the vapor can advect.

Third, we observed the relationship between GV fraction and water vapor slope in order to test hypotheses H and I. We separated fields into groups of similar field size to control for the impact of this factor and then studied the correlation between green vegetation cover and water vapor slope and intercept within each of those groups. We hypothesized that fields with lower vegetation cover (<50% GV) would show a poor relationship between GV fraction and water vapor slope and/or intercept while fields containing a majority GV fraction (>50% GV) would have a positive correlation with water vapor slope and/or intercept. We used a 50% GV threshold as was set in Shivers et al. (2018). Field-level correlations between GV and intercept would be expected in situations with low winds and higher build-up of water vapor whereas strong correlations between GV and slope would be expected if consistent, moderate winds created advection of moisture across fields. Positive correlations would indicate that fields with more transpiring vegetation are adding more moisture to the air than less vegetated fields. A higher concentration of water vapor would be confirmed though a positive correlation with water vapor slope if winds are consistent and moderate, or an increase in intercept if winds are faint and/or variable.

Fourth, this study evaluated Hypotheses J and K by evaluating the slopes and intercepts of the fitted water vapor surfaces over fields of different irrigated crop species. These intercepts indicate the magnitude of water vapor above a field while the slope is indicative of the trend of vapor over a field. A one-way ANOVA was performed to assess differences in slopes between the crop species, and results were evaluated with expected ET rates. ET rates were approximated using the expected crop ET coefficient for irrigated crops for June

in the Southern San Joaquin Valley of California in a dry year (Irrigation Training & Research Center, 2003). We expect crops that transpire more to have significantly higher slopes than crops with lower ET rates.

To further examine expected patterns of water vapor as it relates to ET while controlling for some level of complexity within the scene, we chose three crops that are prevalent in the study area and looked at their LST as it related to water vapor slope. We explored water vapor over fields of alfalfa, almonds, and cherries. We included all fields which had a fractional green cover of 50% or more. We aimed to investigate the hypothesis that fields with lower temperatures would have steeper water slopes. Fields with lower LST are assumed to be healthier and less stressed than those with higher LST because plants that have adequate water will transpire and cool themselves (Jackson et al., 1981; Tanner, 1963).

4.3. Results

Water vapor concentrations varied significantly between dates with mean values of 21.1 mm, 10.6 mm, and 17.0 mm in 2013, 2014, and 2015 respectively (Figure 4.5). While 2014 and 2015 had normal distributions, 2013 showed a bimodal distribution. The image from 2015 had the least variance in water vapor values with a standard deviation of 0.99 mm as compared to 1.46 mm and 1.28 mm in 2013 and 2014.

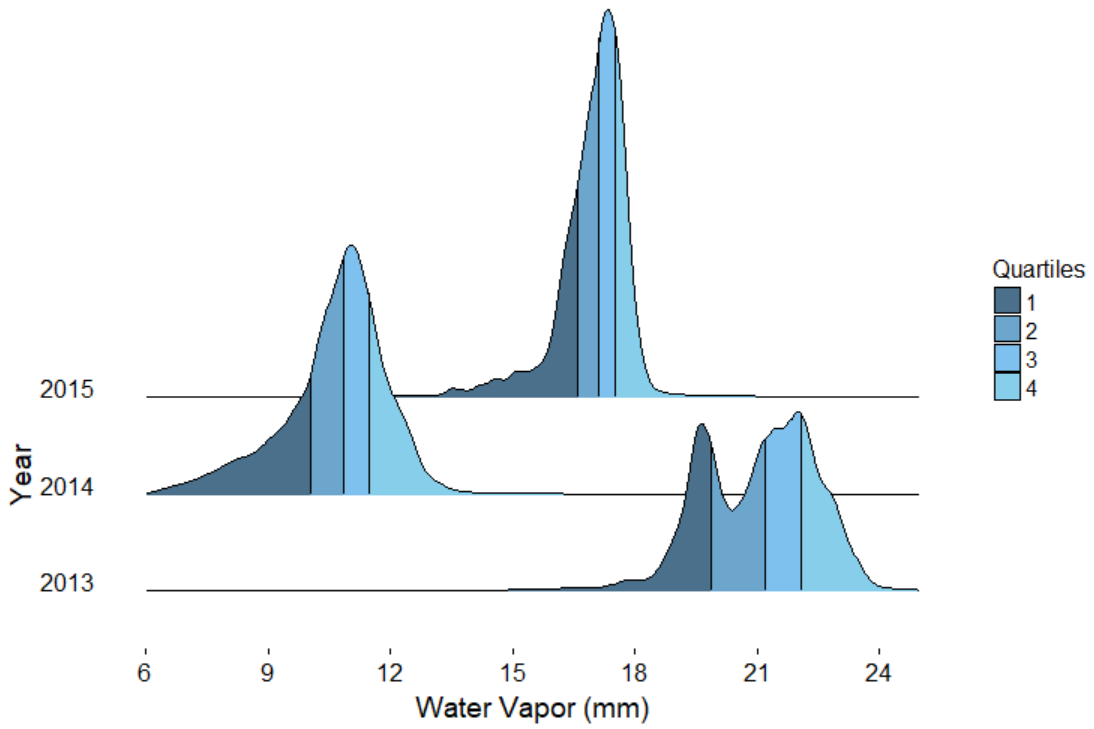

Figure 4.5: Water vapor distributions by year

Calculating linear surface trends of water vapor over fields, in 2013, 84% of the 2,591 fields had statistically significant water vapor surface trends. In 2014, 98% of the 2,351 fields had significant trends, and 92% of the 3,186 fields in 2015 did. The average slopes from 2013, 2014, and 2015 were 0.86, 1.17, and 0.70 µm of water vapor per meter of field respectively.

4.3.1. Pixel-level water vapor correlations

At the pixel-scale, the imagery from 2013 and 2015 showed weak positive correlations between water vapor concentration and GV fraction (r, 2013 = 0.24, r, 2015 = 0.26) while the imagery from 2014 showed no correlation (r=0.01). Imagery from 2013 and 2015 also showed the expected negative correlations between both LST and water vapor (r, 2013 = -0.33, r, 2015 = -0.16) while 2014 did not. These results further suggest that the imagery

from 2013 and 2015 are strong candidates for surface-atmosphere interaction analysis as they show patterns that hold with Hypothesis A.

4.3.2. Scene-scale spatial trends in water vapor concentrations

The three dates of imagery showed different spatial trends of water vapor. In 2013, water vapor showed a clear increasing trend from southwest to northeast, which is noticeable but not as defined in 2015 (Fig 4.6). The 2014 and 2015 scenes showed decreasing water vapor values in the northernmost portion of the scene as the Central Valley transitions into the mountains and the elevation increases. Besides the decreasing water vapor in the northernmost part of the scene, the remainder of the 2014 image is not indicative of any other trends.

When observing the imagery at a larger scale, the water vapor from 2013 and 2015 shows strong coupling with the ground surface below with agricultural field boundaries clearly defined. This result may be indicative of surface-atmosphere interactions or simply an artifact of the reflectance retrieval. In contrast, the 2014 imagery shows patterns of vapor that are more resonant of vapor or clouds that do not relate directly to the surface structure below it. We hypothesize that the difference may be attributable to the moisture level of the atmosphere, the differences in the timing of image acquisition, or the height of the water vapor in the scene. The 2014 imagery had both the driest atmosphere at 10.6 mm and also was the image that was acquired latest in the day. Given the appearance of the water vapor imagery, we hypothesize that the water vapor in 2014 was located well above the terrain while the water vapor in the 2013 and 2015 images were lower in the atmosphere, closer to the terrain. If our study site had larger elevation gradients, we could

test this hypothesis with the method laid out in Roberts et al. (1997). However, the flatness of our study area precludes such an analysis.

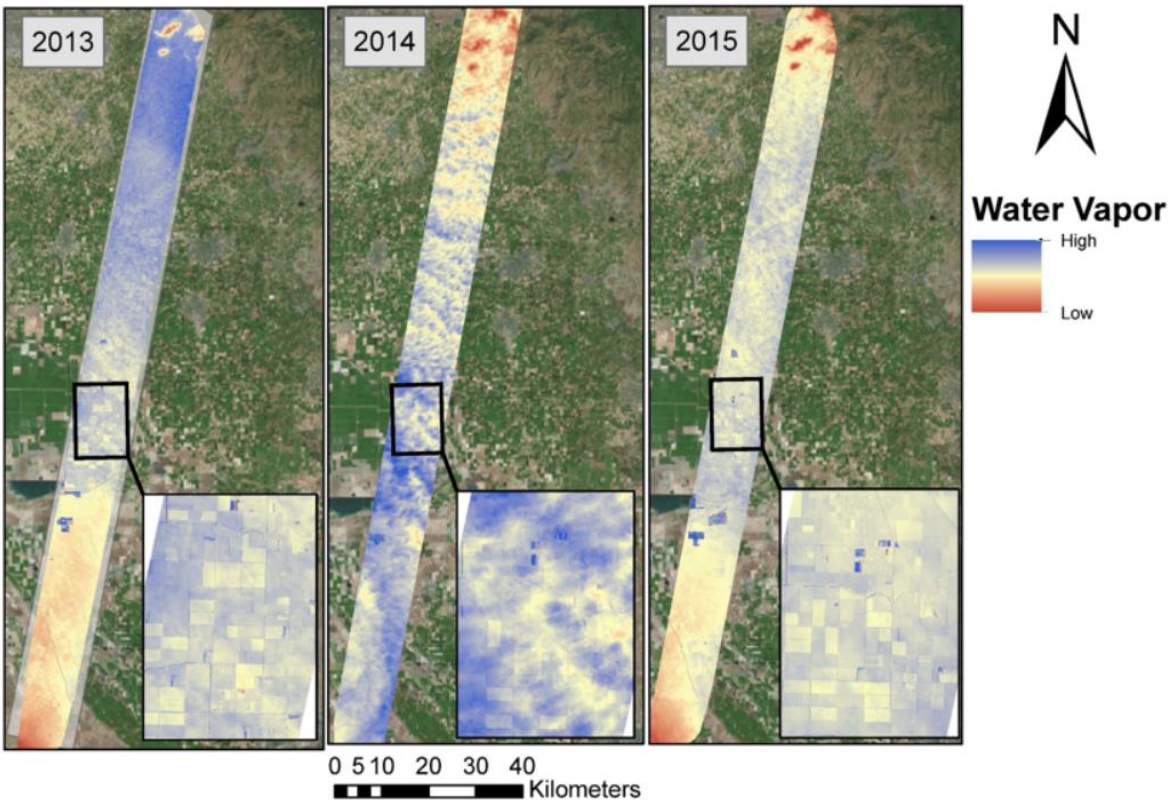

Figure 4.6: Water vapor images produced using AVIRIS radiance imagery and ACORN reflectance retrieval algorithm

Computation of water vapor intercepts and interpolation of wind directionality allowed for comparison between water vapor abundance and patterns of wind as laid out in Hypothesis B. Figure 4.7 shows the directionality of the wind and the water vapor intercept maps side-by-side for comparison. Of the three dates, the 2013 imagery shows the most clear pattern of advected moisture that generally agrees with the wind map, especially in the northern portion of the study area. The intercept map shows water vapor concentration increasing from south to north while the wind direction map shows a south to north trend of wind in the northern part of the study area. As crops transpire and water vapor advects, the

intercepts above fields show increasing moisture. The southern portion of the study area shows less agreement with winds, indicating winds coming from the northeast but a water vapor gradient increasing from west to east. We hypothesize that this may be due to differences in temporal scales or wind interpolation error, as noted in the discussion. The 2014 and 2015 images show water vapor that are not as clear in their trends. The 2014 wind map shows winds primarily from the north and west. The northern winds do generally agree with water vapor intercepts that seem to increase from north to south. The 2015 water vapor intercepts show patterns that are somewhat similar to 2013 with a general south to north increase in moisture, except for in the most northern portion of the flight line. Variability in winds makes evaluation between intercepts and trends challenging. Moreover, while the wind map is a snapshot at the time of flight, the intercept map likely represents a trend of water vapor over a time period of many hours, which further complicates analyses. However, results show some approximate agreement between winds and advected moisture, especially in 2013.

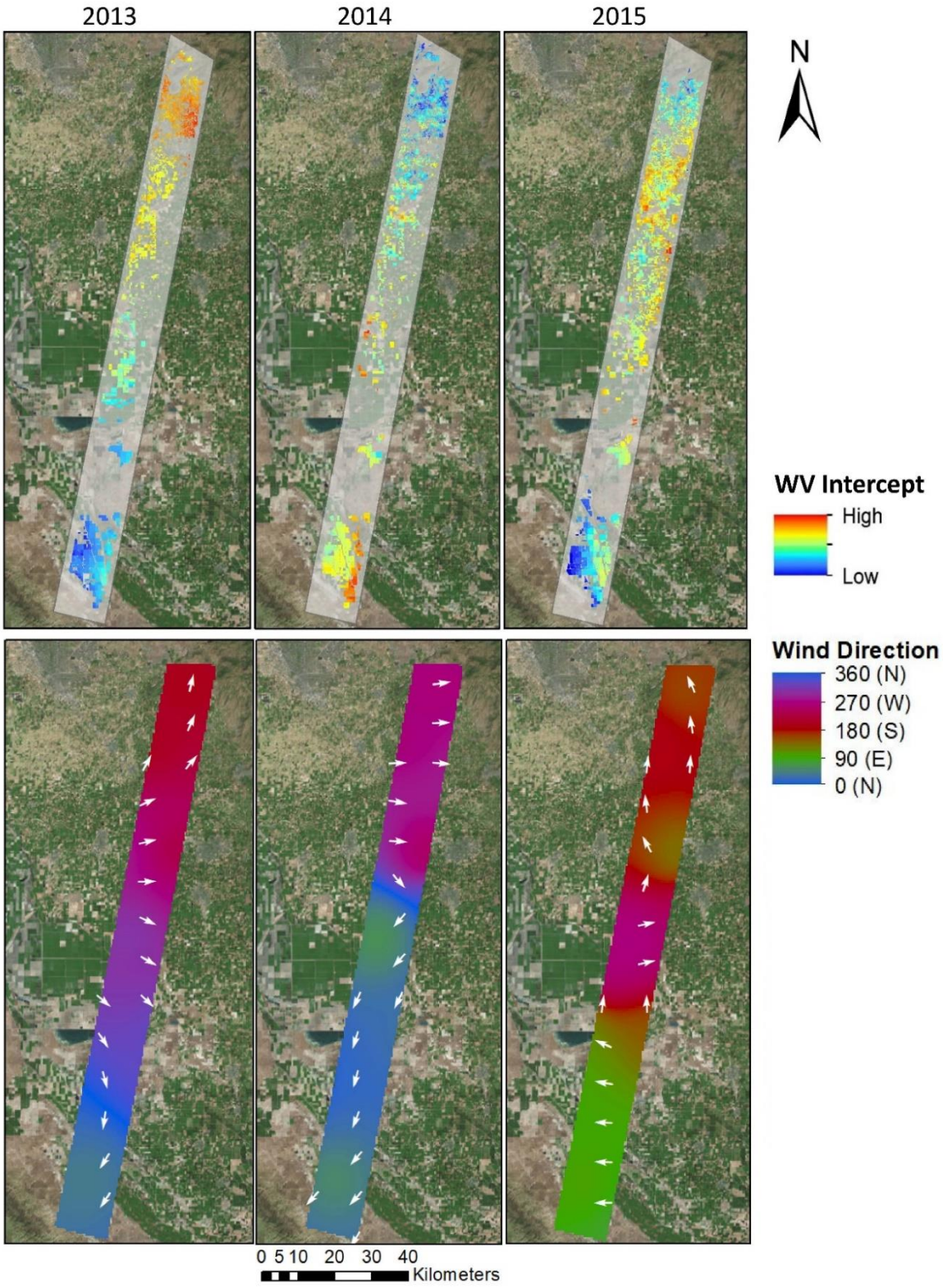

Figure 4.7: Field-level intercepts from water vapor regressions and time-of-flight wind direction maps for each year

4.3.3. Field-level water vapor trends

4.3.3.1. Water vapor patterns as a function of wind

Hypotheses C-F proposed expected relationships between the directionality of water vapor and its slope with both wind magnitude and wind direction. When looking at fields that were predominately covered in green vegetation (GV>0.5), we found patterns that were somewhat consistent with our hypotheses that a moderate wind speed would show higher slopes than very low wind speeds or high wind speeds. Although r-squared values were low, each year showed a significant quadratic relationship between water vapor slope and wind magnitude (Fig 4.8). The 2014 image also had a significant linear trend, but the quadratic relationship showed a higher r-squared. Because wind speeds were lower in 2014, on average, than the other two years, we hypothesize that 2014 would have shown a more definitive quadratic trend if the 2014 scene had more higher windspeed values. These quadratic trends, although accompanied by considerable spread, are in line with our hypotheses.

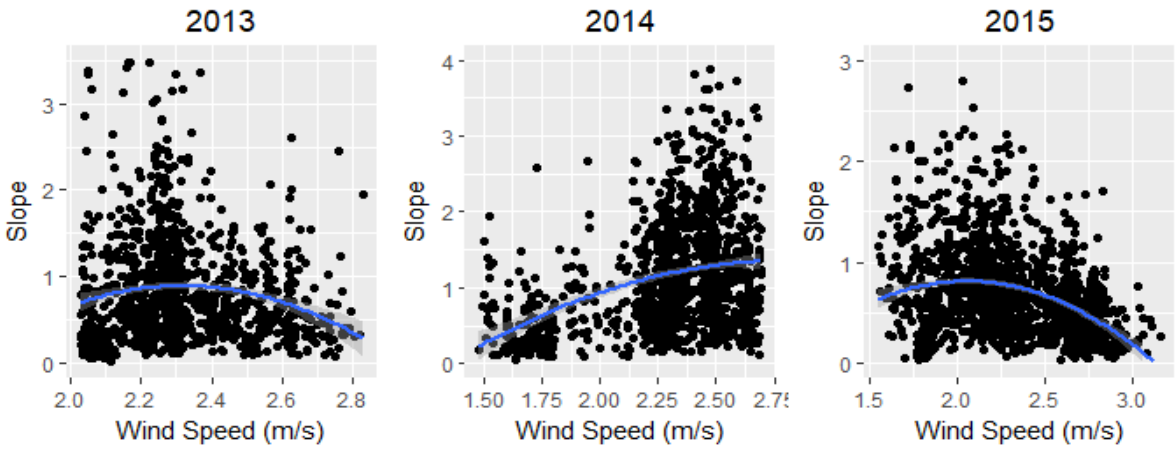

Figure 4.8: Slope of water vapor and the wind speed above the field show significant quadratic relationships in each of the three years (2013:Slope =-10.34+9.83*WS-2.14*WS^2, r^2=0.02, p<0.001, n=1130; 2014:Slope =-3.69+3.57*WS-0.63*WS^2, r^2=0.11, p<0.001, n=1176; 2015:Slope =-2.20+2.96*WS-0.72*WS^2, r^2=0.05, p<0.001, n=1442)

Further, we hypothesized that wind direction and water vapor trajectory would align if fields were actively transpiring. We sub-selected all fields that showed consistent water vapor trajectory and wind directionality. Of 8,128 fields from all three years, 1,138 had significant trends that were within 30° of the wind direction. Of those, 277 were in 2013, 353 in 2014 and 508 in 2015, which accounted for roughly 11%, 15% and 16% of fields in those years respectively. Figure 4.9 highlights two fields from each year that exemplify vapor patterns that were consistent with wind direction, as hypothesized.

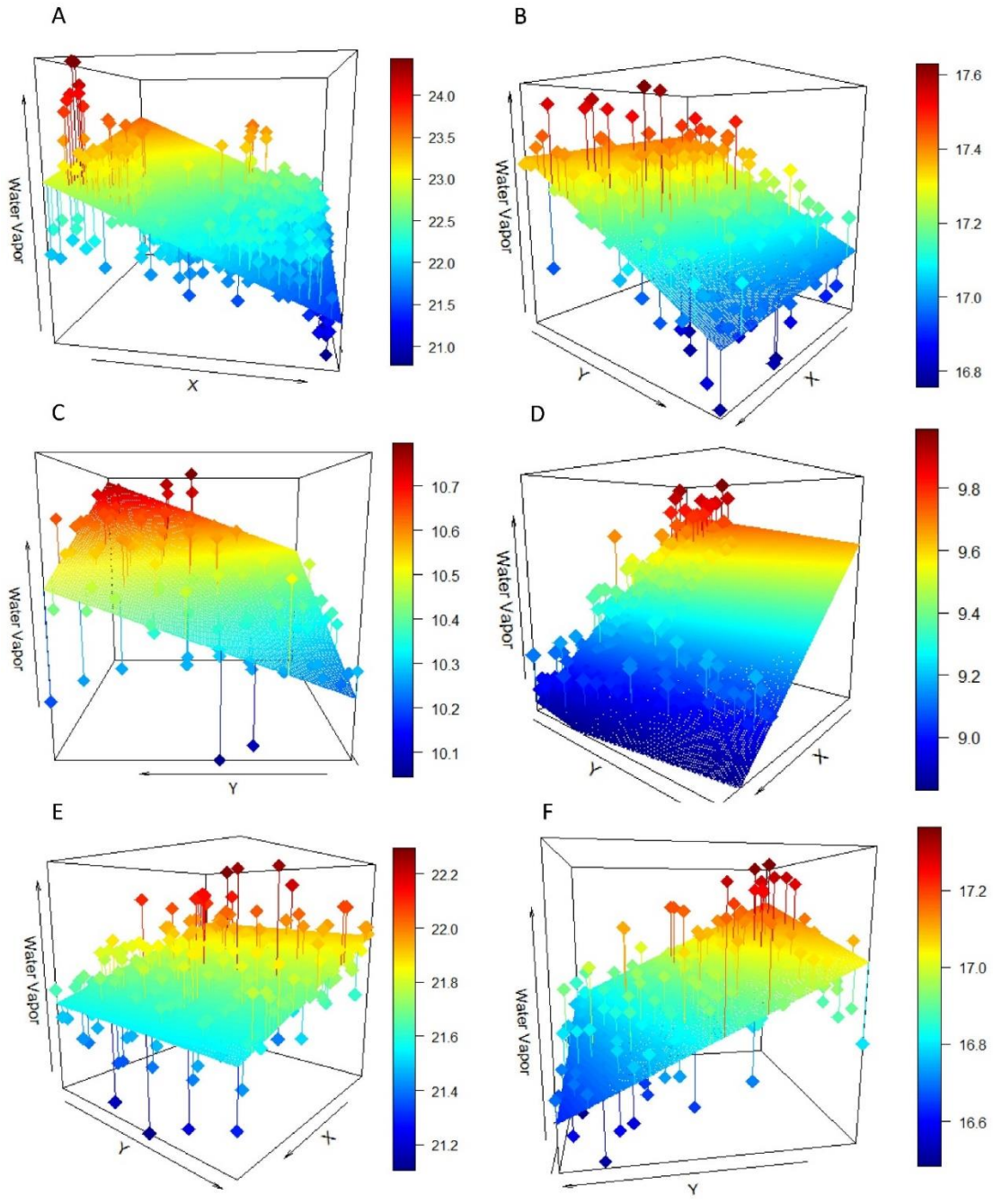

Figure 4.9: Linear surface trends for four fields. A: Corn field from 2013 (slope: 2.45, r^2: 0.54, directional difference: 22°), B: Pistachio field from 2013 (slope: 0.55, r^2: 0.34, directional difference: 5.6°), C: Alfalfa field from 2014 (slope: 2.53, r^2: 0.73, directional difference: 23.0), D: Orange field from 2014 (slope: 1.61, r2: 0.87, directional difference: 1.65) , E: Peach field from 2015 (slope: 1.18, r^2: 0.55, directional difference: 7.3°), F: Mandarin field from 2015 (slope: 1.40, r^2: 0.59, directional difference: 5°)

Analyzing these directionally aligned fields by GV cover and crop type in each year, we found no significant characteristics related to GV when these sub-selected fields were compared to all fields in the study. Examining histograms of GV fraction within the fields that showed directional agreement, no discernable pattern was found. High GV fields were as likely to align in trajectory with wind direction as the low GV fields. In fact, the mean GV of the selected fields were 0.45, 0.46 and 0.43 for the three years, in comparison to 0.47 for the average of all fields in the study. However, segmentation by crop type did show some interesting results. Looking at nine of the most prevalent crops, large differences are seen in the percentage of these crops that showed directional agreement with the wind (Table 4.3). Two-thirds or more of the pistachio and almond fields showed water vapor trends that were in agreement with the wind direction while less than a third of walnut and grape fields did. These differences may be attributable to differences in the crops themselves such as rate of ET or health of the plants, or these differences could be attributable to their position within the study scene as the crops are not evenly disbursed throughout the area.

Table 4.3: The most prevalent crops in the study area and their proportion of fields that had directional differences of less than 30°

Crop	Fields that show agreement with wind direction
Pistachio	76%
Almond	67%
Alfalfa	65%
Orange	48%
Peach	48%
Cherry	40%
Plum	36%
Walnut	32%
Grape	21%

4.3.3.2. Water vapor gradients by field size

Hypothesis G predicted that larger fields would show steeper slopes of vapor than smaller fields because moisture has a larger area over which to build up. We looked at correlations between field size and water vapor slope in each of the three years and found temporally stable results that contradicted our hypothesis. In 2013, 2014, and 2015 water vapor slope and field size showed inverse correlations of -0.35, -0.34, and -0.25 respectively. Smaller fields show steeper slopes than larger fields, generally. Reasons as to why this pattern may exist will be explored in the discussion section.

4.3.3.3. Water vapor gradients and concentrations by GV fraction

We hypothesized that GV fraction would positively correlate with slope and/or intercept, dependent on the wind speed. Fig 4.10 shows the water vapor concentration and GV fraction in the southern portion of the study area where non-cropped area transitions to cropped fields. The figure illustrates that in 2013 and 2015 water vapor concentrations showed a large positive gradient from non-cropped to cropped areas as expected.

Through quantitative evaluation of field-level water vapor trends within the whole study area, we found no correlation in any year between GV fraction and vapor slope ($r = 0.001$ in 2013, $r = -0.02$ in 2014, $r = 0.02$ in 2015) and weak positive correlations between GV fraction and intercept ($r = 0.11$ in 2013, $r = -0.06$ in 2014, $r = 0.26$ in 2015). We hypothesized that the slope/GV correlation would be dependent upon GV fraction as fields that are bare or sparse will show no gradients. Splitting the fields into groups of greater than 50% GV and less than 50% GV, we again found no correlations between GV and vapor slope with all correlation coefficients equaling less than 0.12 and greater than -0.12. Because we found that field size and slope correlated, we further disaggregated fields by field size to study the

GV/slope relationship. Figure 4.11 shows the smallest (less than 0.5 km^2) and largest fields (greater than 0.75 km^2) as example groups of the GV/slope and GV/intercept relationships when split into groups of similar size. No significant trends were found between GV and slope. Small fields from 2014 and 2015 showed significant positive linear relationships between GV and intercept (2014: 9.56 + 0.84*GV, r^2=0.03, p<0.001; 2015: 16.9 + 0.65*GV, r^2=0.04, p<0.001) while the small fields in 2013 and large fields in all three years showed no significant relationship (p>0.05).

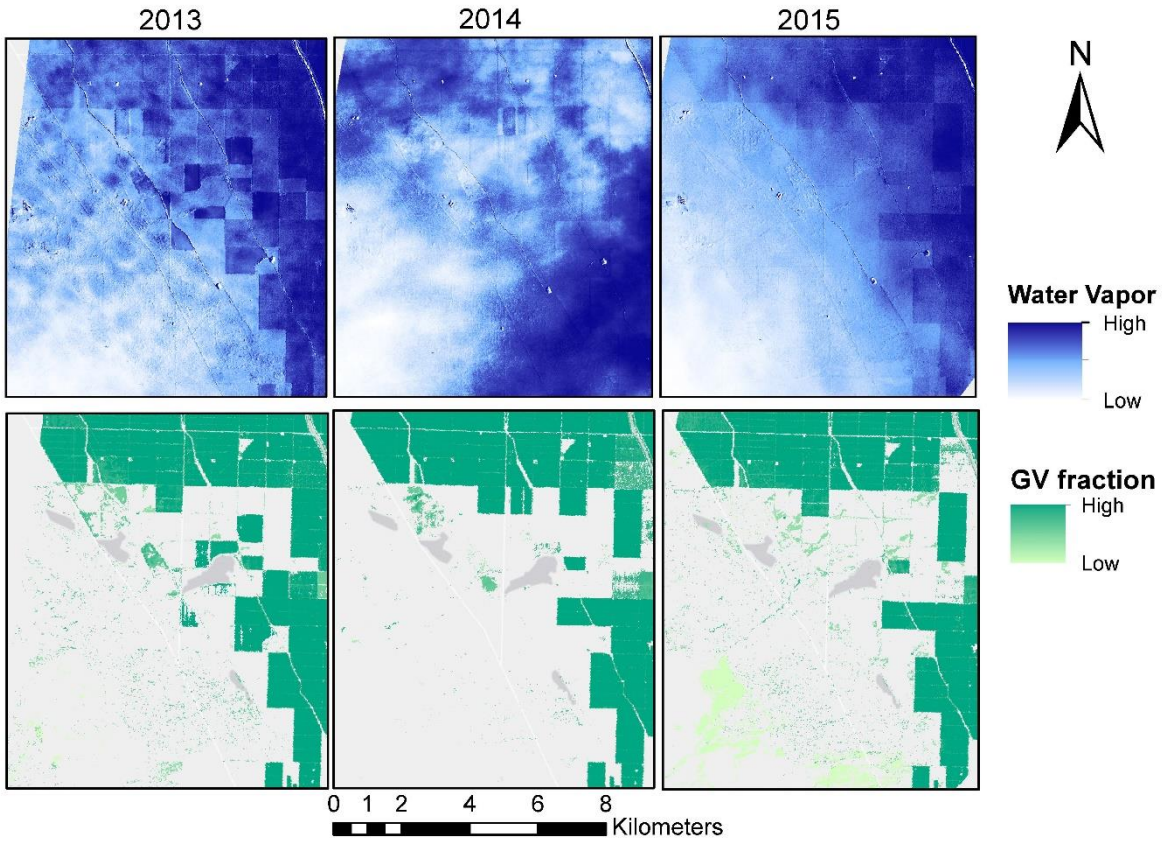

Figure 4.10: Zoomed in section of the southern study area (35.463°, -119.696°) illustrating how water vapor occurs over both cropped and fallow areas. 2013 and 2015 images show greater concentrations of water vapor over cropped than non-cropped areas.

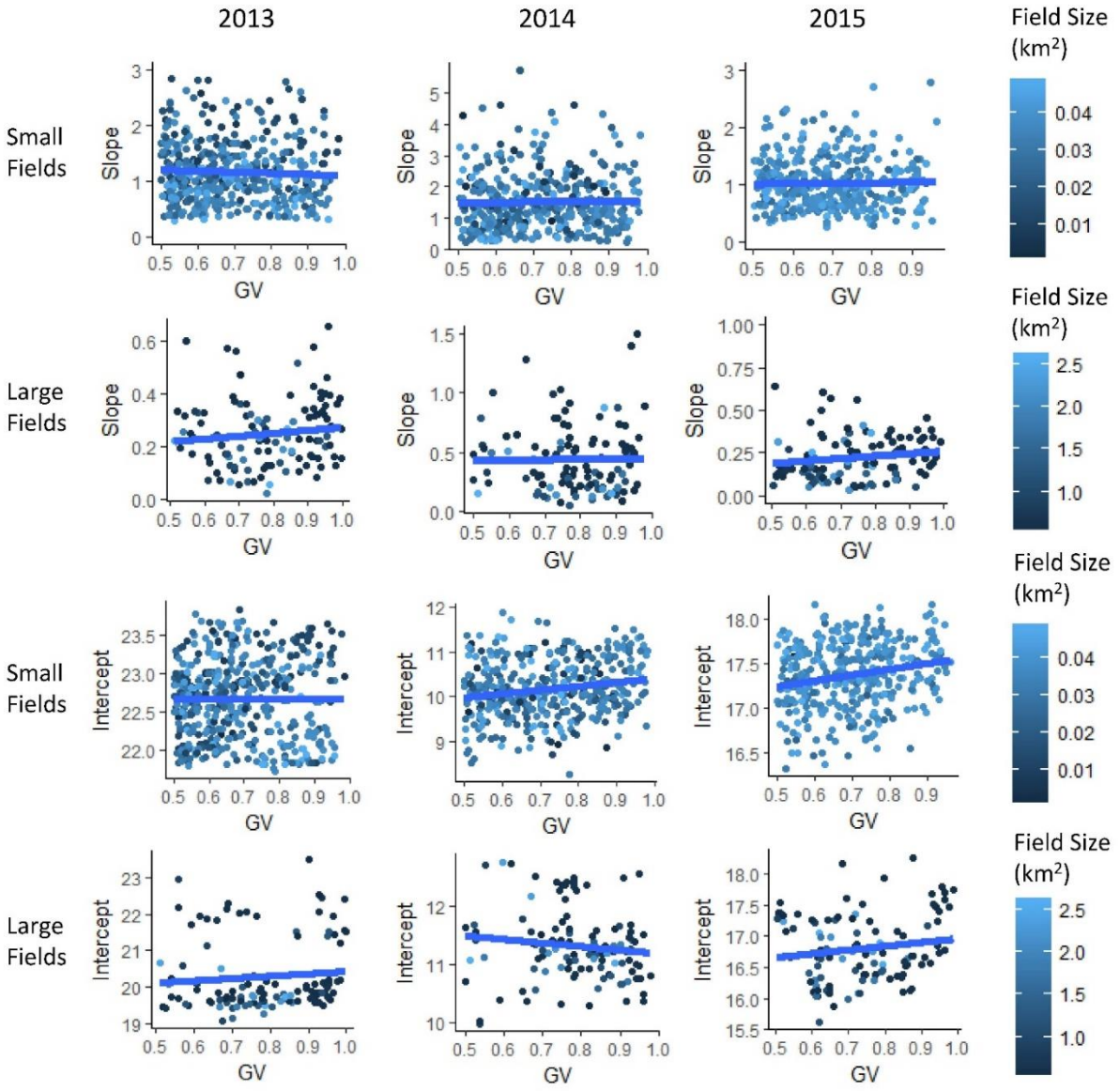

Figure 4.11: Fields from all three years, disaggregated by size, show no relationship between GV fraction and slope of water vapor ($p>0.05$). Small fields from 2014 and 2015 showed significant positive relationships between intercept and GV fraction while small fields in 2013 and all large fields showed no significant relationship ($p>0.05$).

4.3.3.4. Water vapor by crop species

A one-way ANOVA showed that crops do have significantly different slopes of water vapor in every year (2013: [$F(6, 1760) = 33.6$, $p < 0.001$], 2014: [$F(6, 1935) = 26.6$, $p < 0.001$], 2015: [$F(6, 2490) = 39.6$, $p < 0.001$]). We assessed the average slope of each crop type with its expected ET rate, to test Hypothesis K, and expected to find a positive correlation with crops that have high ET rates also having higher slope of water vapor above them. However, we did not find a significant linear trend when plotting ET rate against average slope in any of the three years ($p>0.05$). Given the results of the field size study, we tested the relationship between average slope and average field size and found a significant negative linear relationship in each year (2013: Slope = 0.96 – 0.94*Size, $p<0.001$; 2014: Slope = 1.32– 1.19*Size, $p<0.005$; 2015: Slope = 0.90 – 1.34*Size, $p<0.01$). Fig 4.12 shows 2013 as an example. Therefore, the differences in water vapor slope by crop type, as found by the one-way ANOVA, are likely attributable to the average field size of these crops instead of their ET rate as hypothesized.

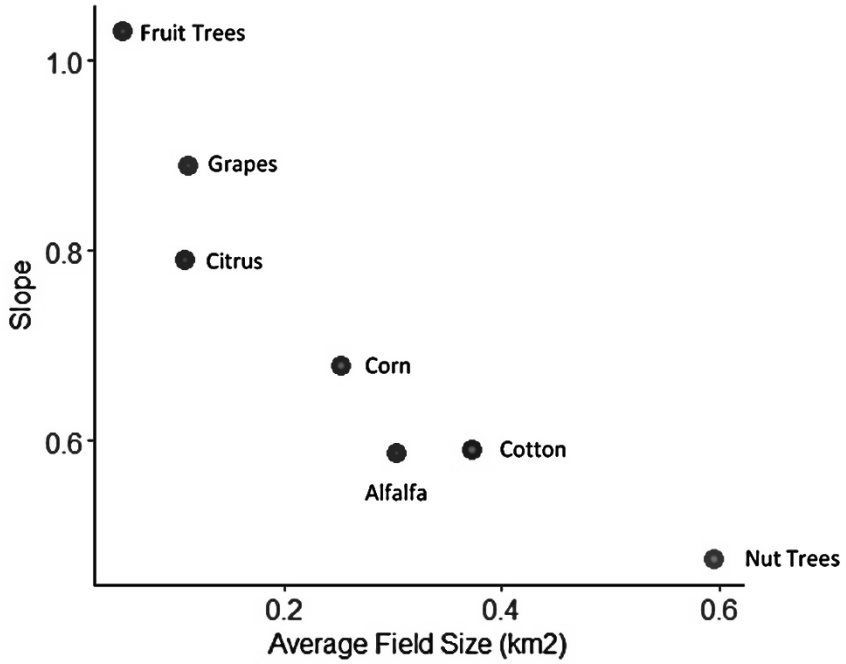

Figure 4.12: Plot showing a negative relationship between water vapor slope and average field size in 2013 for seven crop types prevalent in the study area.

Examining patterns of water vapor over fields within a single crop species, we plotted LST, as an indicator of health, against water vapor slope for fields of alfalfa, almonds, and cherries as three example crops. Results are shown in Figure 4.13. We expected to find a negative relationship between LST and slope as cooler fields are shedding heat via evapotranspiration that may lead to increases of water vapor above a field, detectable through slopes. However, in contrast to Hypothesis J, LST and slope of water vapor actually show a positive correlation that is significant for alfalfa in all three years and almonds in 2014 and 2015 (Fig 4.13). This finding suggests that fields with more healthy, green vegetation have lower slopes, on average, than less vegetated or stressed fields. The reasons for this finding will be explored further in the discussion.

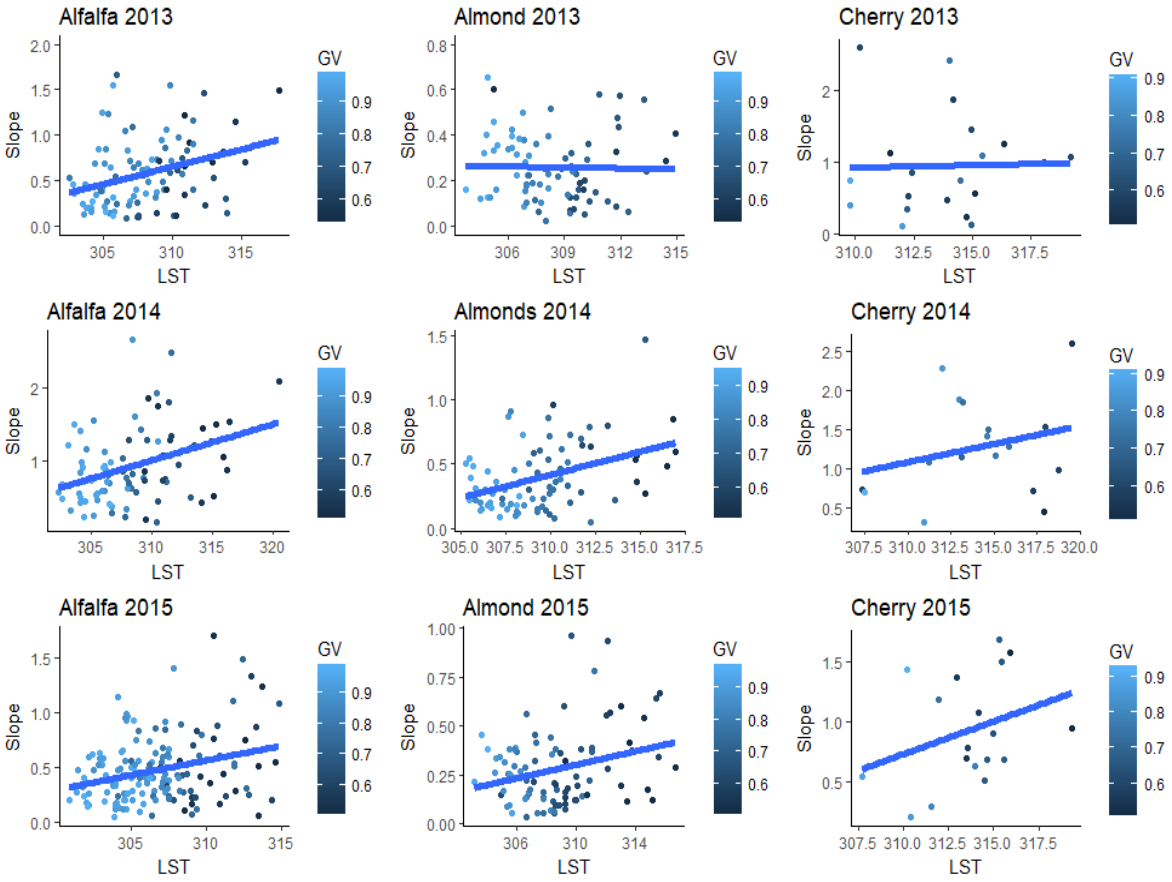

Figure 4.13: Field-level values of water vapor slope and field-level LST for alfalfa, almond, and cherry from 2013, 2014 and 2015. Points are colored by fractional GV coverage. Alfalfa 2013: Slope = -10.0+ 0.03*LST, p=0.013; Almond 2013: Slope = -6.6 + 0.02*LST, p=0.074; Cherry 2013: Slope = -1.1 + 0.007*LST, p=0.914; Alfalfa 2014: Slope = -14.5 + 0.05*LST, p<0.001; Almond 2014: Slope = -10.8 + 0.04*LST, p<0.001; Cherry 2014: Slope = -13.3 + 0.05*LST, p=0.297; Alfalfa 2015: Slope = -7.9 + 0.03*LST, p<0.001; Almond 2015: Slope = -5.0 + 0.02*LST, p=0.008; Cherry 2015: Slope = -16.2 + 0.05*LST, p=0.195.

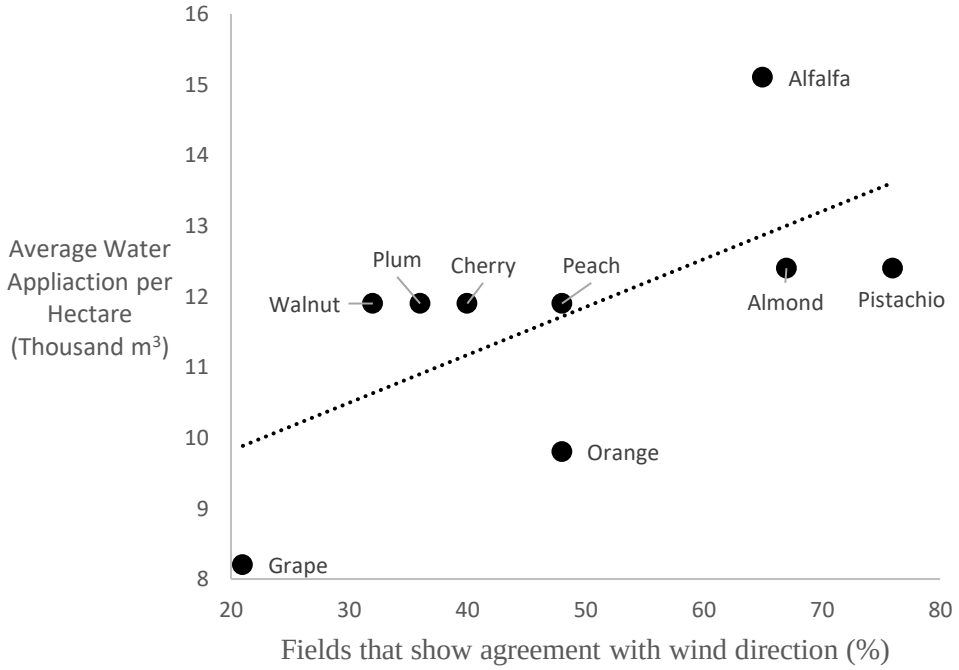

Figure 4.14: A positive correlation is found between crops that require higher water inputs and those that show better agreement between water vapor trends and wind direction ($y = 0.068x + 8.463$)

4.4. Discussion

Water vapor imagery holds information regarding the land surface, the atmosphere, and their interactions, and thus offers a valuable dataset with which to observe and quantify key fluxes between the two. In this study, we expanded upon the work of Ogunjemiyo et al. (2002) by testing several hypotheses to investigate how AVIRIS estimates of water vapor vary with the surface properties and atmospheric conditions in the Central Valley of California. In this section, the key findings will be interpreted, the challenges of this methodology will be discussed, and thoughts on how to move this work forward will be presented.

4.4.1. Interpretation of results

The main findings of the study are summarized in Table 4.4. The results supported that water vapor imagery will show coupling with the land surface at the pixel-level and advection at the scene-scale, under certain atmospheric conditions (Table 4.4 A-B). Further, results supported hypotheses that water vapor gradients will form over fields as a function of wind speed and direction (Table 4.4 C-F). However, hypotheses that field-level ET would be detectable through water vapor slopes were not supported (Table 4.4 G-K).

Table 4.4: Results of the tested hypotheses

	Hypotheses	Result
	Pixel Level	
A	Healthy, transpiring vegetation will have more water vapor above it, as shown through a positive correlation between green vegetation fraction and water vapor concentration and a negative correlation between land surface temperature and water vapor concentration	Conditionally supported
	Scene Level	
B	Water vapor imagery will show advected moisture in the downwind direction	Conditionally Supported
	Field Level	
C	If there are stable and moderate winds, horizontal gradients of water vapor will form above evapotranspiring fields	Supported

D	If winds are light or inconsistent, gradients will not be observed, but water vapor will build up over evapotranspiring fields	Supported
E	High winds will lead to shallower slopes of water vapor gradients above fields	Supported
F	In evapotranspiring fields, wind direction and water vapor trajectory will closely align	Supported
G	Larger fields will show larger water vapor gradients	Not supported
H	The slope of water vapor gradient will positively correlate with green vegetation fraction within vegetated fields	Not supported
I	Bare fields or sparsely vegetated fields will not show water vapor gradients	Not supported
J	Fields that are not evapotranspiring will show no gradients	Not supported
K	Crops that have higher ET rates will have more pronounced (steeper) water vapor gradients above them	Not supported

4.4.1.1. Results in agreement with our hypotheses

At the pixel level, we found results that supported Hypothesis A in two of the three scenes studied. The 2013 and 2015 dates of imagery showed promising correlations to the ground surface below with water vapor increasing with increasing fractions of green, healthy vegetation, while the 2014 imagery did not show any coupling. One hypothesis for this difference is the timing of the flights. While the 2013 and 2015 images were acquired

between 11 AM and noon, the 2014 imagery was flown near 3 PM. This difference in timing suggests that the boundary layer may stay closer to the surface earlier in the day, allowing for greater study of the surface below. Another hypothesis is differences in the atmospheres between those dates such as the air temperature or humidity, which could affect the water vapor over the scene. These differences may also explain why 2014 had significant field-level trends with respect to wind speed and direction while pixel-level correlations with GV were not found. If the 2014 scene shows water vapor that is higher in the air column and more coupled to the wind than to the surface, we would expect to find field-level patterns that act as a function of wind while we would not expect to find surface and water vapor coupling. Our results support this hypothesis.

By calculating field-level water vapor intercepts and evaluating them over the scene, we found evidence that supported Hypothesis B, particularly in the 2013 scene. In that image, small-scale trends of vapor across the study scene showed patterns that were consistent with advection of moisture, as shown in Fig. 4.7. This finding suggests that, as air moves across the Central Valley, crop ET adds vapor to the water column, which builds up in the downwind direction. These results, therefore, show that water vapor imagery could be of use for regional water resource accounting in agricultural areas where water vapor imagery could help quantify latent heat fluxes.

Hypotheses C, D, and E were supported by significant quadratic relationships between wind magnitude and slope that suggest that water vapor slopes only occur when the wind is strong enough to create such trends but weak enough that the water vapor slope is not too shallow. Work by Ogunjemiyo et al. (2002) found their conceptual model held best when winds were at 1.17 to 1.24 m/s. The one case that showed no water vapor patterns was with

an August image with 3.91 m/s winds. The winds in our study were between 1.5 and 3 m/s, in between Ogunjemiyo's values of 1.24 to 3.91 m/s. The quadratic result of our wind speed vs. slope curves suggest that relationships might hold best at intermediate speeds around 2.2-2.5 m/s, and that the wind speed in Ogunjemiyo were lighter than their optimal speed for creating water vapor slopes.

Additionally, some fields showed water vapor trends in line with our hypotheses regarding water vapor trajectory and wind direction, supporting Hypothesis F. As shown in Fig 3.7 of the previous chapter, within pure GV pixels there exists a large range of temperatures that suggest that not all green crop fields are transpiring, possibly due to water shortages mid-summer during a severe drought. Therefore, we hypothesize that fields that show directional agreement between water vapor patterns and wind could be indicative of those fields that were actively transpiring at the time of flight. In agreement with this hypothesis, within those fields that were directionally aligned, we found large variability in the prevalence of crop types. As seen in Table 4.2, two-thirds or more of the alfalfa, almond and pistachios align in trajectory with the wind. Interestingly, these crops are also known for their high water use. Shivers et al. (2018) shows that, in comparison to other deciduous fruits, subtropical fruits or grapes, alfalfa, almonds and pistachios are higher water users. Plotting the percentages in Table 4.2 with the water application values of each crop from Table 2.10 (Shivers et al., 2018), we find a positive correlation (r=0.42; Figure 4.14). This result suggests that high water-using crops show water vapor patterns that align with the wind more frequently, a finding that may be indicative of ET.

4.4.1.2. Results in opposition to our hypotheses

While pixel-level correlations, scene-level advection, and relationships between wind and water vapor were supported by results, we found that Hypotheses G-K were not supported. These hypotheses all emanated from a larger idea that water vapor slope would correlate with ET. We did not find evidence of that. First, we found a temporally-consistent negative relationship between field size and water vapor slope which was in opposition to Hypothesis G. One explanation is that the signal of water vapor movement actually becomes more diffuse and less concentrated over larger fields due to inconsistencies of wind that tend to move the water vapor around and even it out instead of creating gradients. Patterns in smaller fields would be more closely tied to shorter-term wind patterns which would create gradients. Another explanation, suggested by that fact that some crops showed a positive correlation between LST and slope, is that rather than advection of evapotranspired moisture downwind over individual fields, ET causes an accumulation of water vapor over the field. This idea will be explored further in section 4.4.1.3.

Second, we did not find positive correlations between GV fraction and water vapor slope as postulated in Hypotheses H, I and J. If green vegetation transpires and adds to the water vapor above the fields, we expected this addition of water vapor to be quantifiable through the slope above it. We found no correlation between the two, even when results were segmented by field size and GV fraction. We used 50% GV as the cutoff to demarcate sparsely vegetated fields from highly vegetated fields, as is consistent with previous studies (Shivers et al., 2018). However, we found that the average fractional GV coverage of fields that showed good alignment between wind direction and water vapor directionality was

around 45%. Therefore, future studies may want to consider a lower GV threshold or a segmentation of fields into multiple GV classes.

Third, we did not find consistent positive linear relationships between expected crop transpiration rates and water vapor slope as hypothesized in Hypothesis K.

4.4.1.3. New hypotheses

Water vapor patterns were as expected at the field level, in response to wind. However, water vapor patterns were not as expected in response to the surface properties of field size, GV fraction, and ET rate. We had hypothesized that field-level water vapor slopes can be used to infer crop transpiration, but did not find evidence supporting that hypothesis. Rather, our results suggested that water vapor accumulation from transpiration was more dominant than the advection signal at the field level. The rate of ET has been found to stay constant with downwind distance across a field, even if warm, dry air is being advected to a vegetated field (McAneney et al., 1994; Zermeño-Gonzalez & Hipps, 1997). If plants are transpiring at a constant rate and winds are not strong enough or stable enough in directionality to evenly disburse it, the concentration of water vapor above the field would increase relatively evenly throughout the field, leading to a diminished slope. Crops are also more aerodynamically rough than an empty soil field (Chapin et al., 2002), and the resultant turbulence caused by vegetation creates eddies and atmospheric mixing that may muddle signals of field-level advection discernable above smoother landscapes. The hypothesis of water vapor accumulation is supported by results that found a positive relationship between LST and slope for some crops, a negative relationship between field size and slope, and a weak positive correlation between water vapor intercept and GV fraction in 2013 and 2015. Therefore, the results of this study lead us to new conceptual understanding that the

magnitude of water vapor as assessed though the intercept of a fitted plane may be a more accurate indicator of latent heat flux. However, underlying heterogeneity of the landscape and scaling issues, as discussed below, prohibited isolated analyses of intercepts in this study area.

4.4.2. Challenges of water vapor analysis

Observing the link between water vapor and the land surface is complicated by multiple factors that obscure the signal. These include error within the water vapor and wind estimations, the heterogeneity of the landscape, and spatiotemporal issues of scale.

4.4.2.1. Estimation error

There is error within all water vapor estimates regardless of which retrieval method is used, and the estimates vary significantly from model to model (Ben-Dor et al., 2005). However, Ben-Dor et al. found that, of six different water vapor retrievals, ACORN estimated water content with acceptable accuracy and, importantly for our study, it was one of only two models that did not show significant changes in water vapor by vegetation fraction. Therefore, the positive correlations found in years 2013 and 2015 between water vapor and vegetation fraction is assumed to be a product of coupling between the landscape and the atmosphere, rather than an artifact of the retrieval.

There is also error within wind estimates. Wind direction and magnitude can change significantly within a small period of time, making estimations of wind within the study scene at the time of the flight particularly difficult. For example, the Buttonwillow meteorological station registered a wind direction of 353 degrees at 21:28 UTC and 51 degrees ten minutes later at 21:38 UTC on June 3, 2014 when imagery was being captured. With wind directionality that changes frequently, water vapor will not show a uniform trend

in a single direction (Figure 4.15F). Furthermore, with a difference of 100 degrees within ten minutes, estimating wind direction inherently contains a large degree of error. Moreover, with uncertainty as to the accuracy of the wind estimations at the meteorological stations, interpolating from this data to the entire scene will have even a greater degree of error.

4.4.2.2. Land surface interactions

Unlike Ogunjemiyo et al. (2002) who studied water vapor over a relatively homogeneous area of transpiring poplars, this study evaluated water vapor as it varies across a very diverse agricultural landscape with many different crop species, green vegetation cover, and irrigation regimes. As such, Ogunjemiyo's conceptual model (Fig 4.1) illustrated an ideal relationship between water vapor and vegetation at the field-scale that may not hold when introduced in our complex study area. First, interactions between water vapor occurring over two diverse, adjacent fields may alter the vapor deficit and stomatal response of a single crop field and result in water vapor trends that do not hold with Ogunjemiyo's model. The schematic in Figure 4.15A illustrates one possible interaction in which a transpiring field is upwind of a non-transpiring field. While the transpiring field will act as hypothesized with the slope and direction of a fitted plane in line with the wind direction, a plane fitted to the fallow field downwind will likely show a slope that is opposite in direction to the wind. The wind carries moist air from the vegetated field onto the fallow field, leading the upwind edge of the fallow field to have higher water vapor concentrations than the edge that is downwind. In the case of the downwind area being another highly transpiring field (Figure 4.15B), the moist, advected air from the upwind field may reduce the transpiration rate of the downwind field at the boundary by

decreasing the vapor pressure deficit. This may lead to an exaggerated water vapor slope over the downwind field. The accumulation of water vapor from one field can therefore lead to shifts in vegetation response that are difficult to account for. Figure 4.15C illustrates the scenario where a dry, fallow field is upwind of a transpiring field. If the area upwind of a vegetated field is fallow, we would expect the saturation deficit of the dry advecting air to increase the evaporation rate at the boundary unless the vapor pressure deficit is high enough to initialize stomatal closure (Zermeño-Gonzalez & Hipps, 1997). A higher evapotranspiration rate at the upwind side of the field will lessen the expected, observable trend of advection across the field. The transpiration response will be species-dependent.

Second, not all fields will interact with the atmosphere in the same ways, due to differences in aerodynamic roughness, affected by row spacing, plant height, plant size, orientation, and composition. The aerodynamic roughness of a field will influence how effectively and at what height the transpired water vapor will mix with the atmosphere (Chapin et al., 2002). Agricultural fields may differ strongly in aerodynamic roughness, and these differences will lead to deviations from the hypothesized water vapor slope and intercept patterns as they vary with crop type. Therefore, we would not expect all fields to show the same relationships between water vapor, wind, and estimated transpiration rates. We would expect aerodynamically rougher surfaces, such as orchards, to generate greater turbulence, show more mixing between ET and the atmosphere, generate mixing higher up in the atmosphere, and show greater coupling with the wind than row crops (Figure 4.15D). Depending on the wind speed, orchards may show higher or lower slopes than row crops if their vapor patterns are more tied to wind patterns. In contrast, shorter and smoother row crops such as alfalfa will be less coupled to the atmosphere (Figure 4.15E). Because crops

such as orchards are more closely coupled to the atmosphere, they may be more appropriate to study with water vapor imagery.

Therefore, isolating the effects of neighboring fields would be beneficial for field-level water vapor analyses, but this was not logistically possible in our study. The study area is a high-producing agricultural area where most fields are bordered by multiple neighbors of varying GV cover, crop type, size, physical characteristics that influence roughness, and ET rate. Further, without LiDAR data from which physical characteristics such as orientation, height and structure could be obtained, it was not possible to model field-scale differences in aerodynamic roughness in this study. This work has aimed to enhance understanding of the impact of GV fraction, field size, crop type and ET rate on patterns of water vapor, although not enough is yet known to allow for accurate modeling and analysis of all such factors on field level trends in such a diverse landscape.

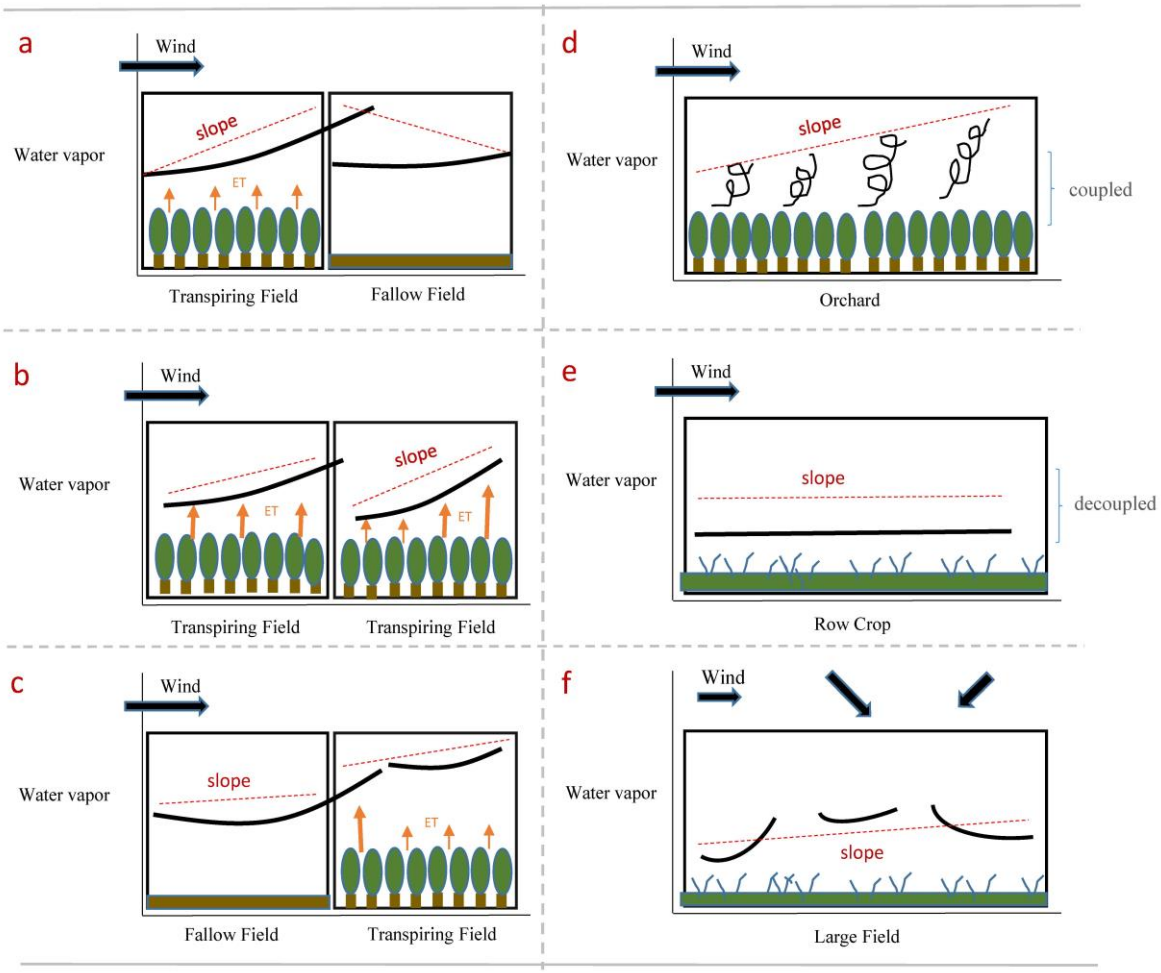

Figure 4.15: Schematic of water vapor over agricultural fields as it is affected by adjacent fields (A,B,C), as it changes with field roughness (D,E) and as it changes with wind heterogeneity (F). Black lines represent water vapor while red dotted lines indicate estimated slopes.

4.4.2.3. Issues of scale

Temporally, snapshots of water vapor and wind at one point in a day do not encompass smaller-scale patterns that are occurring over the entire day, and these snapshots from one moment will not accurately capture wind-vapor interactions. The patterns of water vapor shown in an acquired image will not be created by wind patterns that occur at the time of acquisition. Rather, water vapor will show patterns of advection over a length of time of minutes to hours prior to image acquisition, dependent upon wind speed, ET, boundary

layer depth, turbulence, and other site and scene-specific factors. Therefore, the difference between wind direction and the directionality of a fitted surface of water vapor above a crop field may show large differences when, in actuality, they align with each other. The effect of wind on water vapor at different scales also makes tying an air parcel to the small patch of land at which it originated challenging. In order to determine the time-scale of wind as it relates to water vapor patterns and better be able to account for these effects, a large eddy simulation study would be of value to model water vapor results under a variety of temporal lengths and atmospheric conditions.

Spatially, our results support the assumption that advection is happening at different length scales, but analyses of water vapor at these separate scales is complicated by heterogeneity in the landscape that is not evenly distributed. Many field-level trends are likely obscured by larger synoptic differences in water vapor over the study site because factors of the landscape that are likely to influence water vapor cannot be decoupled from patterns of advection across the scene. Within our study area, both crop species and field sizes are not evenly distributed spatially. Generally, fields in the southern part of the study area are larger and those in the northern part are smaller. Additionally, these larger fields in the south are disproportionately planted with nut crops, while citrus fruits and grapes are more common in the northern, smaller fields. Because water vapor slope is affected by field size, and crop species show large differences in average size, the impact of field size on slope cannot be distinguished from the impact of crop ET on slope. Almond and pistachio trees are high water users, had large fields, but low water vapor slopes. Fruit trees and grapes are lower water users, had small fields, and steep water vapor slopes.

Additionally, the results of this study lead to a new hypothesis that water vapor accumulation on fields may be the dominant process rather than field-level advection, which would cause higher-transpiring crops to have higher water vapor concentration/intercepts. However, this hypothesis could not be tested because scene-scale advection of water vapor obscures potential analyses of water vapor intercept by field size or crop type when the landscape is not evenly distributed. With unequally distributed crops and scene-scale advection, a crop's water vapor intercept will be factor of its position within the scene, and other factors that are expected to influence the intercept, such as ET rates, cannot be studied in isolation. This finding indicates that water vapor analysis in such a diverse and complex agricultural scene, such as the Central Valley, is very scale-dependent as larger scene-level advection confounds analysis of small-scale patterns and vice versa. Future studies that aim to detect ET through water vapor imagery should carefully choose a study site that is of an appropriate scale to measure the type of advection (field, regional) it proposes to detect. In our study area we found trends at the pixel, field and scene scale although these trends muddled analyses at other scales. Future studies might consider a well-mixed study area of an intermediate scale where wind inconsistencies average out.

4.4.3. Opportunities for future work

Water vapor imagery shows patterns of vapor that are highly variable through space and time and that hold valuable information about land-atmosphere interactions. Because few studies have used these data for analyses of vapor patterns, there is considerable room for growth of knowledge in this field.

To further scientific understanding of water vapor imagery analysis, further studies are necessary to refine observation and quantification of land-surface interactions as the signal is highly complex and is affected by many factors. While water vapor imagery could potentially be used to parameterize models of land-surface interactions, additional studies in equally complex landscapes are necessary to define the conditions and scales at which this imagery can be used. Almost 4,000 AVIRIS images have been collected since 2006 and are available for public download. With such a large repository of data collected at different time points, under varied atmospheric conditions, and over diverse surfaces, future research could tease out the conditions under which interactions can best be observed in a more comprehensive way than this study of three snapshots in time could. Further, with future remote sensing missions such as SBG, which will collect hyperspectral imagery at moderate spatial resolutions and enable column water vapor estimates globally, these data streams can be exploited for comparisons of water vapor over large agricultural areas worldwide. These large archives of water vapor observations can also act as a compliment to models that estimate water vapor and plant water use by providing validation data.

In addition to increasing analysis of similarly complex scenes, future studies would benefit from additional data sources that could to isolate the signal of water vapor and validate its link to the surface. Such controls include on-site continuous wind measurements, flux tower measurements of ET, and/or more spatially comprehensive wind data. On-site wind data and ET measurements at a high temporal resolution would both validate trends seen in the water vapor imagery and assist in pinpointing the appropriate temporal scale and time of day for which this analysis is best suited. A mesoscale weather model such as the Weather Research and Forecasting Model (WRF) would also be an asset

to future studies as it could produce a more accurate and spatially comprehensive estimation for wind speeds and directions than interpolation of wind data from weather stations.

Although more work is needed in order to refine understanding of the water vapor signal in a complex agricultural environment, the results suggest that this technique could currently be of use for crop water analyses in agricultural areas that experience less variation in crop type, wind, and field size than the Central Valley of California. The Central Valley proved to be an especially challenging study site as it has a large variety of crops and management practices, which will create non-uniform distributions of aerodynamic roughness, ET rates, and landscape structures throughout the scene. Further, with an average field size that is smaller than average in the United States, the water vapor parcels are more difficult to tie to a source field. Therefore, using this imagery for crop ET estimation would be less challenging in an agricultural area that grows only a few crop types and that has a more consistent and central wind direction. In line with this assumption, we suggest that future studies may consider agricultural sites in North American mid-continental agricultural regions with large fields such as Iowa or Nebraska.

Beyond advancing our ability to capture patterns of field-level ET with water vapor imagery, this imagery may prove valuable for regional analyses of water transport. There are many challenges associated with linking water vapor to crops at the field-level as outlined above, but the idea behind this work will likely hold at a smaller scale. Lo and Famiglietti (2013) found that in the Western United States the irrigation from California has been shown to increase the summer streamflow of the Colorado River by 30 percent. This finding matches with observations of advected moisture in 2013 and 2015 that show

increasing water vapor from west to east from the coast to the Sierra Nevada Mountains. These large movements of water vapor have implications for climate change and land use, and call upon the need to increase monitoring of water vapor patterns in areas with large irrigation inputs. Therefore, a study that examines the ability of water vapor imagery to assist in regional water transport assessments could be of high value.

4.5. Conclusion

This paper analyzed water vapor as it varies spatially in three different years over an agricultural landscape and found that the methodology shows promising correlations between water vapor and the surface at the pixel, field, and scene scales. Our results showed coupling with the land surface at the pixel level, advection at the scene scale, water vapor gradients over fields as a function of wind speed and direction, and correlations between water vapor and surface properties that support accumulation of water vapor over advection at the field-scale. This work demonstrates the potential for water vapor retrievals to provide multi-scale information on water in a complex agricultural region; however, further elaboration of the methodology will be necessary to identify ideal conditions and scales for such analyses, as well as to quantify errors.

Chapter 5: Conclusions

The goal of this research was to test the capabilities of a combined hyperspectral and thermal dataset for study of agriculture in the Central Valley as it changes with drought. The work of this dissertation examines the opportunities and challenges of mapping crops and monitoring their change with time, using crop temperatures to pinpoint stress within and between fields, and using water vapor imagery to increase understanding of hydrological processes on the ground. In the following paragraphs, I will review the key findings of this work and then suggest future directions and potential applications of this research.

In Chapter 2, I examined crop classification accuracy and used resultant products to study crop change over time. Results showed high overall accuracies of 94.4% at the field level when classifying crops with AVIRIS. This classification was more accurate than comparable classifications run with Landsat OLI and Sentinel at 90.4% and 91.7%. The higher accuracy indicates that the additional bands and finer spectral resolution of hyperspectral imagery confers added benefits for crop classification. Crop maps produced using the random forest classifier indicated that the crops were fallowed with greater frequency as the drought persisted from 2013 to 2015. Changes in area by crop type revealed that decisions regarding which crop to plant in times of drought were not driven by crop water use, but were more likely a factor of crop value and/or crop permanence.

In Chapter 3, I investigated thermal variability within agricultural orchards and proposed a new method of evaluating crop stress without the need for ancillary meteorological variables. MASTER imagery showed that within orchards, there exist multiple distinct thermal classes of GV, NPV, and soil. Hyperspectral AVIRIS imagery can

be used to capture a degree of this variability for more refined modeling of expected pixel temperatures. This study found crop temperatures that correlate to expected crop ET rates and soil temperatures that show linkages to soil moisture. These findings highlight the need for identification of thermal subclasses within GV, NPV, and soil for stress analyses. With variability due to fractional cover, type of vegetation, moisture, and structure stripped away, our approach calculated temperature residuals that showed correlations to changes in crop yields during the study period. Further assessment of findings revealed an increase in temperature residuals during the study period that is consistent with increasing stress, likely linked to the progression of drought.

In Chapter 4, I found results that furthered our understanding of the challenges and potential opportunities to use water vapor imagery in future analyses of land-atmosphere interactions. While pixel-level correlations, scene-level advection, and relationships between wind and water vapor were supported by results, relationships between water vapor and surface properties of field size, GV fraction, and ET rate were not supported. I found evidence of water vapor advection across the study area. Crops with higher average water application rates show more directional agreement between water vapor slope and wind direction. I also found expected quadratic relationships between wind magnitude and slope. However, hypotheses that GV fraction of a field would correlate positively to its slope and that crops would have higher slopes over cooler fields were both unsupported by the results. Analysis helped to refine understanding of the drivers of water vapor patterns and its utility for agricultural applications.

One of the primary goals of this dissertation was to test sensor capabilities, such as will be included in the future space borne NASA SBG (previously HyspIRI) Mission, for

agricultural drought analyses. Results show that the SBG Mission will enhance our ability to monitor agriculture in water-limited regions. Hyperspectral imagery can improve accuracy of crop mapping over multispectral sensors and can enable classifications at one time point with one image. This type of imagery could be well suited for monitoring diverse and dynamic agricultural landscapes where yearly crop maps are not sufficient for crop accounting and water resource needs. Further, with the addition of thermal imagery, SBG will be able to not only map crops, but also assess the well-being of those crops. Land surface temperature has been shown to be a fairly accurate predictor of water stress at the regional level, when thermal variability can be accounted for. The hyperspectral imagery provides information about the surface properties that allow for thermal stress to be evaluated. Moreover, the types and health of crops can be studied in conjunction with the atmospheric water vapor above them as hyperspectral imagery contains refined information about water vapor absorptions that most Earth-observing satellites avoid. This allows for evaluation of land-atmosphere interactions over a large spatial area. While such work continues to require more attention and is not understood enough to be applied or operational, the scientific assumptions hold promise.

Beyond sensor capabilities, this work also commented on California's agriculture and its change with drought. The crop planting analysis and health evaluation show results that are somewhat counterintuitive. Chapter 2 showed that farmers are planting more perennial crops than annual crops, likely because they are more lucrative. Chapter 3 showed that crops that are not well-suited for drought, such as walnuts, actually do well during drought as farmers shift resources to the most vulnerable and economically-important crops. These results are really important given that droughts are likely to become more severe and

frequent with time. If farmers continue to respond to environmental limitations with economic incentives, what will the future of California agriculture look like? This research surmises that such a landscape will be made up of an increasingly large percentage of high-value fruit and nut crops. As these crops are not only economically valuable but water intensive, short-term droughts may be driving management choices that will lead to further vulnerability within the sector.

With the SBG Mission recommended by the 2018 Decadal Survey, we will obtain a hyperspectral and temporal dataset that is more expansive in spatial scope, temporally richer, and more streamlined in its operational products. The expansion in spatial scope will allow crop mapping and crop health analyses on a global scale. Given the results of this dissertation, SBG will be most valuable to agricultural areas that see a high diversity of crops, have dynamic plantings, and/or are in need to accurate and timely resource accounting. Besides California, SBG could be of value in China, India, or Brazil given their high agricultural production. With the finer temporal resolution, methods used in this work will be able to be applied with enhanced frequency for refined understanding of plant water use. The time scale at which plants experience water stress is much finer than the yearly time scales that were examined in this dissertation. Rather than looking at one point in a year, SBG will allow researchers to monitor crop health at the field-scale multiple times within a month. With this information, such analyses may be able to be operationalized so that stressed fields can be pinpointed and assisted prior to yield losses. Finally, the shift from the HyspIRI test campaign to the SBG mission means a move from an aerial to a satellite platform, which will allow for streamlining of data products. Working with the aerial HyspIRI dataset was cumbersome in that the products required a lot of pre-

processing, products were not entirely consistent between dates, and the timing of the flights varied with each acquisition. With consistent products from the SBG mission, multi-temporal analyses can be more easily conducted that will allow for the change in agriculture across seasons and multi-annual time steps.

To move this work forward, future studies should investigate the potential for operational crop mapping in California, study the viability of the proposed thermal method for routine analysis of plant health in places other than California orchards, and continue to study the potential of water vapor imagery in a more controlled study setting. First, to make a crop classification operational and useful to managers who needs to monitor food and water resources, the methodology needs to be portable between dates and scenes. While Chapter 2 showed that results of our classification were not very portable, such a study would need to be replicated with more consistent satellite imagery and a spectral library composed of crops at many different growth stages to better understand its limitations for routine monitoring. Second, future work should examine the viability of the thermal method proposed in Chapter 3 to differentiate crop stress in other regions besides California and in other types of vegetation besides managed orchards. Without the need for ancilliary inputs, the method shows potential for operational evaluation of plant health. However, such studies that expand and assess the method spatially and temporal need to be conducted. Results could be compared or enhanced by high-resolution diurnal thermal data from ECOSTRESS. Finally, the water vapor imagery analysis is only in its infancy and, because little research has been done in the area, can be expanded in many ways. As suggested in Chapter 4, future work would benefit from hypothesis testing of surface and land interactions in an area such as the mid-Western United States that has less crop variability

and more uniform winds, a smaller and more controlled study site, or with the aid of refined weather models such as WRF.

As the climate changes, understanding its impacts to our food and water resources will be of critical importance. This dissertation furthered scientific and societal ability to aid in this need by evaluating ways in which remote sensing data can be used to inform management and policy decisions in the years to come.

References

Adams, J.B., Smith, M.O., Gillespie, A.R., 1993. Imaging spectroscopy: Interpretation based on spectral mixture analysis., in: Remote Geochemical Analysis: Elemental and Mineralogical Composition. https://doi.org/10.1109/IEMBS.1997.757820

Adams, R.M., Rosenzweig, C., Peart, R.M., Ritchie, J.T., McCarl, B.A., Glyer, J.D., Curry, R.B., Jones, J.W., Boote, K. J., Hartwell Allen, L., 1990. Global climate change and US agriculture. Nature. https://doi.org/10.1016/0021-9797(80)90501-9

AghaKouchak, A., Cheng, L., Mazdiyasni, O., Farahmand, A., 2014. Global warming and changes in risk of concurrent climate extremes: Insights from the 2014 California drought. Geophys. Res. Lett. https://doi.org/10.1002/2014GL062308

AghaKouchak, A., Feldman, D., Hoerling, M., Huxman, T., Lund, J., 2015. Water and climate: Recognize anthropogenic drought. Nature. https://doi.org/10.1038/524409a

Alcantara, C., Kuemmerle, T., Prishchepov, A. V., Radeloff, V.C., 2012. Mapping abandoned agriculture with multi-temporal MODIS satellite data. Remote Sens. Environ. https://doi.org/10.1016/j.rse.2012.05.019

Alchanatis, V., Cohen, Y., Cohen, S., Moller, M., Sprinstin, M., Meron, M., Tsipris, J., Saranga, Y., Sela, E., 2010. Evaluation of different approaches for estimating and mapping crop water status in cotton with thermal imaging. Precis. Agric. 11, 27–41. https://doi.org/10.1007/s11119-009-9111-7

Alderfasi, A.A., Nielsen, D.C., 2001. Use of crop water stress index for monitoring water status and scheduling irrigation in wheat. Agric. Water Manag. https://doi.org/10.1016/S0378-3774(00)00096-2

Allen, R.G., Pereira, L.S., Raes, D., Smith, M., 1998. FAO Irrigation and Drainage Paper, FAO. https://doi.org/10.1016/j.eja.2010.12.001

Allen, R.G., Tasumi, M., Trezza, R., 2007. Satellite-Based Energy Balance for Mapping Evapotranspiration with Internalized Calibration (METRIC)—Model. J. Irrig. Drain. Eng. 133, 380–394. https://doi.org/10.1061/(ASCE)0733-9437(2007)133:4(380)

Anderson, M.C., Allen, R.G., Morse, A., Kustas, W.P., 2012. Use of Landsat thermal imagery in monitoring evapotranspiration and managing water resources. Remote Sens. Environ. 122, 50–65. https://doi.org/10.1016/j.rse.2011.08.025

Anderson, M.C., Hain, C., Wardlow, B., Pimstein, A., Mecikalski, J.R., Kustas, W.P., 2011. Evaluation of Drought Indices Based on Thermal Remote Sensing of Evapotranspiration over the Continental United States. J. Clim. 24, 2025–2044. https://doi.org/10.1175/2010JCLI3812.1

Anderson, M.C., Norman, J.M., Diak, G.R., Kustas, W.P., Mecikalski, J.R., 1997. A two-source time-integrated model for estimating surface fluxes using thermal infrared remote sensing. Remote Sens. Environ. https://doi.org/10.1016/S0034-4257(96)00215-5

Anderson, M.C., Norman, J.M., Mecikalski, J.R., Otkin, J. a., Kustas, W.P., 2007. A climatological study of evapotranspiration and moisture stress across the continental United States based on thermal remote sensing: 2. Surface moisture climatology. J. Geophys. Res. Atmos. 112, 1–13. https://doi.org/10.1029/2006JD007507

Anderson, M.C., Norman, J.M., Mecikalski, J.R., Otkin, J. a., Kustas, W.P., 2007. A climatological study of evapotranspiration and moisture stress across the continental United States based on thermal remote sensing: 1. Model formulation. J. Geophys. Res. Atmos. 112. https://doi.org/10.1029/2006JD007506

Anderson, M.C., Zolin, C.A., Sentelhas, P.C., Hain, C.R., Semmens, K., Tugrul Yilmaz, M., Gao, F., Otkin, J.A., Tetrault, R., 2016. The Evaporative Stress Index as an indicator of agricultural drought in Brazil: An assessment based on crop yield impacts. Remote Sens. Environ. https://doi.org/10.1016/j.rse.2015.11.034

Asbjornsen, H., Goldsmith, G.R., Alvarado-Barrientos, M.S., Rebel, K., Van Osch, F.P., Rietkerk, M., Chen, J., Gotsch, S., Tobón, C., Geissert, D.R., Gómez-Tagle, A., Vache, K., Dawson, T.E., 2011. Ecohydrological advances and applications in plant-water relations research: A review. J. Plant Ecol. https://doi.org/10.1093/jpe/rtr005

Bandos, T.V., Bruzzone, L., Camps-Valls, G., 2009. Classification of Hyperspectral Images With Regularized Linear Discriminant Analysis. IEEE Trans. Geosci. Remote Sens. 47, 862–873. https://doi.org/10.1109/TGRS.2008.2005729

Barcza, Z., Kern, A., Haszpra, L., Kljun, N., 2009. Spatial representativeness of tall tower eddy covariance measurements using remote sensing and footprint analysis. Agric. For. Meteorol. https://doi.org/10.1016/j.agrformet.2008.10.021

Barnett, T., Malone, R., Pennell, W., Stammer, D., Semtner, B., Washington, W., 2004. The effects of climate change on water resources in the west: Introduction and overview. Clim. Change. https://doi.org/10.1023/B:CLIM.0000013695.21726.b8

Bellvert, J., Zarco-Tejada, P.J., Girona, J., Fereres, E., 2014. Mapping crop water stress index in a 'Pinot-noir' vineyard: comparing ground measurements with thermal remote sensing imagery from an unmanned aerial vehicle. Precis. Agric. 15, 361–376. https://doi.org/10.1007/s11119-013-9334-5

Ben-Gal, A., Agam, N., Alchanatis, V., Cohen, Y., Yermiyahu, U., Zipori, I., Presnov, E., Sprintsin, M., Dag, A., 2009. Evaluating water stress in irrigated olives: correlation of soil water status, tree water status, and thermal imagery. Irrig. Sci. 27, 367–376. https://doi.org/10.1007/s00271-009-0150-7

Berk, A., Conforti, P., Kennett, R., Perkins, T., Hawes, F., Van Den Bosch, J., 2017. MODTRAN® 6: A major upgrade of the MODTRAN® radiative transfer code, in: Workshop on Hyperspectral Image and Signal Processing, Evolution in Remote Sensing. https://doi.org/10.1109/WHISPERS.2014.8077573

Berni, J.A.J., Zarco-Tejada, P.J., Sepulcre-Cantó, G., Fereres, E., Villalobos, F., 2009. Mapping canopy conductance and CWSI in olive orchards using high resolution thermal remote sensing imagery. Remote Sens. Environ. 113, 2380–2388. https://doi.org/10.1016/J.RSE.2009.06.018

Bhuiyan, C., Singh, R.P., Kogan, F.N., 2006. Monitoring drought dynamics in the Aravalli region (India) using different indices based on ground and remote sensing data. Int. J. Appl. Earth Obs. Geoinf. https://doi.org/10.1016/j.jag.2006.03.002

Bonan, G.B., 2008. Ecological Climatology: Concepts and Applications, 2nd edition, Cambridge University Press. https://doi.org/10.1111/j.1745-5871.2009.00640.x

Borel, C.C., Gerstl, S.A.W., 1994. Nonlinear spectral mixing models for vegetative and soil surfaces. Remote Sens. Environ. https://doi.org/10.1016/0034-4257(94)90107-4

Breiman, L., 2001. Random Forests. Mach. Learn. https://doi.org/10.1023/A:1010933404324

California Department of Food & Agriculture (CDFA), 2018. California Agricultural Statistics Review 2017-18. https://www.cdfa.ca.gov/statistics/PDFs/2017-18AgReport.pdf (accessed 29 January 2019)

California Department of Food & Agriculture (CDFA), 2016. California Agricultural Statistics Review 2015-16. https://www.cdfa.ca.gov/statistics/PDFs/2016Report.pdf (accessed 18 October 2018)

California Department of Food and Agriculture (CDFA), 2015. California Agricultural Statistics Review 2014–2015. https://www.cdfa.ca.gov/statistics/PDFs/2015Report.pdf (accessed on 10 July 2018).

California Department of Water Resources (CA DWR), 2018. Agricultural Water Use. http://www.water.ca.gov/wateruseefficiency/agricultural (accessed 29 January 2019)

California Department of Water Resources (CA DWR), 2017. Drought Information. http://www.water.ca.gov/waterconditions/ (accessed 20 May 2017)

California Department of Water Resources (CA DWR), 2009. California Water Plan. Update 2009. *Volume 3, Regional Reports*. *Bulletin 160–09*, Sacramento, CA, USA.

Camps-Valls, G., Gómez-Chova, L., Calpe-Maravilla, J., Soria-Olivas, E., Martín-Guerrero, J.D., Moreno, J., 2003. Support vector machines for crop classification using hyperspectral data, in: Iberian Conference on Pattern Recognition and Image Analysis. https://doi.org/10.1007/978-3-540-44871-6_16

Carle, D., 2004. *Introduction to Water in California*; University of California Press: Los Angeles, CA, USA.

Carlson, T.N., Gillies, R.R., Perry, E.M., 1994. A method to make use of thermal infrared temperature and NDVI measurements to infer surface soil water content and fractional vegetation cover. Remote Sens. Rev. https://doi.org/10.1080/02757259409532220

Carrère, V., Conel, J.E., 1993. Recovery of atmospheric water vapor total column abundance from imaging spectrometer data around 940 nm - sensitivity analysis and application to Airborne Visible/Infrared Imaging Spectrometer (AVIRIS) data. Remote Sens. Environ. https://doi.org/10.1016/0034-4257(93)90015-P

Cayan, D.R., Kammerdiener, S.A., Dettinger, M.D., Caprio, J.M., Peterson, D.H., 2001. Changes in the Onset of Spring in the Western United States. Bull. Am. Meteorol. Soc. https://doi.org/10.1175/1520-0477(2001)082<0399:CITOOS>2.3.CO;2

California Cotton Ginners and Growers Association (CCGGA). California Cotton Information. Available online: https://ccgga.org/cotton-information (accessed on 10 July 2018).

Challinor, A.J., Watson, J., Lobell, D.B., Howden, S.M., Smith, D.R., Chhetri, N., 2014. A meta-analysis of crop yield under climate change and adaptation. Nat. Clim. Chang. https://doi.org/10.1038/nclimate2153

Chang, J., Hansen, M.C., Pittman, K., Carroll, M., DiMiceli, C., 2007. Corn and soybean mapping in the United States using MODIS time-series data sets. Agron. J. https://doi.org/10.2134/agronj2007.0170

Chapin III, F. S., Matson, P. A., & Mooney, H. A., 2002. Principles of terrestrial ecosystem ecology–Springer-Verlag. *New York, USA*, 298-300.

Christian-Smith, J., Levy, M.C., Gleick, P.H., 2015. Maladaptation to drought: a case report from California, USA. Sustain. Sci. https://doi.org/10.1007/s11625-014-0269-1

Clark, M.L., 2017. Comparison of simulated hyperspectral HyspIRI and multispectral Landsat 8 and Sentinel-2 imagery for multi-seasonal, regional land-cover mapping. Remote Sens. Environ. https://doi.org/10.1016/j.rse.2017.08.028

Clark, M.L., Roberts, D.A., 2012. Species-level differences in hyperspectral metrics among tropical rainforest trees as determined by a tree-based classifier. Remote Sens. https://doi.org/10.3390/rs4061820

Cooley, H., Donnelly, K., Phurisamban, R., Subramanian, M., 2015. Impacts of California ' s Ongoing Drought: Agriculture. Pacific Inst.

Craig, M.E., 2001. The NASS cropland data layer program. In *Third International Conference on Geospatial Information in Agriculture and Forestry, Denver, Colorado* (pp. 5-7).

Diffenbaugh, N.S., Swain, D.L., Touma, D., 2015. Anthropogenic warming has increased drought risk in California. Proc. Natl. Acad. Sci. https://doi.org/10.1073/pnas.1422385112

Dirks, K.N., Hay, J.E., Stow, C.D., Harris, D., 1998. High-resolution studies of rainfall on Norfolk Island: Part II: Interpolation of rainfall data. J. Hydrol. 208, 187–193. https://doi.org/10.1016/S0022-1694(98)00155-3

Dubayah, R., Rich, P., 1995. Topographic solar radiation models for GIS. Int. J. Geogr. Inf. Sci. 9, 405–419. https://doi.org/10.1080/02693799508902046

Dudley, K.L., Dennison, P.E., Roth, K.L., Roberts, D.A., Coates, A.R., 2015. A multi-temporal spectral library approach for mapping vegetation species across spatial and temporal phenological gradients. Remote Sens. Environ. https://doi.org/10.1016/j.rse.2015.05.004

Faunt, C.C., 2009. Groundwater Availability of the Central Valley Aquifer, California. U.S. Geol. Surv. https://doi.org/10.1017/CBO9781107415324.004

Fisher, J.B., Hook, S.J., Allen, R.G., Anderson, M.C., French, A.N., Hain, C., Hulley, G.C. Wood, E.F., 2015. ECOSTRESS: NASA's next-generation mission to measure evapotranspiration from the International Space Station. In AGU Fall Meeting Abstracts.

Foody, G.M., Cox, D.P., 1994. Sub-pixel land cover composition estimation using a linear mixture model and fuzzy membership functions. Int. J. Remote Sens. https://doi.org/10.1080/01431169408954100

Foody, G.M., 2002. Status of land cover classification accuracy assessment. Remote Sens. Environ. https://doi.org/10.1016/S0034-4257(01)00295-4

Foody, G.M., Mathur, A., 2006. The use of small training sets containing mixed pixels for accurate hard image classification: Training on mixed spectral responses for classification by a SVM. Remote Sens. Environ. https://doi.org/10.1016/j.rse.2006.04.001

Fresno County Agricultural Commissioner, 2018. Crop Report History. https://www.co.fresno.ca.us/departments/agricultural-commissioner/crop-report-history (accessed 18 October 2018).

Gaffen, D.J., Elliott, W.P., Robock, A., 1992. Relationships between tropospheric water vapor and surface temperature as observed by radiosondes. Geophys. Res. Lett. https://doi.org/10.1029/92GL02001

Galvão, L.S., Epiphanio, J.C.N., Breunig., F.M., Formaggio, A.R., 2011. Crop Type Discrimination Using Hyperspectral Data. Hyperspectral Remote Sens. Veg. https://doi.org/doi:10.1201/b11222-25

Galvão, L.S., Formaggio, A.R., Tisot, D.A., 2005. Discrimination of sugarcane varieties in Southeastern Brazil with EO-1 Hyperion data. Remote Sens. Environ. 94, 523–534. https://doi.org/10.1016/j.rse.2004.11.012

Galvão, L.S., Roberts, D.A., Formaggio, A.R., Numata, I., Breunig, F.M., 2009. View angle effects on the discrimination of soybean varieties and on the relationships between vegetation indices and yield using off-nadir Hyperion data. Remote Sens. Environ. https://doi.org/10.1016/j.rse.2008.12.010

Gao, B.C., Goetzt, A.F.H., 1995. Retrieval of equivalent water thickness and information related to biochemical components of vegetation canopies from AVIRIS data. Remote Sens. Environ. https://doi.org/10.1016/0034-4257(95)00039-4

Gao, B.-C., Goetz, A.F.H., 1990. Column atmospheric water vapor and vegetation liquid water retrievals from Airborne Imaging Spectrometer data. J. Geophys. Res. https://doi.org/10.1029/JD095iD04p03549

Gislason, P.O., Benediktsson, J.A., Sveinsson, J.R., 2006. Random forests for land cover classification, in: Pattern Recognition Letters. https://doi.org/10.1016/j.patrec.2005.08.011

Glenn, E.P., Huete, A.R., Nagler, P.L., Hirschboeck, K.K., Brown, P., 2007. Integrating remote sensing and ground methods to estimate evapotranspiration. CRC. Crit. Rev. Plant Sci. https://doi.org/10.1080/07352680701402503

Gonzalez-Dugo, V., Zarco-Tejada, P., Nicolás, E., Nortes, P.A., Alarcón, J.J., Intrigliolo, D.S., Fereres, E., 2013. Using high resolution UAV thermal imagery to assess the variability in the water status of five fruit tree species within a commercial orchard. Precis. Agric. https://doi.org/10.1007/s11119-013-9322-9

Gordon, L.J., Steffen, W., Jonsson, B.F., Folke, C., Falkenmark, M., Johannessen, A., 2005. Human modification of global water vapor flows from the land surface. Proc. Natl. Acad. Sci. https://doi.org/10.1073/pnas.0500208102

Gowda, P.H., Chavez, J.L., Colaizzi, P.D., Evett, S.R., Howell, T.A., Tolk, J.A., 2008. ET mapping for agricultural water management: Present status and challenges. Irrig. Sci. https://doi.org/10.1007/s00271-007-0088-6

Green, R.O., Eastwood, M.L., Sarture, C.M., Chrien, T.G., Aronsson, M., Chippendale, B.J., Faust, J.A., Pavri, B.E., Chovit, C.J., Solis, M., Olah, M.R., Williams, O., 1998. Imaging spectroscopy and the Airborne Visible/Infrared Imaging Spectrometer (AVIRIS). Remote Sens. Environ. https://doi.org/10.1016/S0034-4257(98)00064-9

Griffin, D., Anchukaitis, K.J., 2014. How unusual is the 2012-2014 California drought? Geophys. Res. Lett. https://doi.org/10.1002/2014GL062433

Hanak, E., Lund, J., Dinar, A., Gray, B., Howitt, R., Mount, J., Moyle, P., Thomposn, B., 2011. Managing California's Water: From Conflict to Reconciliation, Water. https://doi.org/DOI: 10.1016/j.jvoice.2007.10.014

Harwood, K.G., Gillon, J.S., Griffiths, H., Broadmeadow, M.S.J., 1998. Diurnal variation of Δ13CO2, Δ18O16O and evaporative site enrichment of δH218O in Piper aduncum under field conditions in Trinidad. Plant, Cell Environ. https://doi.org/10.1046/j.1365-3040.1998.00276.x

Hook, S.J., Myers, J.J., Thome, K.J., Fitzgerald, M., Kahle, A.B., 2001. The MODIS/ASTER airborne simulator (MASTER) - A new instrument for earth science studies. Remote Sens. Environ. https://doi.org/10.1016/S0034-4257(00)00195-4

Horler, D.N.H., Dockray, M., Barber, J., 1983. The red edge of plant leaf reflectance. Int. J. Remote Sens. https://doi.org/10.1080/01431168308948546

Howden, S.M., Soussana, J.F., ..., 2007. Adapting agriculture to climate change. Proc. …. https://doi.org/10.1073/pnas.0701890104

Howitt, R., MacEwan, D., Medellín-Azuara, J., Lund, J., Sumner, D., 2014. Economic Analysis of the 2014 Drought for California Agriculture. Cent. Watershed Sci. Univ. California, Davis, Calif. https://doi.org/10.1016/j.ijrobp.2014.05.013

Hulley, G.C., Hook, S.J., 2011. Generating consistent land surface temperature and emissivity products between ASTER and MODIS data for earth science research. IEEE Trans. Geosci. Remote Sens. https://doi.org/10.1109/TGRS.2010.2063034

Idso, S.B., Jackson, R.D., Pinter, P.J., Reginato, R.J., Hatfield, J.L., 1981. Normalizing the stress-degree-day parameter for environmental variability. Agric. Meteorol. https://doi.org/10.1016/0002-1571(81)90032-7

Idso, S.B., Baker, D.G., Gates, D.M., 1966. The Energy Environment of Plants. Adv. Agron. https://doi.org/10.1016/S0065-2113(08)60650-1

Idso, S.B., Schmugge, T.J., Jackson, R.D., Reginato, R.J., 1978. The Utility of Surface Temperature Measurements for the Remote Sensing of Surface Soil Water Status. J. Geophys. Res. https://doi.org/10.1029/JC080i021p03044

Immitzer, M., Vuolo, F., Atzberger, C., 2016. First experience with Sentinel-2 data for crop and tree species classifications in central Europe. Remote Sens. https://doi.org/10.3390/rs8030166

Irmak, S., Haman, D.Z., Bastug, R., 2000. Determination of crop water stress index for irrigation timing and yield estimation of corn. Agron. J. https://doi.org/10.2134/agronj2000.9261221x

Irrigation Training & Research Center, 2003. California Crop and Soil Evapotranspiration. Irrigation Training & Research Center, California Polytechnic State University, San Luis Obispo, California, USA. ITRC Report No. R 03-001. 65 pp.

Jackson, R.D., Idso, S.B., Reginato, R.J., Pinter, P.J., 1981. Canopy temperature as a crop water stress indicator. Water Resour. Res. https://doi.org/10.1029/WR017i004p01133

Jarvis, P.G., Mcnaughton, K.G., 1986. Stomatal Control of Transpiration: Scaling Up from Leaf to Region. Adv. Ecol. Res. https://doi.org/10.1016/S0065-2504(08)60119-1

Johnson, D.M., 2013. A 2010 map estimate of annually tilled cropland within the conterminous United States. Agric. Syst. https://doi.org/10.1016/j.agsy.2012.08.004

Johnson, R., Cody, B.A., 2015. California Agricultural Production and Irrigated Water Use. Congr. Res. Serv. https://doi.org/10.1115/1.4023255

Jones, H.G., 1999. Use of thermography for quantitative studies of spatial and temporal variation of stomatal conductance over leaf surfaces. Plant, Cell Environ. 22, 1043–1055. https://doi.org/10.1046/j.1365-3040.1999.00468.x

Jones, H.G., Serraj, R., Loveys, B.R., Xiong, L., Wheaton, A., Price, A.H., 2009. Thermal infrared imaging of crop canopies for the remote diagnosis and quantification of plant responses to water stress in the field. https://doi.org/10.1071/FP09123

Kailath, T., 1967. The Divergence and Bhattacharyya Distance Measures in Signal Selection. IEEE Trans. Commun. Technol. https://doi.org/10.1109/TCOM.1967.1089532

Kakani, V.G., Reddy, K.R., Zhao, D., Sailaja, K., 2003. Field crop responses to ultraviolet-B radiation: A review, in: Agricultural and Forest Meteorology. https://doi.org/10.1016/j.agrformet.2003.08.015

Karnieli, A., Agam, N., Pinker, R.T., Anderson, M., Imhoff, M.L., Gutman, G.G., Panov, N., Goldberg, A., 2010. Use of NDVI and land surface temperature for drought assessment: Merits and limitations. J. Clim. https://doi.org/10.1175/2009JCLI2900.1

Kern County Department of Agriculture and Measurement Standards, 2018. Kern County Crop Reports. http://www.kernag.com/caap/crop-reports/crop-reports.asp (accessed 18 October 2018).

Kerr, Y.H., Lagouarde, J.P., Nerry, F., Ottlé, C., 2004. Land surface temperature retrieval techniques and applications Case of the AVHRR, in: Thermal Remote Sensing in Land Surface Processing. https://doi.org/10.18544/PEDM-22.02.0054

Key, T., Warner, T.A., McGraw, J.B., Fajvan, M.A., 2001. A comparison of multispectral and multitemporal information in high spatial resolution imagery for classification of individual tree species in a temperate hardwood forest. Remote Sens. Environ. https://doi.org/10.1016/S0034-4257(00)00159-0

Kings County Department of Agriculture and Measurement Standards, 2018. Kings County Crop Reports. https://www.countyofkings.com/departments/general-services/agriculture-department-measurement-standards/ag-services/crop-reports-1941-2013/test (accessed 18 October 2018).

Kogan, F.N., 1997. Global Drought Watch from Space. Bull. Am. Meteorol. Soc. https://doi.org/10.1175/1520-0477(1997)078<0621:GDWFS>2.0.CO;2

Kongoli, C., Kustas, W.P., Anderson, M.C., Norman, J.M., Alfieri, J.G., Flerchinger, G.N., Marks, D., 2014. Evaluation of a Two-Source Snow–Vegetation Energy Balance Model for Estimating Surface Energy Fluxes in a Rangeland Ecosystem. J. Hydrometeorol. https://doi.org/10.1175/JHM-D-12-0153.1

Kruse, F.A., 2004. Comparison of atrem, acorn, and flaash atmospheric corrections using low-altitude aviris data of boulder, co. 13th JPL Airborne Geosci. Work. Jet Propuls. Lab. https://doi.org/10.1186/s12917-015-0622-3

Lambin, E.F., Ehrlich, D., 1996. The surface temperature-vegetation index space for land cover and land-cover change analysis. Int. J. Remote Sens. https://doi.org/10.1080/01431169608949021

Lee, C.M., Cable, M.L., Hook, S.J., Green, R.O., Ustin, S.L., Mandl, D.J., Middleton, E.M., 2015. An introduction to the NASA Hyperspectral InfraRed Imager (HyspIRI) mission and preparatory activities. Remote Sens. Environ. https://doi.org/10.1016/j.rse.2015.06.012

Lee, D.T., Schachter, B.J., 1980. Two algorithms for constructing a Delaunay triangulation. Int. J. Comput. Inf. Sci. https://doi.org/10.1007/BF00977785

Legates, D.R., Willmott, C.J., 1990. Mean seasonal and spatial variability in gauge-corrected, global precipitation. Int. J. Climatol. 10, 111–127. https://doi.org/10.1002/joc.3370100202

Leinonen, I., Jones, H.G., 2004. Combining thermal and visible imagery for estimating canopy temperature and identifying plant stress. J. Exp. Bot. https://doi.org/10.1093/jxb/erh146

Leuzinger, S., Körner, C., 2007. Tree species diversity affects canopy leaf temperatures in a mature temperate forest. Agric. For. Meteorol. https://doi.org/10.1016/j.agrformet.2007.05.007

Liu, H., Wang, B., Fu, C., 2008. Relationships between surface albedo, soil thermal parameters and soil moisture in the semi-arid area of Tongyu, northeastern China. Adv. Atmos. Sci. https://doi.org/10.1007/s00376-008-0757-2

Lo, M.H., Famiglietti, J.S., 2013. Irrigation in California's Central Valley strengthens the southwestern U.S. water cycle. Geophys. Res. Lett. https://doi.org/10.1002/grl.50108

Lobell, D.B., Asner, G.P., 2002. Moisture Effects on Soil Reflectance. Soil Sci. Soc. Am. J. https://doi.org/10.2136/sssaj2002.7220

Lobell, D.B., Asner, G.P., 2004. Cropland distributions from temporal unmixing of MODIS data. Remote Sens. Environ. https://doi.org/10.1016/j.rse.2004.08.002

Lobell, D.B., Burke, M.B., Tebaldi, C., Mastrandrea, M.D., Falcon, W.P., Naylor, R.L., 2008. Prioritizing climate change adaptation needs for food security in 2030. Science (80-.). https://doi.org/10.1126/science.1152339

Lobell, D.B., Field, C.B., Cahill, K.N., Bonfils, C., 2006. Impacts of future climate change on California perennial crop yields: Model projections with climate and crop uncertainties. Agric. For. Meteorol. https://doi.org/10.1016/j.agrformet.2006.10.006

Lu, J., Sun, G., McNulty, S.G., Amatya, D.M., 2005. A comparison of six potential evapotranspiration methods for regional use in the southeastern United States. J. Am. Water Resour. Assoc. https://doi.org/10.1111/j.1752-1688.2005.tb03759.x

Luo, W., Taylor, M.C., Parker, S.R., 2008. A comparison of spatial interpolation methods to estimate continuous wind speed surfaces using irregularly distributed data from England and Wales. Int. J. Climatol. 28, 947–959. https://doi.org/10.1002/joc.1583

Lynn, B.H., Carlson, T.N., 1990. A stomatal resistance model illustrating plant vs. external control of transpiration. Agric. For. Meteorol. https://doi.org/10.1016/0168-1923(90)90099-R

Mariotto, I., Thenkabail, P.S., Huete, A., Slonecker, E.T., Platonov, A., 2013. Hyperspectral versus multispectral crop-productivity modeling and type discrimination for the HyspIRI mission. Remote Sens. Environ. 139, 291–305. https://doi.org/10.1016/j.rse.2013.08.002

Massey, R., Sankey, T.T., Congalton, R.G., Yadav, K., Thenkabail, P.S., Ozdogan, M., Sánchez Meador, A.J., 2017. MODIS phenology-derived, multi-year distribution of conterminous U.S. crop types. Remote Sens. Environ. https://doi.org/10.1016/j.rse.2017.06.033

McAneney, K.J., Brunet, Y., Itier, B., 1994. Downwind evolution of transpiration by two irrigated crops under conditions of local advection. J. Hydrol. 161, 375–388. https://doi.org/10.1016/0022-1694(94)9013

Medellín-Azuara, J., Harou, J.J., Olivares, M.A., Madani, K., Lund, J.R., Howitt, R.E., Tanaka, S.K., Jenkins, M.W., Zhu, T., 2007. Adaptability and adaptations of California's water supply system to dry climate warming. Clim. Change. https://doi.org/10.1007/s10584-007-9355-z

Medellín-Azuara, J., MacEwan, D., Howitt, R.E., Koruakos, G., Dogrul, E.C., Brush, C.F., Kadir, T.N., Harter, T., Melton, F., Lund, J.R., 2015. Hydro-economic analysis of groundwater pumping for irrigated agriculture in California's Central Valley, USA. Hydrogeol. J. https://doi.org/10.1007/s10040-015-1283-9

Melton, F., Rosevelt, C., Guzman, A., Johnson, L., Zaragoza, I., Verdin, J., Thenkabail, P., Wallace, C., Mueller, R., Willis, P., 2015. Fallowed Area Mapping for Drought Impact Reporting: 2015 Assessment of Conditions in the California Central Valley; NASA Ames Research Center: Mountain View, CA, USA.

Millard et al., J.P., 1978. Crop Water-Stress Assessment Using Airborne Thermal Scanner. Photogramm. Eng. Remote Sensing.

Millard, K., Richardson, M., 2015. On the importance of training data sample selection in Random Forest image classification: A case study in peatland ecosystem mapping. Remote Sens. https://doi.org/10.3390/rs70708489

Moller, M., Alchanatis, V., Cohen, Y., Meron, M., Tsipris, J., Naor, A., Ostrovsky, V., Sprintsin, M., Cohen, S., 2006. Use of thermal and visible imagery for estimating crop water status of irrigated grapevine. J. Exp. Bot. 58, 827–838. https://doi.org/10.1093/jxb/erl115

Moran, M., 2004. Thermal infrared measurement as an indicator of plant ecosystem health, in: Thermal Remote Sensing in Land Surface Processing. https://doi.org/doi:10.1201/9780203502174-c9

Moran, M.S., Clarke, T.R., Inoue, Y., Vidal, A., 1994. Estimating crop water deficit using the relation between surface-air temperature and spectral vegetation index. Remote Sens. Environ. https://doi.org/10.1016/0034-4257(94)90020-5

Moran, M.S., Clarke, T.R., Inoue, Y., Vidal, A., 1994. Estimating crop water deficit using the relation between surface-air temperature and spectral vegetation index. Remote Sens. Environ. https://doi.org/10.1016/0034-4257(94)90020-5

Mote, P.W., Hamlet, A.F., Clark, M.P., Lettenmaier, D.P., 2005. Declining mountain snowpack in western north America. Bull. Am. Meteorol. Soc. https://doi.org/10.1175/BAMS-86-1-39

Mount, J., Hanak, E., 2016. Water Use in California. PPIC Water Policy Cent. https://doi.org/10.5066/F7KD1VXV

Musick, H.B., Pelletier, R.E., 1986. Response of some {Thematic} {Mapper} band ratios to variation in soil water content. Photogramm. Eng. Remote Sensing.

National Agricultural Statistics Service, 2013. California Agricultural Statistics. http://www.nass.usda.gov/Statistics_by_State/California/Publications/California_Ag_Statistics/index.asp

National Academies of Sciences, Engineering, and Medicine, 2018. Thriving on Our Changing Planet: A Decadal Strategy for Earth Observation from Space. National Academies Press. https://doi.org.10.17226/24938.

Nemani, R.R., Running, S.W., 1989. Estimation of Regional Surface Resistance to Evapotranspiration from NDVI and Thermal-IR AVHRR Data. J. Appl. Meteor. https://doi.org/10.1175/1520-0450(1989)028<0276:EORSRT>2.0.CO;2

NOAA National Centers for Environmental information. Climate at a Glance: Statewide Time Series. https://www.ncdc.noaa.gov/cag/ (accessed 23 October 2018)

Nuckols, J.R., Gunier, R.B., Riggs, P., Miller, R., Reynolds, P., Ward, M.H., 2007. Linkage of the California Pesticide Use Reporting Database with spatial land use data for exposure assessment. Environ. Health Perspect. https://doi.org/10.1289/ehp.9518

Ogunjemiyo, S., Roberts, D.A., Keightley, K., Ustin, S.L., Hinckley, T., Lamb, B., 2002. Evaluating the relationship between AVIRIS water vapor and poplar plantation evapotranspiration. J. Geophys. Res. Atmos. https://doi.org/10.1029/2001JD001194

Olioso, A., Carlson, T.N., Brisson, N., 1996. Simulation of diurnal transpiration and photosynthesis of a water stressed soybean crop. Agric. For. Meteorol. https://doi.org/10.1016/0168-1923(95)02297-X

Otkin, J.A., Anderson, M.C., Hain, C., Mladenova, I.E., Basara, J.B., Svoboda, M., 2013. Examining Rapid Onset Drought Development Using the Thermal Infrared–Based Evaporative Stress Index. J. Hydrometeorol. https://doi.org/10.1175/JHM-D-12-0144.1

Ozdogan, M., 2010. The spatial distribution of crop types from MODIS data: Temporal unmixing using Independent Component Analysis. Remote Sens. Environ. https://doi.org/10.1016/j.rse.2010.01.006

Pal, M., 2005. Random forest classifier for remote sensing classification. Int. J. Remote Sens. https://doi.org/10.1080/01431160412331269698

Palazzo, J., Liu, O.R., Stillinger, T., Song, R., Wang, Y., Hiroyasu, E.H.T., Zenteno, J., Anderson, S., Tague, C., 2017. Urban responses to restrictive conservation policy during drought. Water Resour. Res. https://doi.org/10.1002/2016WR020136

Pinter, Jr., P.J., Hatfield, J.L., Schepers, J.S., Barnes, E.M., Moran, M.S., Daughtry, C.S.T., Upchurch, D.R., 2003. Remote Sensing for Crop Management. Photogramm. Eng. Remote Sens. https://doi.org/10.14358/PERS.69.6.647

Platt, R. V, Goetz, A.F.H., 2005. A comparison of AVIRIS and Landsat for land use classification at the urban fringe. Photogramm. Eng. Remote Sensing. https://doi.org/10.14358/PERS.70.7.813

Quattrochi, D. a., Luvall, J.C., 1999. Thermal Infrared Remote Sensing for Analysis of Landscape Ecological Processes: Methods and Applications 577–598.

Rao, N.R., 2008. Development of a crop-specific spectral library and discrimination of various agricultural crop varieties using hyperspectral imagery. Int. J. Remote Sens. https://doi.org/10.1080/01431160701241779

Rijsberman, F.R., 2006. Water scarcity: Fact or fiction?, in: Agricultural Water Management. https://doi.org/10.1016/j.agwat.2005.07.001

Roberts, D.A., 1991. Separating Spectral Mixtures of Vegetation and Soil. University of Washington PhD. Dissertation, 180 pp.

Roberts, D.A., Gardner, M., Church, R., Ustin, S., Scheer, G., Green, R.O., 1998. Mapping chaparral in the Santa Monica Mountains using multiple endmember spectral mixture models. Remote Sens. Environ. https://doi.org/10.1016/S0034-4257(98)00037-6

Roberts, D.A., Green, R.O., Adams, J.B., 1997. Temporal and spatial patterns in vegetation and atmospheric properties from AVIRIS. Remote Sens. Environ. https://doi.org/10.1016/S0034-4257(97)00092-8

Roberts, D.A., Smith, M.O., Adams, J.B., 1993. Green vegetation, nonphotosynthetic vegetation, and soils in AVIRIS data. Remote Sens. Environ. https://doi.org/10.1016/0034-4257(93)90020-X

Roberts, D.A., Dennison, P.E., Roth, K.L., Dudley, K., Hulley, G., 2015. Relationships between dominant plant species, fractional cover and Land Surface Temperature in a

Mediterranean ecosystem. Remote Sens. Environ. 167, 152–167. https://doi.org/10.1016/j.rse.2015.01.026

Roberts, D.A., Quattrochi, D.A., Hulley, G.C., Hook, S.J., Green, R.O., 2012. Synergies between VSWIR and TIR data for the urban environment: An evaluation of the potential for the Hyperspectral Infrared Imager (HyspIRI) Decadal Survey mission. Remote Sens. Environ. https://doi.org/10.1016/j.rse.2011.07.021

Roberts, D.A., Ustin, S.L., Ogunjemiyo, S., Greenberg, J., Bobrowski, S.Z., Chen, J., Hinckley, T.M., 2004. Spectral and structural measures of northwest forest vegetation at leaf to landscape scales. Ecosystems. https://doi.org/10.1007/s10021-004-0144-5

Robeson, S.M., 2015. Revisiting the recent California drought as an extreme value. Geophys. Res. Lett. https://doi.org/10.1002/2015GL064593

Rojas, O., Vrieling, A., Rembold, F., 2011. Assessing drought probability for agricultural areas in Africa with coarse resolution remote sensing imagery. Remote Sens. Environ. https://doi.org/10.1016/j.rse.2010.09.006

Rosegrant, M.W., Ringler, C., Zhu, T., 2010. Water for Agriculture: Maintaining Food Security Under Growing Scarcity, SSRN. https://doi.org/10.1146/annurev.environ.030308.090351

Ross, R.J., Elliot, W.P., 2001. Radiosonde-based Northern Hemisphere tropospheric water vapor trends. J. Clim. https://doi.org/10.1175/1520-0442(2001)014<1602:RBNHTW>2.0.CO;2

Sandholt, I., Rasmussen, K., Andersen, J., 2002. A simple interpretation of the surface temperature/vegetation index space for assessment of surface moisture status. Remote Sens. Environ. 79, 213–224. https://doi.org/10.1016/S0034-4257(01)00274-7

Scherrer, D., Bader, M.K.-F., Körner, C., 2011. Drought-sensitivity ranking of deciduous tree species based on thermal imaging of forest canopies. Agric. For. Meteorol. 151, 1632–1640. https://doi.org/10.1016/J.AGRFORMET.2011.06.019

Schlenker, W., Hanemann, W.M., Fisher, A.C., 2007. Water availability, degree days, and the potential impact of climate change on irrigated agriculture in California. Clim. Change. https://doi.org/10.1007/s10584-005-9008-z

Schmidhuber, J., Tubiello, F.N., 2007. Global food security under climate change. Proc. Natl. Acad. Sci. https://doi.org/10.1073/pnas.0701976104

Sepulcre-Cantó, G., Zarco-Tejada, P.J., Jiménez-Muñoz, J.C., Sobrino, J.A., Miguel, E. De, Villalobos, F.J., 2006. Detection of water stress in an olive orchard with thermal remote sensing imagery. Agric. For. Meteorol. https://doi.org/10.1016/j.agrformet.2006.01.008

Sepulcre-Cantó, G., Zarco-Tejada, P.J., Jiménez-Muñoz, J.C., Sobrino, J.A., Soriano, M.A., Fereres, E., Vega, V., Pastor, M., 2007. Monitoring yield and fruit quality parameters in open-canopy tree crops under water stress. Implications for ASTER. Remote Sens. Environ. 107, 455–470. https://doi.org/10.1016/J.RSE.2006.09.014

Shivers, S., Roberts, D., McFadden, J., Tague, C., 2018. Using Imaging Spectrometry to Study Changes in Crop Area in California's Central Valley during Drought. Remote Sens. https://doi.org/10.3390/rs10101556

Siebert, S., Döll, P., 2007. The Global Map of Irrigation Areas. https://doi.org/10.1086/167779

Somers, B., Cools, K., Delalieux, S., Stuckens, J., Van der Zande, D., Verstraeten, W.W., Coppin, P., 2009. Nonlinear Hyperspectral Mixture Analysis for tree cover estimates in orchards. Remote Sens. Environ. https://doi.org/10.1016/j.rse.2009.02.003

Starrs, P. F., & Goin, P., 2010. *Field Guide to California Agriculture*. University of California Press.

Stewart, I.T., Cayan, D.R., Dettinger, M.D., 2005. Changes toward earlier streamflow timing across western North America. J. Clim. https://doi.org/10.1175/JCLI3321.1

Swain, D.L., Tsiang, M., Haugen, M., Singh, D., Charland, A., Rajaratnam, B., Diffenbaugh, N.S., 2014. 2 . the Extraordinary California Drought of 2013 / 2014 : Character , Context , and the Role of Climate Change 3–7.

Tanaka, S.K., Zhu, T., Lund, J.R., Howitt, R.E., Jenkins, M.W., Pulido, M. a., Tauber, M., Ritzema, R.S., Ferreira, I.C., 2006. Climate warming and water management adaptation for California. Clim. Change 76, 361–387. https://doi.org/10.1007/s10584-006-9079-5

Tanner, C.B., 1963. Plant Temperatures1. Agron. J. 55, 210. https://doi.org/10.2134/agronj1963.00021962005500020043x

Thenkabail, P.S., Enclona, E. a., Ashton, M.S., Van Der Meer, B., 2004. Accuracy assessments of hyperspectral waveband performance for vegetation analysis applications. Remote Sens. Environ. 91, 354–376. https://doi.org/10.1016/j.rse.2004.03.013

Thenkabail, P.S., Mariotto, I., Gumma, M.K., Middleton, E.M., Landis, D.R., Huemmrich, K.F., 2013. Selection of hyperspectral narrowbands (hnbs) and composition of hyperspectral twoband vegetation indices (HVIS) for biophysical characterization and discrimination of crop types using field reflectance and hyperion/EO-1 data. IEEE J. Sel. Top. Appl. Earth Obs. Remote Sens. https://doi.org/10.1109/JSTARS.2013.2252601

Thenkabail, P.S., Smith, R.B., Pauw, E. De, De Pauw, E., 2002. Evaluation of Narrowband and Broadband Vegetation Indices for Determining Optimal Hyperspectral Wavebands for Agricultural Crop Characterization. Photogramm. Eng. Remote Sensing 68, 607–621.

Thompson, D.R., Gao, B.C., Green, R.O., Roberts, D.A., Dennison, P.E., Lundeen, S.R., 2015. Atmospheric correction for global mapping spectroscopy: ATREM advances for the HyspIRI preparatory campaign. Remote Sens. Environ. https://doi.org/10.1016/j.rse.2015.02.010

Tindula, G.N., Orang, M.N., Snyder, R.L., 2013. Survey of Irrigation Methods in California in 2010. J. Irrig. Drain. Eng. https://doi.org/10.1061/(ASCE)IR.1943-4774.0000538

Tortajada, C., Kastner, M.J., Buurman, J., Biswas, A.K., 2017. The California drought: Coping responses and resilience building. Environ. Sci. Policy. https://doi.org/10.1016/j.envsci.2017.09.012

Trenberth, K.E., Fasullo, J., Smith, L., 2005. Trends and variability in column-integrated atmospheric water vapor. Clim. Dyn. https://doi.org/10.1007/s00382-005-0017-4

Tucker, C.J., Garratt, M.W., 1977. Leaf optical system modeled as a stochastic process. Appl. Opt. https://doi.org/10.1364/AO.16.000635

Tulare County Agricultural Commissioner/Sealer, 2018. Crop Reports. http://agcomm.co.tulare.ca.us/ag/index.cfm/standards-and-quarantine/crop-reports1/crop-reports-2011-2020/ (accessed 18 October 2018).

United States Drought Monitor. https://droughtmonitor.unl.edu/ (accessed on 8 June 2018).

United States Geological Survey, 2018. 2012-2016 California Drought: Historical Perspective. https://ca.water.usgs.gov/california-drought/california-drought-comparisons.html (accessed 18 October 2018).

University of California Division of Agriculture and Natural Resources, 2018. Crop Irrigation Strategies. http://ucmanagedrought.ucdavis.edu/Agriculture/Crop_Irrigation_Strategies/ (accessed 25 October 2018).

USDA National Agricultural Statistics Service Cropland Data Layer, 2018. Published crop-specific data layer. https://nassgeodata.gmu.edu/CropScape/ (accessed October 22, 2018). USDA-NASS, Washington, DC.

U.S. Department of the Interior, 2014. Reclamation Managing Water in the West: Sacramento and San Joaquin Basins Climate Impact Assessment. https://www.usbr.gov/watersmart/baseline/docs/ssjbia/ssjbia.pdf (accessed 30 January 2019)

US Geological Survey. 2012–2016 California Drought: Historical Perspective. Available online: https://ca.water.usgs.gov/california-drought/california-drought-comparisons.html (accessed 8 June 2018).

Vermeulen, S.J.; Aggarwal, P.K.; Ainslie, A.; Angelone, C.; Campbell, B.M.; Challinor, A.J.; Hansen, J.; Ingram, J.S.; Jarvis, A.; Kristjanson, P.; et al. *Agriculture, Food Security and Climate Change: Outlook for Knowledge, Tools and Action. Climate Change, Agriculture and Food Security Report 3*; CGIAR-ESSP Program on Climate Change, Agriculture and Food Security (CCAFS): Copenhagen, Denmark, 2010.

Vuolo, F., Neuwirth, M., Immitzer, M., Atzberger, C., Ng, W.-T., 2018. How much does multi-temporal Sentinel-2 data improve crop type classification? Int. J. Appl. Earth Obs. Geoinf. https://doi.org/10.1016/j.jag.2018.06.007

Waldhoff, G., Lussem, U., Bareth, G., 2017. Multi-Data Approach for remote sensing-based regional crop rotation mapping: A case study for the Rur catchment, Germany. Int. J. Appl. Earth Obs. Geoinf. https://doi.org/10.1016/j.jag.2017.04.009

Wardlow, B., Egbert, S., Kastens, J., 2007. Analysis of time-series MODIS 250 m vegetation index data for crop classification in the U.S. Central Great Plains. Remote Sens. Environ. 108, 290–310. https://doi.org/10.1016/j.rse.2006.11.021

Wardlow, B.D., Egbert, S.L., 2008. Large-area crop mapping using time-series MODIS 250 m NDVI data: An assessment for the U.S. Central Great Plains. Remote Sens. Environ. 112, 1096–1116. https://doi.org/10.1016/j.rse.2007.07.019

Wetherley, E.B., Roberts, D.A., McFadden, J.P., 2017. Mapping spectrally similar urban materials at sub-pixel scales. Remote Sens. Environ. https://doi.org/10.1016/j.rse.2017.04.013

Wu, Z., Thenkabail, P.S., Mueller, R., Zakzeski, A., Melton, F., Johnson, L., Rosevelt, C., Dwyer, J., Jones, J., Verdin, J.P., 2014. Seasonal cultivated and fallow cropland mapping using MODIS-based automated cropland classification algorithm. J. Appl. Remote Sens. 8, 083685. https://doi.org/10.1117/1.JRS.8.083685

Xiao, J., Moody, A., 2005. A comparison of methods for estimating fractional green vegetation cover within a desert-to-upland transition zone in central New Mexico, USA. Remote Sens. Environ. https://doi.org/10.1016/j.rse.2005.07.011

Yan, L., Roy, D.P., 2016. Conterminous United States crop field size quantification from multi-temporal Landsat data. Remote Sens. Environ. https://doi.org/10.1016/j.rse.2015.10.034

Yang, Y., Anderson, M.C., Gao, F., Wardlow, B., Hain, C.R., Otkin, J.A., Alfieri, J., Yang, Y., Sun, L., Dulaney, W., 2018. Field-scale mapping of evaporative stress indicators of

crop yield: An application over Mead, NE, USA. Remote Sens. Environ. https://doi.org/10.1016/j.rse.2018.02.020

Yepez, E.A., Williams, D.G., Scott, R.L., Lin, G., 2003. Partitioning overstory and understory evapotranspiration in a semiarid savanna woodland from the isotopic composition of water vapor. Agric. For. Meteorol. https://doi.org/10.1016/S0168-1923(03)00116-3

Zarco-Tejada, P.J., Ustin, S.L., Whiting, M.L., 2005. Temporal and spatial relationships between within-field yield variability in cotton and high-spatial hyperspectral remote sensing imagery. Agron. J. https://doi.org/10.2134/agronj2003.0257

Zarco-Tejada, P.J., González-Dugo, V., Berni, J.A.J., 2012. Fluorescence, temperature and narrow-band indices acquired from a UAV platform for water stress detection using a micro-hyperspectral imager and a thermal camera. Remote Sens. Environ. 117, 322–337. https://doi.org/10.1016/J.RSE.2011.10.007

Zermeño-Gonzalez, A., Hipps, L.E., 1997. Downwind evolution of surface fluxes over a vegetated surface during local advection of heat and saturation deficit. J. Hydrol. 192, 189–210. https://doi.org/10.1016/S0022-1694(96)03108-3

Zhang, X., Friedl, M.A., Schaaf, C.B., Strahler, A.H., Hodges, J.C.F., Gao, F., Reed, B.C., Huete, A., 2003. Monitoring vegetation phenology using MODIS. Remote Sens. Environ. https://doi.org/10.1016/S0034-4257(02)00135-9